On the effects of external noise on diffusion and pattern formation in biofluid systems

Von der Universität Bayreuth

zur Erlangung des Grades eines

Doktors der Naturwissenschaften (Dr. rer. nat.)

genehmigte Abhandlung

von

Mithun Thampi

aus Sulthan Bathery, Kerala, Indien

1. Gutachter: Prof. Dr. Matthias Weiss

2. Gutachter: Prof. Dr. Markus Retsch

Tag der Einreichung: 15.12.2022

Tag des Kolloquiums: 26.05.2023

Abstract

Self-organization into well-defined higher-order structures by energy consumption is a crucial feature of biological systems. Exploring these features in vitro using simple biofluid system like *Xenopus* extracts have recently attracted much interest. This thesis deals with developing methods to understand self-organization under enhanced mixing, confinement, and chemical perturbations. For enhanced mixing inside microdroplets, magnetic stir bars (MSBs) were synthesized and characterized along with a custom-made inverted microscope-compatible stirrer and its controllers. Stirring aqueous droplets with MSBs enhanced the seemingly normal diffusion of tracer particles with its signature encoded in the velocity autocorrelation function. The applicability of MSBs in extract droplets is demonstrated by quantifying fluctuations of ensembles of microtubules.

As a next step, the self-organization of *Xenopus* interphase extract with similar spatial arrangements of cell-like compartments was achieved without any template structures (centrosome or chromatin). Quantifying these features over time showed similar geometrical features with increasing length scale due to the merging of the nearby protocells. These features remained invariant in the presence of a microtubule-stabilizing drug, taxol, with a reduced size, which reduces with increasing taxol concentration. Furthermore, the arrangement of the patterns achieved in microfluidic chambers depends on the chamber geometry. Moreover, in cycling extract supplemented with sperm heads, the cell-like division was achieved. As a preliminary result, the initial pattern in microfluidic chamber depends on the microfluidic chamber, but the smaller daughter protocells that formed later evenly distributed the whole chamber independent of the geometry. The interphase and cycling extract results resembled the patterns in energids and embryos of developing organisms. The results presented in this thesis provide new insights into the complex self-organization processes in cells and the methods that can be utilized to deepen the understanding.

Zusammenfassung

Ein essenzielles Merkmal biologischer Systeme ist die Selbstorganisation hin zu geordneten Strukturen weit jenseits des thermischen Gleichgewichts. Phänomene dieser Art lassen sich in vitro besonders gut mit Zellextrakten, gewonnen aus Eiern des Krallenfroschs *Xenopus laevis*, beobachten. In dieser Arbeit wird die Entwicklung von Methoden beschrieben, um Selbstorganisation in Anwesenheit von verstärktem Durchmischen, lokaler Beengtheit oder chemischen Störungen zu verstehen. Um Mikro-Tröpfchen verstärkt zu durchmischen, wurden sowohl magnetische Rührstäbchen (MSBs) synthetisiert und charakterisiert als auch der zugehörige maßgefertigte Rührer mit Ansteuerung angefertigt, welcher kompatibel mit invertierten Mikroskopen ist. Das Rühren wässriger Tröpfchen mit MSBs führt zu einer Verstärkung der normal erscheinenden Diffusion von Testpartikeln, was in den Charakteristika der Geschwindigkeitsautokorrelationsfunktion zu erkennen ist. Die Anwendbarkeit der MSBs wurde anhand von Fluktuationen eines Mikrotubuliensembles in Extrakttröpfchen gezeigt.

Im nächsten Schritt wurde die Selbstorganisation von *Xenopus* Interphase-Extrakt zu zellartigen Kompartimenten in Abwesenheit von vorgebenden Strukturen (Zentrosomen oder Chromatin) untersucht. Das Charakterisieren dieser Eigenschaften über die Zeit offenbart zeitlich invariante geometrische Merkmale, wobei die charakteristische Längenskala durch das Verschmelzen von benachbarten Protozellen wächst. Diese Eigenschaften blieben in der Anwesenheit des Mikrotubuli stabilisierenden Wirkstoffs Taxol erhalten, wobei die Strukturen mit steigender Taxolkonzentration schrumpfen. Darüber hinaus hängt das entstehende Muster, welches in einer Mikrofluidikkammer realisiert wird, von der Geometrie dieser Kammer ab. Weiterhin wurde zellartige Teilungen in sog. Cycling Extrakten realisiert, welche mit Spermienköpfen versehenen wurden. Vorläufige Ergebnisse zeigen, dass das anfängliche Muster von der Mikrofluidikkammer abhängt, während sich die kleineren Tochterzellen, welche sich später bilden, unabhängig von der Geometrie gleichmäßig in der Kammer verteilen. Die Muster, die in Interphase und Cycling Extrakt ausgebildet werden, ähneln dabei denen von Embryos des Nematoden *Caenorhabditis elegans*. Die Ergebnisse dieser Arbeit geben neue Einblicke in komplexe Prozesse der Selbstorganisation von Zellen und in Methoden, welche verwendet werden können, um deren Verständnis zu vertiefen.

Contents

1 Introduction

Self-organization and self-assembly are two fundamentally different mechanisms that generate macromolecular structures. Self-organization is the emergence of the overall order of a system in time and space resulting from the collective interaction of its components without any external intervention. It requires a constant supply of energy to maintain its order and usually occurrs in non-equilibrium or dissipative systems [1]. In contrast, self-assembly is widely discussed as the physical association of molecules into an equilibrium structure [1, 2]. This concept of self-organization is widely regarded as the basic principle of pattern formation in physical, chemical and biological systems [1]. Examples of biological patterns include the school of fish, a raiding column of army ants, the synchronous flashing of fireflies, the facetted eye of *Drosophila*, lichen growth, and pigmentation patterns on shells, fish and mammals [3]. In particular, the self-organization of macromolecular complexes and organelles in biological systems has attracted much interest in scientific research (see ref. [2, 4]).

Several theories can be found in the literature to elucidate the principles of pattern formation (see ref. [5]). However, few of them are as universal as the theory of reaction-diffusion systems proposed by Alan Turing in his seminal article on *The chemical basis of morphogenesis* [6]. Turing found that the interplay of molecular diffusion and chemical interaction causes instability in the spatially uniform state, resulting in patterns [7]. Using the simple model with two interacting diffusive molecules (morphogen), Turing mathematically revealed six potential steady states, depending on the dynamics of reaction terms and the wavelength of the pattern [8]. These structures are known as reaction-diffusion, Turing, or dissipative structures. Prigogine and coworkers widely used the term dissipative structures as the dissipation of chemical energy are required to drive this system and keep it in a far-from-equilibrium state. This dissipation of energy serves as the thermodynamic driving force for self-organization [9]. The morphogen concept was validated in studies with *Drosophila* syncitial embryo and *Pombe* cells [10]. These ideas and theories paved a new way for conceptualizing the biological system's pattern formation mechanisms.

The emergence of systems like *Xenopus* extract, with the technological advances in microscopy and enhanced mathematical modeling abilities, enabled us to study complex self-organization phe-

nomena in living systems in greater depth. The concept of self-organization is well studied in actin and microtubule cytoskeleton [2]. A beautiful demonstration of microtubule self-organization in vitro using tubulin, microtubule motors, GTP and ATP can be seen in Nédélec et al. [11]. More complex self-organized structures like mitotic spindle formation in cell-like droplets [12, 13], cell-like pattern formation and division [14] were recently established using *Xenopus* egg extracts. The confinement and chemicals also influenced the pattern formation observed in these systems. Since biological systems are complex fluids consisting of several macromolecules and organelles, these can affect the diffusion of the molecules [15, 16]. This dense condition is called macromolecular crowding and it can influence the pattern formation.

This thesis focuses on developing experimental methods to explore the effects of enhanced mixing, confinement and chemical perturbation on self-organization in a biofluid system. The biofluid system used in this work is egg extract, obtained from *Xenopus laevis*, an important model organism in biology. Protocols for extract preparation, microfluidic device fabrication and microdroplet-compatible magnetic stir bars (MSBs) synthesis were developed for the study. In addition, a magnetic stirring system compatible with an inverted confocal microscope was also created, allowing confocal imaging while stirring.

The MSBs were used to achieve enhanced mixing, and the mixing effect was quantified using tracer bead trajectories (using the single particle tracking method) in an aqueous droplet. The effect of MSBs agitation on self-organization in the extract was also probed. The cell-like pattern formation in the presence and absence of a microtubule-stabilizing drug, taxol, was quantified over time using the parameter obtained from Voronoi tesselation. In addition, the effect of geometrical confinement on pattern formation was probed using microfluidic chambers having different geometries. Moreover, the cell-like division was probed in microfluidic chambers.

The **fundamental part**, chapter 2 gives an overview of the research using the model organism *Xenopus laevis* and discusses *Xenopus* oocyte maturation and extract preparation. Moreover, it gives an overview of microtubule and mitotic spindles. Furthermore, the basics of Brownian motion, anomalous diffusion, and the velocity autocorrelation function are covered.

Chapter 3 discusses the common **materials and methods** used in this thesis. A brief overview of extract preparation protocols (extended protocol is given in the Appendix A.1) and microfluidic fabrication methods is provided, along with a detailed discussion of the T-junction device and the microfluidic chamber used in the thesis. Furthermore, the data analysis methods, single particle tracking (SPT) and Voronoi tesselation are explained in detail.

Chapter 4 focused on the **magnetic stirring in microdroplets** using the MSBs and the inverted microscope-compatible stirring devices. The synthesis and characterization methods used for MSBs, and the development of different stirring devices are presented in detail. The stirring effect of MSBs is demonstrated using an aqueous droplet with tracer particles and MSBs. The SPT analysis of tracer particles is utilized to obtain the stirring signature and diffusion characteristics.

Furthermore, MSBs stirring signature obtained in the *Xenopus* extract droplet is also presented in detail.

The effect of chemical perturbation and confinement in **structure and pattern formation** in *Xenopus* extract is discussed in Chapter 5. The protocol to obtain mitotic spindle in cell-like water in oil droplets, cell-like compartmentalization in interphase extract, and cell-like division using cycling extract are discussed in detail. In addition, the effect of taxol addition on pattern formation and quantification of its effect over time using the parameter obtained from Voronoi tesselation is presented. Furthermore, the effect of chamber geometry on pattern formation and division is probed using microfluidic chambers with different geometries and presented its possible implication with embryos of developing organisms.

This thesis concludes with a summary of the work's findings and a note on the potential applications of the methods developed. Moreover, additional information and figures related to the thesis are provided in the Appendix A.

2 Fundamentals

This chapter will provide an overview of the research using the model organism Xenopus and discusses Xenopus oocyte maturation and extract preparation. Moreover, it gives an overview of microtubule and mitotic spindle research. The last section discusses Brownian motion, diffusion, anomalous diffusion, and velocity autocorrelation function.

2.1. *Xenopus laevis*

Xenopus is a genus of aquatic frogs native to Africa, commonly known as African clawed frogs. Two species of these frogs, *Xenopus laevis* and *Xenopus tropicalis* are widely used model organisms in research [17, 18]. The *Xenopus tropicalis* is diploid, while *Xenopus laevis* is allotetraploid, which is its only disadvantage, making them less suitable for studying mutant phenotypes [19]. However, *Xenopus laevis* offers an experimental advantage over other vertebrates because of the abundance of large (>1 mm) and robust eggs and embryos accessible at all stages of development [19–21]. Adding to that *Xenopus* colonies are comparatively easy to maintain in the laboratory and can be induced to lay eggs in a controlled manner by injecting human chronic gonadotropin (HCG) [22, 23]. Since HCG hormone is present in the urine of pregnant women, it was used for pregnancy testing in the last century [24] and aided its distribution to laboratories worldwide [25]. The major cellular and developmental processes are conserved in mammals and *Xenopus*. Furthermore, the high degree of genomic synteny made them valuable in studying human development and diseases [19, 20]. Some early work with *Xenopus* led to the 2012 Nobel prize of Sir John B. Gurdon in Physiology or Medicine [26]. He demonstrated that inserting a tadpole nucleus into a frog egg results in fertilization and healthy offspring [27], which paved the way for the cloning of Dolly, the sheep [28].

Figure 2.1.: *Xenopus laevis* with its laid eggs

The experimental studies with *Xenopus* eggs and embryos are fascinating due to the following three factors: (i) embryos can withstand extensive surgical manipulations [29, 30]. (ii) External materials such as nucleus [27], mRNA [31–33], proteins [34], and so on can be easily injected into eggs and embryos. Targeted injections to individual blastomere at a specific embryonic stage are also possible [35, 36]. (iii) Eggs and embryos are a rich source of material for biochemical studies [19, 37–39]. The cell-free extracts prepared by crushing the eggs and embryos helped study cell cycle events in vitro with increased possibilities in biochemical manipulations [40–43]. It overcomes the limitations of microinjection's ability to perturb the cell cycle as well as the difficulties of microscopic analysis of intercellular activities in intact embryos [23].

Xenopus cytoplasmic extracts were extensively used to study: cell cycle oscillations [44, 45], mitotic spindle assembly [13, 46], chromosome segregation [47, 48], cell cycle regulation of microtubule and actomyosin cytoskeleton [42, 49, 50], and many other processes [51]. An interesting feature of this system is its ability to manipulate the cell cycle state. In this thesis, I have prepared *Xenopus* extracts arrested in interphase or meiosis II states. Also, prepared extract can constitute multiple cell cycles. The knowledge of oocyte development is crucial for these extract preparation, which is discussed in the next section.

2.1.1. *Xenopus* oocyte maturation and extract preparation

Eukaryotic cell cycle

An idea about cell cycle phases is beneficial to understand the developmental stages of *Xenopus* oocytes and the extract preparation methods. The eukaryote cell cycle consists of four discrete phases: gap phase 1 (G_1), gap phase 2 (G_2), synthesis phase (S), and mitotic phase (M). The G_1, G_2, and S together make up the interphase. The cell accumulates chromosomal DNA, associated proteins, and energy reserves for the next task during the G_1 phase. In the S phase, the cell replicates its DNA and centrosome. During the G_2 phase, it synthesizes proteins required for chromosome manipulation, duplicates some organelles, and replenishes its energy storage. It also dismantles the cytoskeleton to provide resources for the M phase.

The M phase is a multistep process in which the duplicated chromosome becomes aligned, separated, moved to the poles, and divided into two daughter cells. The stages in the M phase are prophase, prometaphase, metaphase, anaphase, telophase, and cytokinesis. In prophase, the nucleolus disappears, chromatin condenses into chromosomes, centromeres move to the poles, and mitotic spindle formation starts. Prometaphase advances the spindle formation, microtubules connecting the centromere to the kinetochore in the chromosome. The chromosome becomes aligned in the equatorial plane (metaphase plate) during the metaphase. In anaphase, sister chromatids separate at the centromere and move to opposite poles. In telophase, the chromosome reaches the opposite poles and begins to decondense. A nuclear envelope forms around the chromosome, and the nucleosomes appear in the nuclear area. Also, the spindle depolymerizes into tubulin for cytoskeleton formation in daughter cells. Cytokinesis finishes cell division by physically separating

the cytoplasmic components into two daughter cells. Meiosis is similar to mitosis but undergoes two back-to-back cell divisions without a DNA duplication in between, yielding four daughter cells with half the parent's chromosome [52, 53].

Xenopus oocyte maturation

A sexually mature female *Xenopus laevis* contains tens of thousands of oocytes in the ovary. The oocytes begin as a cell, a little larger than the somatic cells, which undergo DNA replication and enter into the prophase of the meiosis cell cycle. The oocytes stay in this G_2-like growth phase for several months. Once fully grown, it remains in an arrested G_2-like state (Dumont stage VI) and it can stay in this state for a long time [54, 55].

The steroid hormone progesterone overcomes this arrest and causes oocyte maturation, which produces a fertilizable oocyte arrested in meiosis II. The progesterone is synthesized and released by follicle cells in response to the pituitary luteinizing hormone (LH). Injection of human chronic gonadotropin into the frog's dorsal lymph sac can also induce oocyte maturation by activating the same receptor as LH, which is used extensively in research to induce egg production [56]. The universal inducer of cell division, maturation promoting factor (MPF; complex between cyclin-dependent kinase 1 (Cdk1) and Cyclin B), controls the oocyte maturation. MPF was kept inactive in prophase, and the progesterone secretion made them active, resulting in meiosis resumption. Oocytes completes the meiosis I and comes to metaphase II. The cytostatic factor (CSF) present in the cytoplasm inhibits anaphase promoting complex/cyclosome (APC/C), which results in the second arrest at metaphase. The eggs (mature oocytes) laid by *Xenopus laevis* are in the CSF-arrested state. The CSF arrest was released upon fertilization or parthenogenic activation by releasing the Ca^{2+} ions. The activated/fertilized egg proceeds through anaphase and advances into the next cell cycle [54, 55, 57, 58].

Extract preparation

The cell-free cytoplasmic extracts prepared from *Xenopus laevis* are extensively used to study intracellular events in vitro [44–46, 50]. The extracts are prepared by crushing eggs or embryos using centrifugation. They mainly include interphase, CSF, cycling and embryo extract. As you might expect, the name is determined by the final state of the extract and preparation protocol. The key differences are outlined below.

a) Interphase extract: Crushing of the eggs result in the Ca^{2+} release from its intracellular stores, which mimics the fertilization wave and activates the entry into first mitotic interphase. Cycloheximide added to the extract prevents further protein synthesis, resulting in the interphase arrest [59, 60].

b) CSF extract: This extract is prepared in the presence of a calcium chelator (such as EGTA) maintains its metaphase arrest. Interphase extract can be prepared from CSF extract by adding Ca^{2+}. It can be returned to the mitotic phase by adding fresh CSF [59].

c) Cycling extract: This extract is prepared from activated eggs (by calcium ionophore or electrical shock) in the absence of EGTA. Egg activation causes Ca^{2+} release from intercellular stores and results in the exit from the CSF arrest state. Since protein synthesis is not inhibited, this extract can do multiple cell cycles [61].

d) Embryo extract: This extract is prepared from the embryos of *Xenopus laevis* utilizing the synchronous division of fertilized eggs. Exogenously added cell cycle machinery regulators (non-degradable cyclin B and an APC/C inhibitor) arrest the prepared extract in metaphase. The yield of embryo extract is low compared to egg extracts [60].

In this thesis, I have prepared different types of extracts (CSF, interphase and cycling; see section 3.1 and A.1) to study the mitotic spindle formation (using CSF extract; see section 5.1), cell-like compartment formation (using interphase extract; see section 5.2) and cell-like division (using cycling extracts; see section 5.3).

2.2. Microtubules and mitotic spindle

Microtubules

Microtubules (MTs) are one of the significant components of the cytoskeleton of eukaryotic cells, which perform a variety of essential functions, such as chromosome segregation, formation of cilia and flagella, cell polarity, positioning of organelles, and transport of cargo in cells [52, 62]. MTs are rigid hollow tubes made up of $\alpha\beta$-tubulin heterodimers that associate head to tale to form linear protofilaments (PFs), which in turn associate laterally to form the hollow cylindrical structure [63–66]. MTs typically comprise 13 PFs [67] with a diameter of 25 nm [63], although MTs with a different number of PFs have also been reported [68].

MTs nucleation can happen in a self-organized manner or from a templated structure. Spontaneous MTs nucleation needs to overcome a large energy barrier, hence a kinetically restraint process. Spontaneous nucleation of MTs can occur in the presence of GTP and Mg^{2+} ions but requires a much higher tubulin concentration than is necessary for the growth of existing MTs [69, 70]. There are some molecules known to promote spontaneous microtubule nucleation. Such molecules are microtubule-stabilizing drugs (e.g., taxol) and glycerol [70–73]. Another member of the tubulin superfamily, γ-tubulin, also supports the nucleation of MTs by forming the γ-tubulin ring complex (γ-TURC). The γ-TURC usually contains 10-13 γ-tubulin and can establish a strong longitudinal connection with the α-tubulin (minus end) of the tubulin dimer, thus forming a template for MT [70, 74]. MTs are also nucleated from pre-existing MTs, and the augmin complex mediates it by targetting the γ-TURC to a pre-existing MT, where a new MT is nucleated at an angle [70, 75–77].

MTs are very dynamic and stochastically alternate between the phase of growth and shrinkage. This out-of-equilibrium feature is termed as dynamic instability [78] and is essential for its func-

tion [79]. It is the consequence of binding and GTP hydrolysis at β-tubulin [80]. Both tubulin dimers bind to GTP, where α-tubulin one is non-exchangeable (N-site) and serves only a structural function [81]. In contrast, GTP at β-tubulin (E-site) is exchangeable and responsible for polymerization and dynamic instability [66]. The E-site GTP undergoes hydrolysis to GDP upon adding an unpolymerized tubulin dimer at the end [82]. As a result, growing MT consists primarily of GDP-bound tubulin dimers, with a relatively small region at the tip (β-tubulin end, also known as plus end) containing newly incorporated GTP-tubulin (GTP-cap) [83]. The GTP-cap is necessary for MT stabilization and growth [84]. Hydrolysis of this GTP-cap results in a structural strain and allosterically affects lateral contacts between PFs [37]. So GTP-hydrolysis at plus end leads to the depolymerization of the MTs (also referred as catastrophe). MTs disassemble fully or until the GTP-cap stochastically re-establish, which leads to repolymerization (rescue) [83]. Numerous factors control the dynamic instability of MTs and the connection of MTs to cellular structure, and these factors are broadly grouped into microtubule-associated proteins (MAPs) and molecular motors [37].

Mitotic spindle

The spindle is the MTs-based macromolecular machine that accurately segregates replicated chromosomes into two daughter cells during mitosis. The spindle formed during meiosis is called the meiosis spindle and is similar to the mitosis spindle [46, 52]. The following discussion mainly focuses on the mitotic spindle. The initial discovery of the mitotic spindle happened around the late 19th century, and the history of mitosis research discussed in the review of McIntosh et al. [85].

The spindle formation starts at the onset of mitosis. At prophase, the interphase MTs disassemble and begin forming the spindle MTs. The minus end of the MTs localized on the poles, and the positive end interacts with chromosomes. The spindle acquires its typical fusiform structure at the metaphase by arranging chromosomes at the spindle equator. Chromosomes segregate to opposite poles during anaphase, and cell division ends in telophase with the formation of daughter cells [38, 52]. The spindle primarily comprises an antiparallel arrangement of microtubules, with the minus end pointing toward the spindle poles and the plus end pointing toward the chromosome. The centrosome organizes the mitotic spindle pole in most cell types and nucleates the MTs. Kinetochore, a protein complex assembled on the centromere, connects the chromosome to the MTs. There are three distinct sub-populations of MTs in mitotic spindles: (i) kinetochore MTs, which connect the chromosome to the spindle poles, (ii) interpolar MTs extend from the poles and interact antiparallel to stabilize the bipolarity of the spindle, and (iii) astral MTs, that radiate out from the centrosome into the cytoplasm and helps in positioning the spindle in the cell [52, 88]. Several proteins are also involved in mitotic spindle formation and its proper functioning [38, 88, 89].

Xenopus laevis egg extracts played a significant role in studying the mitotic spindle [12, 55, 90–97]. This section discusses how the egg extract system constitutes spindle assembly. There are different pathways to create spindle assembly using CSF extracts. The DNA inside the egg

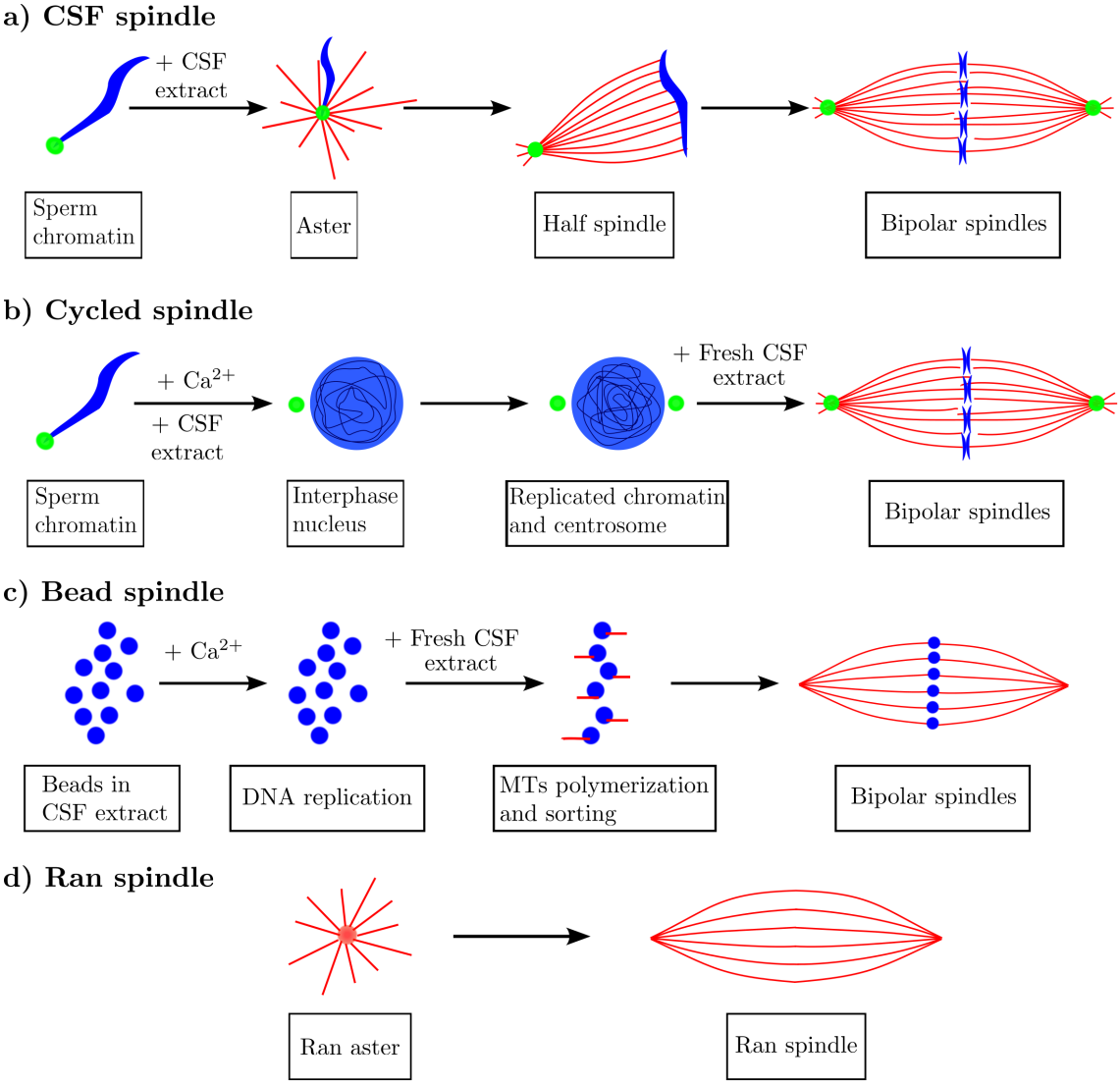

Figure 2.2.: Schematic representation of different spindle assembly reactions: **(a)** CSF spindle: Sperm heads added to the CSF extract, forms asters, which develop into half spindles and finally bipolar spindles. **(b)** Cycled spindle: The CSF extract containing sperm heads cycled into interphase using Ca^{2+}. Chromatin and centrosome replication happens at interphase. Fresh CSF addition results in mitotic entry and spindle formation. **(c)** Bead spindle: Plasmid DNA coated beads incubated in the CSF extract cycled through interphase, results in spindle formation. **(d)** Ran spindle: Addition of RanGTP to CSF extract causes the formation of asters and spindle. Schematic is adapted from [86, 87].

pelleted during the crushing spin to create the extract, but an external DNA addition triggered spindle formation [87]. The four main methods discussed in the literature to create a spindle are given below [86, 87, 90, 98].

a) CSF spindle (Figure 2.2a): The demembranized sperm heads added to the CSF extract serves as a nucleation sites for MTs and forms asters. These asters develop into half-spindles and eventually form the bipolar spindle. Because the extract is in meiosis II, the resulting spindle is correctly referred to as a meiotic spindle.

b) Cycled spindle (Figure 2.2b): For the cycled spindle, Ca^{2+} is added along with the demembranated sperm head. The Ca^{2+} abolishes the CSF arrest and initiates the entry of the extract into the interphase. In this interphase state, centrosome duplication and DNA replication take place. Then the extract can be cycled back to mitosis by adding an equal volume of fresh CSF extract. It results in the formation of the bipolar mitotic spindle from the centrosomes, analogous to the spindle formation in normal cells.

c) Bead spindle (Figure 2.2c): Magnetic beads coated with plasmid DNA incubated in CSF extract and cycled into interphase using Ca^{2+}. The extract was cycled back to mitosis using fresh CSF extract. The active chromatin assemblies on these DNA beads support MT polymerization and form the mitotic spindle with the help of motor proteins. Here, there are no kinetochores or centrosomes to support spindle assembly.

d) Ran spindle (Figure 2.2d): Incubating non-hydrolyzable RanGTP in CSF extract causes MT polymerization and the formation of small spindle-like structures (Ran spindle) and asters (Ran aster).

In this thesis, I have used the cycled spindle reaction method to create the spindle (see Chapter 5).

2.3. Brownian motion and diffusion

In order to consider motion or forces acting at the subcellular level, it was beneficial to consider Brownian motion. The random motion of particles suspended in a medium was named after botanist Robert Brown, who first observed this phenomenon looking at the movement of pollen grains in water in 1827 [99]. From the Newtonian perspective, it was surprising to see this active movement in the absence of forces. In 1905, Albert Einstein came up with a seminal paper (molecular kinetic theory of heat) demonstrating that the thermal excitation of water molecules in the surrounding media is responsible for the irregular motion of pollen grains [100, 101]. Around the same time, the Brownian motion was independently explained by Marian Smoluchowski [102]. These predictions were later experimentally confirmed by Jean Perrin in 1908, for which he received the Nobel prize in 1926 [103, 104].

In 1908, French physicist Paul Langevin came up with another concept to demonstrate the Brownian motion [105]. The Langevin equation is Newton's second law for Brownian particles, and historically it is the first example of a stochastic differential equation [106]. It also considered the inertia of Brownian particles, which Einstein and Smoluchowski neglected. For simplicity, the Langevin equation in 1D for a Brownian particle of mass m and an external potential U can be written as follows

$$m\frac{\mathrm{d}^2x}{\mathrm{d}t^2} = F_{ext}(x) - \gamma\frac{\mathrm{d}x}{\mathrm{d}t} + F'(x,t), \text{ with } F_{ext}(x) = -\nabla U \tag{2.1}$$

where γ is the friction coefficient (proportional to viscosity, η) and $F'(x,t)$ is the delta-correlated Gaussian white noise.

Here we also have to consider the relative importance of viscous to inertial force in the above equation, which can be represented using the Reynolds number (Re). For a spherical object with radius a, density ρ moving with a velocity ν in a fluid, Re becomes,

$$Re = \frac{F_{inertial}}{F_{viscous}} = \frac{\rho a^2 \nu^2}{\eta a \nu} = \frac{\rho a \nu}{\eta} \tag{2.2}$$

The subcellular realm belongs to low Re. For example, a typical bacterium with few μm size and velocity of 30 $\mu\mathrm{m/s}$ has Re of 10^{-4} and for molecular motors with a length scale of 10 nm and velocity of order, 1 $\mu\mathrm{m/s}$ has even smaller $Re \approx 10^{-8}$ [107]. We can neglect the inertia term in this overdamped regime with low Re since $|m\frac{\mathrm{d}^2x}{\mathrm{d}t^2}| \ll |\gamma\frac{\mathrm{d}x}{\mathrm{d}t}|$. Here we no longer consider the medium as continuous fluid and the particulate nature comes into play. The impacts of the medium on the immersed object are captured in the $F'(x,t)$ and the Equation 2.1 becomes

$$F_{ext}(x) - \gamma\frac{\mathrm{d}x}{\mathrm{d}t} + F'(x,t) = 0 \tag{2.3}$$

The corresponding Fokker-Planck equation governing the evolution of the probability $p(x,t)$ (probability of finding the particle at a position x at time t) is similar to the Fick second law of diffusion [108] with an additional drift term. Integrating Equation 2.3 over all possible realizations of $F'(x,t)$ while assuming the external potential U= 0, the equation becomes

$$\frac{\partial}{\partial t}p(x,t) = D\frac{\partial^2}{\partial x^2}p(x,t) \tag{2.4}$$

Here, D is the diffusion coefficient, a proportional constant, and denotes the diffusing substances' rapidity. The solution of the Equation 2.4 assuming that the particle's initial position is at x = 0 and at time t = 0 is a Gaussian function.

$$p(x,t) = \frac{1}{\sqrt{4\pi Dt}}\exp\left(-\frac{x^2}{4Dt}\right) \tag{2.5}$$

The distribution function (Equation 2.5), the diffusion propagator, depends on time t and position x. Its moments characterize the diffusion of the particle ensemble. Here only the even moments are non-zero and the second moment, mean square displacement (MSD), can determine all subsequent moments and measure particle motion. For this purpose, MSD was calculated in our experiments using the tracked time-resolved particle positions.

Ensemble-averaged MSD $\langle MSD(\tau)\rangle_E$ refers to M realizations of a single particle trajectory (or a single trajectory of M particles), while time-averaged MSD $\langle MSD(\tau)\rangle_t$ is calculated by monitoring N positions in a single particle trajectory over time, keeping the time difference (τ) between successive positions constant. Owing to ergodicity (i.e., mean values of various observ-

ables in the system do not depend on the averaging method) [109], the $\langle MSD(\tau)\rangle_E$ will be equal to $\langle MSD(\tau)\rangle_t$

$$\langle MSD(\tau)\rangle_E = \langle (x_i(\tau) - x_i(0))^2\rangle_E = \frac{1}{M}\sum_{i=1}^{M}(x_i(\tau) - x_i(0))^2 \tag{2.6}$$

$$\langle MSD(\tau)\rangle_t = \langle (x(t_i+\tau) - x(t_i))^2\rangle_t = \frac{1}{N}\sum_{i=1}^{N}(x(t_i+\tau) - x(t_i))^2 \tag{2.7}$$

By solving the Equation 2.3 in the absence of F_{ext} and using the equipartition theorem [110] results in

$$\langle MSD(\tau)\rangle_t = \frac{2k_BT\tau}{\gamma} \tag{2.8}$$

where k_B is the Boltzmann constant and T is the absolute temperature.

According to the fluctuation-dissipation theorem [111], the Einstein-Smoluchowski relation gives a relationship between MSD and the diffusion coefficient D. For a d-dimensional system, it is as follows

$$\langle MSD(\tau)\rangle_t = 2dD\tau \tag{2.9}$$

where $D = \frac{k_BT}{\gamma}$, which relates the noise at microscopic level to the dissipation at macroscopic level. At low Re, the D can be expressed in terms of the particle and the embedding fluid using the Stokes-Einstein equation [100, 112]. For a spherical particle of radius R, D becomes

$$D = \frac{k_BT}{6\pi\eta R} \tag{2.10}$$

2.3.1. Anomalous diffusion

The normal diffusion discussed in the previous sections obeys the Gaussian central limit theorem (CLT) and is ergodic. However, later studies show that many of the natural processes are, in fact, anomalous, and it violates at least one of the three conditions assumed by Einstein to derive the diffusion equation (see ref. [113, 114] for details) and breaks the strong convergence to Gaussian. In the case of anomalous diffusion, the MSD no longer scales linearly with time, but shows a non-linear scaling according to a power law.

$$\langle MSD(\tau)\rangle_t = 2dK_\alpha\tau^\alpha,\ \alpha \neq 1 \text{ is a positive number} \tag{2.11}$$

with the anomalous diffusion exponent α and generalized diffusion coefficient K_α of physical di-

mension $cm^2(s^\alpha)^{-1}$. When α = 1, the Equation 2.11 transformed into normal diffusion equation (Equation 2.9).

Based on the α, the anomalous diffusion is typically divided into three regimes; subdiffusion ($0 < \alpha < 1$), superdiffusion ($\alpha > 1$) and ballistic transport (α = 2) [115, 116]. Subdiffusive behavior is commonly observed in biological contexts as a result of macromolecules or organelles in the cytoplasm (a phenomenon known as macromolecular crowding) [117–119]. Out of the many mathematical models presented in the literature, the fractional Brownian motion (FBM) and continuous time random walk (CTRW) are frequently used to model this anomalous processes (see [113] for details).

One of the reasons for the anomalous behaviour is due to long-range correlation in the particle trajectory, where particles have a memory of the previous moments. This process is described mathematically using the FBM. The Hurst coefficient (H) is often used instead of α in the FBM literature, but is related to it as $\alpha = 2H$ [113, 116]. In FBM, a persistent superdiffusive movement can occur if the correlation is positive [120], while a negative correlation leads to an antipersistent subdiffusive behaviour [121–123]. Subdiffusive behaviour usually occurs in cells when the viscoelastic behaviour of cell cytoplasm (due to macromolecular crowding and the presence of elastic elements, such as cytoskeletal filaments and nucleus) act on the diffusing particles. The antipersistent trajectory created by repeated cycles of compression and restoration, causing the particle to move subdiffusively.

The CTRW problem exhibits anomalous behavior via two independent probability distributions, one for the step sizes and another one for the time increments between two steps. These two probability distributions are not correlated in time or to each other. A broad distribution in time with a narrow distribution in step sizes leads to subdiffusion [113]. This model is used to study diffusion in several systems [124–126]. When the particles occasionally take large steps leads to a broad distribution of step sizes, which gives rise to superdiffusive Levy flights [113]. Levy flights were observed in the foraging of animals for food [127, 128], fluorescent molecules within an assembly of giant cetyl bromide micelles in salt water [129], movement of T cells to fight the pathogen [130], etc. The CTRW model exhibits a weak ergodicity breaking, while the FBM is ergodic [113].

Along with other types of anomalous diffusion, the ballistic transport of motor proteins were also observed in cells [131]. In this thesis, we used the single particle tracking method to obtain the particle trajectory and investigated the effects of stirring on the diffusion of tracer particles.

2.3.2. Velocity autocorrelation function

The velocity autocorrelation function (VACF) is a readily available quantity from experimental data that can be used to distinguish between different diffusion models [132]. The VACF is defined as

$$C_v(\tau) = \frac{\langle v(t)v(t+\tau)\rangle}{\langle v(t)^2\rangle}, \quad \text{with } v(t) = \frac{1}{\delta t}[r(t+\delta t) - r(t)] \tag{2.12}$$

Here $v(t)$ is the instantaneous velocity at time t, determined using the distance $(r(t+\delta t) - r(t))$ traveled within a period δt, which is an integer multiple of the frame time (δt = $n\Delta t$) used for particle tracking and τ = $k\Delta t$ is the lag time.

The VACF of free Brownian motion/unbounded CTRW process is uncorrelated while FBM is correlated. For a free Brownian motion the VACF drops to zero as $C_v \sim 1-(\tau/\delta t)^\alpha$ and becomes zero for $\tau \geq \delta t$, where α is the anomalous diffusion exponent. For a confined CTRW process shows a cross over to negative values and it decays back to zero (from negative side) at long τ. This antipersistant behaviour is due to reflections at the boundary or the effect of the confining potential [113, 132].

For FBM, an alternative expression for the VACF can be obtained by rescaling τ with δt, which gives an expression with dimensionless time ξ = $\tau/\delta t$ = k/n [123].

$$C_{v,FBM}(\xi) = \{(\xi+1)^\alpha + |\xi-1|^\alpha - 2\xi^\alpha\}/2 \tag{2.13}$$

The self-similarity of FBM processes can be seen by keeping the ξ fixed while varying k and n. Self-similarity can be broken due to localization errors during single particle tracking experiments, and the VACF is sensitive to it. According to the Equation 2.13, at ξ =1, the α has a direct correlation with VACF value, $C_{v,FBM}(\xi = 1)$ = $2^{\alpha-1} - 1$ [123, 133]. For subdiffusive FBM, the VACF is similar to confined CTRW and becomes indistinguishable from each other [113]. For superdiffusive FBM, persistent correlation can be seen beyond ξ=1 with an asymptotic decay to zero [133].

3

Materials & Methods

This chapter contains the common materials and methods used in this thesis. The upcoming chapters will discuss the materials and methods explicitly used in the respective section. The first section describes the different Xenopus laevis extracts prepared as part of this research. The following section deals with the methods used to fabricate microfluidic chips and modify their surface properties. This section also covers the fabrication of T-junction devices for microdroplet production and microfluidic chambers for interphase and cycling extracts. The final section addresses the data analysis methods, single particle tracking and Voronoi tesselation.

3.1. *Xenopus laevis* extract preparation

We utilized the lab facilities of Prof. Olaf Stemmann (Genetics, University of Bayreuth) to prepare *Xenopus laevis* extract. Prof. Stemmann's Ph.D. students (Ms. Brigitte Neumann and Mr. Alexander Cuba Ramos) chose the frog from their *Xenopus* colony and performed hormone injections to induce egg laying. After the human chorionic gonadotropin (HCG) injection, we kept the injected frog in separate 4 L containers containing 1.5 L of egg laying buffer/1x Marc's Modified Ringer's (MMR) buffer for egg laying. We usually have enough eggs for the extract preparation about 16 h after the injection. In our experiments, we didn't pool eggs from different frogs, as we saw it can degrade the quality of the extract and helped us to achieve at least one good extract.

When we started the extract preparation, two injections were given to induce egg laying, pregnant mare serum gonadotropin (PMSG) three days before and HCG one day before the extract preparation. However, later we found out a single HCG injection was enough to induce egg laying (in interphase and cycling extract preparations, only given a single HCG injection). We also noticed that stressed frogs lay bad quality eggs and become extra careful while handeling them. The extract quality mainly depends on the quality of the eggs. If more than a quarter of the eggs are bad, we didn't use that batch for extract preparation. If we have only a few bad ones, we carefully removed the bad ones and used the rest for extract preparation. We also had to strictly follow the timings of each protocol steps to yield a high-quality extract. Below is a brief description of the procedures

we used to create cytostatic factor arrested (CSF) extract, interphase extract, and cycling extract. However, the appendix section A.1 comprehensively discusses the materials and buffers used for extract preparation, its experiments, and extract preparation protocols.

3.1.1. CSF extract

The CSF extract preparation protocol was adapted from the protocols of Murray et al. [23, 134], Hannak et al. [87], and Good et al. [12, 60, 135].

CSF cytoplasmic extracts were prepared from freshly laid *Xenopus laevis* eggs. Briefly, eggs in the metaphase stage of meiosis II were collected and dejellied. These eggs were washed with cytostatic factor extract buffer (CSF-XB), and finally packed by centrifugation with the excess buffer that is removed. These packed eggs were crushed and fractionated into three distinctive layers by centrifugation using a Beckman Coulter JS-13.1 swinging bucket rotor. Then the mid cytoplasmic layer was carefully isolated and supplemented with 10 μg/mL of protease inhibitors (leupeptin, pepstatin, and chymostatin), 10 μg/mL of cytochalasin D, 1:50 of ATP regeneration mix, and stored on ice. We used this extract within 6 h of preparation for the experiments that required fresh extract. 20 μL extract aliquots were deep-frozen in liquid nitrogen and stored at -80°C for the experiments which did not require fresh extract.

The addition of protease inhibitors limits protein degradation [136], while cytochalasin D addition avoids actin polymerization [137].

3.1.2. Interphase extract

The interphase extract preparation protocol was adapted from Refs. (Deming and Kornbluth, 2006) [138] and (Sparks and Walter, 2018) [139] with the following minor modifications: A single HCG injection 16-17 h before the experiment was sufficient to obtain proper egg harvest. We changed the concentration of MMR to 0.5x (instead of 0.25x) and washed five times instead of three times. Correcting for a typo, we used KCl instead of HCl in the egg lysis buffer (ELB) preparation. Cycloheximide was added to the extract only after egg crushing (not in the ELB) but cytochalasin B was added already to the ELB in the centrifuge tube to which eggs were transfered for crushing (50 μg/mL final concentration).

Interphase-arrested cytoplasmic extracts were prepared from freshly laid oocytes of *Xenopus laevis* following standard protocols [138, 139]. In brief, eggs in the metaphase stage of meiosis II were collected and dejellied. These eggs were washed first with 0.5x MMR, then with ELB containing Dithiothreitol (DTT), and finally packed by centrifugation with the excess buffer being removed. Packed eggs were crushed and fractionated into three distinctive layers by centrifugation using a Beckman Coulter JS-13.1 swinging bucket rotor and open-top polyclear centrifuge tubes (Seton, 4/6.5 mL). Then the mid cytoplasmic layer was carefully isolated and supplemented with 5

μg/mL of aprotinin, 5 μg/mL of leupeptin, 5 μg/mL of cytochalasin B, 50 μg/mL of cycloheximide, and stored on ice; these extracts were used within 6 h.

The addition of cycloheximide inhibits protein synthesis, including the synthesis of new cyclin. Thus, the extract is arrested in an interphase state. The addition of protease inhibitors (aprotinin, leupeptin) limits protein degradation (Chan and Forbes, 2006) [136], while cytochalasin B suppresses actin polymerization [137].

3.1.3. Cycling extract

The cycling extract preparation protocol was adapted from the protocol of Chang et al. [140], with the following modification. We didn't do the washing step with XB^{+} buffer.

Cycling cytoplasmic extracts were prepared from freshly laid *Xenopus laevis* eggs. Briefly, eggs in the metaphase stage of meiosis II were collected and dejellied. The eggs were first washed in the 0.2x MMR and then activated in the calcium ionophore solution for exactly 2 min. At this point you can see a change in the colour of the eggs and be careful with the activation time as a longer exposure will result in a poor extract. Then wash it immediately with 1 L of XB buffer and transfer it to a Seton open-top centrifuge tube containing 500 μL XB^{++} buffer. Pack these eggs by centrifugation and remove the excess buffer. Finally, crush these packed eggs and fractioned into three distinctive layers by centrifugation with a Beckman Coulter JS-13.1 swinging bucket rotor. The mid cytoplasmic layer was then carefully isolated and supplemented with 10 μg/mL of protease inhibitor (leupeptin, pepstatin, and chymostatin), and 10 μg/mL of cytochalasin B. It was centrifuged again with a tabletop centrifuge and the top lipid layer was carefully removed with a 2 mL syringe with a 30-gauge needle. The clear extract is isolated using a pipette with the pipette tip cut off, avoiding the dark pigmented part at the bottom. The clear extract is stored on ice and used within 6 h.

Depending on the purpose, the extract can be supplemented with ATP regeneration/energy mix (30 μL in 970 μL extract). In our case, we decided not to have a regeneration mix because we only want to see cycling in the extract. Chang et al. [140] found that sometimes energy mix prevent the extract from cycling, so it is not used unless they are attempting to do a very long ($>$ 8 cycles) experiment. The addition of protease inhibitors (chymostatin, leupeptin, pepstatin) limits protein degradation [136], while cytochalasin B suppresses actin polymerization [137].

3.2. Microfluidics

We fabricated the microfluidic devices using the conventional photolithographic techniques in the clean room facility of Prof. Markus Retsch (Physical Chemistry 1, University of Bayreuth). We used MicroWriter (MicroWriter ML3 Baby Plus from Durham Magneto Optics Ltd.) to create the master molds for our poly(dimethylsiloxane) (PDMS)-based microfluidic devices. The fabrication

of a microfluidic device comprises several stages, including design, master mold preparation, curing of the PDMS over the master mold, punching the channel inlets and outlets, gluing the PDMS to a glass slide to fabricate the device, surface treatment of the channels, etc. Below is a detailed explanation of these procedures.

3.2.1. Fabrication of master mold

We created the desired design of the microfluidic channels using AutoCAD software in a *.dxf* file format. The KLayout software converted the file into the MicroWriter readable *.cif* file format.

Master molds was created in silicon wafers (Si-Mat Silicon Materials) with a diameter of 76.2 mm (3 inches) and a thickness of 381 $\pm$ 25 μm. We cleaned the wafers in isopropanol and dried them with compressed air to remove debris from the surface. The wafer is then centered on the spin coater (Brewer Science model 200x) and coated with the SU-8 2050 negative photoresist. Tuning the time and rotation speed, as mentioned in the datasheet of the photoresist [141], can adjust the thickness of the coating. The photoresist-coated wafer was soft-baked using two preheated hot plates (Harry Gestigkeit DT 6015 Digsi-Therm Safety Precision Hotplate). The hotplates were preheated at 65°C and 95°C, and we went sequentially from low to high temperature to reduce the stress on the photoresist. The exposure time is adjusted based on the technical data sheet [141].

The soft-baked wafer is moved to the MicroWriter and digitally centered using three edge points so that the pattern on the wafer is exposed correctly. The software then calculated the wafer height with the photoresist. After setting the necessary parameters, the exposure started with the experimentally determined exposure dose (3500 mJ/cm^2). Exposure time depends on the size and detail of the design, as well as the quality of the exposure required. It typically took from 4 h to 12 h. This wafer subsequently undergoes post-exposure bake in succession at 65°C and 95°C on the preheated hotplates according to the data sheet [141]. The wafer was developed using mr-Dev 600 developer, which removes the unexposed photoresist. If there is no unexposed photoresist left, it was cleaned with isopropanol and dried with compressed air. The developed wafer (master mold) was kept in a pre-cleaned Petri dish until used to minimize impurities.

3.2.2. PDMS microfluidic device

We transferred the microfluidic patterns to PDMS by curing PDMS over the master mold. Varying the ratio of the PDMS base to the curing agent can alter the elastic properties of the PDMS [142]. The PDMS base to the curing agent (Sylgard®184 silicone elastomer kit, Dow Corning) ratio used in our study was 10:1 w/w. We weighed and mixed the PDMS and its curing agent in a weighing boat. The mixture was subsequently poured onto the master mold placed in the Petri dish and degassed with a desiccator (Duran® desiccator, DWK Life Sciences GmbH) connected to a vacuum pump (Laboport® N 86 KT.18, KNF Neuberger GmbH). If bubbles remained under the master mold, they were carefully removed with a pipette tip. It was then cured in a preheated oven (Heraeus

INSTRUMENTS UT 6200, Thermo Scientific) at 75°C for 3 h. The cured PDMS was carefully cut and removed from the master mold with a scalpel and used for microfluidic device fabrication.

The required weight of PDMS and curing agent depends on the desired thickness of the cured PDMS. As a rule, we used 20 g of PDMS and 2 g of hardener for the first casting and then changed the weight taking into account the PDMS remaining in the master mold after we had removed the patterned parts required to fabricate the microfluidic chip.

The microfluidic chips were fabricated by bonding these patterned PDMS substrates to a microscope slide. First, we carefully punched holes (inlets and outlets) into the microfluidic channels of the cured PDMS using a 1.2 mm puncher (Harris Uni-Core). The puncher cleaned before each punching procedure to avoid debris accumulating in the holes. A Scotch® Magic™ tape was used to remove the remaining PDMS fragments and dust. We also employed a stereo microscope (Leica S8 APO) to detect the PDMS substrate's debris and channel/hole defects. The microscope slides were precleaned using isopropanol by sonication (Elmasonic S 15 (H), Elma Schmidbauer GmbH) for 15 min. We used air plasma to bond the PDMS and microscope slide together. The bonding surfaces were activated with a plasma cleaner (PDC-32G-2, Harrick Plasma) for 20 s at 122 Pa (916 mTorr) with HIGH intensity plasma and bonded immediately. Without damaging the channels, the air trapped between them was carefully removed with a pipette tip. The device was then placed in a 75°C oven for 45 min to complete the bonding.

3.2.3. Surface treatments

The PDMS chips have several advantages: low curing temperature, optical permeability, non-toxicity, biological compatibility, non-flammable and gas permeable [143]. PDMS is hydrophobic by nature, but after plasma bonding it becomes hydrophilic due to the formation of -OH groups at the surface, with the effect decaying to baseline in around 24 h. This change in surface hydrophobicity can greatly affect the performance of many PDMS chips, and for our experiments it is important that the channels are hydrophobic. To enhance the hydrophobic nature we used one of the following two methods: Treatment with (i) a commercially available Aquapel water-repellent kit or (ii) with trichloro-(1H, 1H, 2H, 2H-perfluorooctyl)silane. In the discussion that follows, I will use the term chip to refer the PDMS chip.

For Aquapel treatment, the Aquapel vial was carefully opened, and the channels were filled with a 2 μL pipette. Then the Aquapel is removed from the channel with a stream of nitrogen gas and cleaned with a Kimwipe. The chip was then kept in the oven at 75°C for more than 4 h to evaporate the excess Aquapel. The chip remains hydrophobic for a long time after this treatment. Similarly, we could also make the glass surfaces hydrophobic.

In the second method, the channels of the fresh chips were filled with 1% trichloro-(1H, 1H, 2H, 2H-perfluorooctyl)silane in HFE 7500 fluorinated oil. The filled chips were then heated at 75°C for 20 min on a hot plate to evaporate the excess liquid and accelerate the reaction [144]. It

is important to perform this step under a fume hood as toxic fumes are produced. Afterwards, all channels are hydrophobic and ready for use.

We also observed flow in our channels due to fluid permeation, even though the water was the least likely to swell the PDMS [145]. However, soaked chips overnight in Milli-Q water resulted in a significant reduction in the flow [146].

3.2.4. Flow control system

There are several technologies for controlling microfluidic flow in the chip. The most common are pressure pumps and syringe pumps. Pressure pumps create flow by pressurizing the fluid reservoir and pushing the fluid from the reservoir into the microfluidic system. Because they are pressure-driven and have no mechanical component, pressure changes can propagate throughout the system without delay, providing stable flow. Modern systems have microfluidic pressure sensors that improve the system's flow control accuracy. Syringe pumps are mechanical system that advances a syringe to create flow. The main advantage is controlling flow through microchannels independent of fluid resistance. But it can cause pulsating flow at low flow rates.

We used syringe pumps for our experiments and this flow control system was ordered and installed together with Dr. Pierre-Yves Gires (Post-Doc). The syringe pump used was the neMESYS low pressure module V2 with BASE 120 neMESYS controller from CETONI. We used the CETONI Qmix Elements software to control the syringe pumps. With this software, we can create and run custom program scripts and manage the syringe in real time.

We used PTFE Teflon tubing to connect the syringes to the chips (inner diameter 0.5 mm and outer diameter 1.58 mm). In addition, the tubes were connected to the chip after the liquid reached the end of the tubes to prevent air bubbles from being trapped. An inverted microscope (Zeiss Axiovert 25 microscope with Manta G-201 camera containing Sony ICX274 Sensor from Allied Vision Technologies GmbH) was used to monitor the successful filling of the chip with fluid and the formation of droplets.

3.2.5. Droplet generation using microfluidic chip

The microfluidic chip was produced using the method discussed in this section. We have used T-junction devices to create homogenous water in oil droplets. T-junction devices have been used extensively in the literature to produce droplets [12, 147, 148], and the mechanisms of droplet formation have also been studied in depth [149–153]. In a T-junction device, the continuous phase (or carrier fluid) flow meets a dispersed phase flow entering perpendicularly at the junction, resulting in the formation of droplets when the two phases are immiscible. Several other factors play a role in droplet formation, such as flow rate, channel geometry, surface properties, etc.

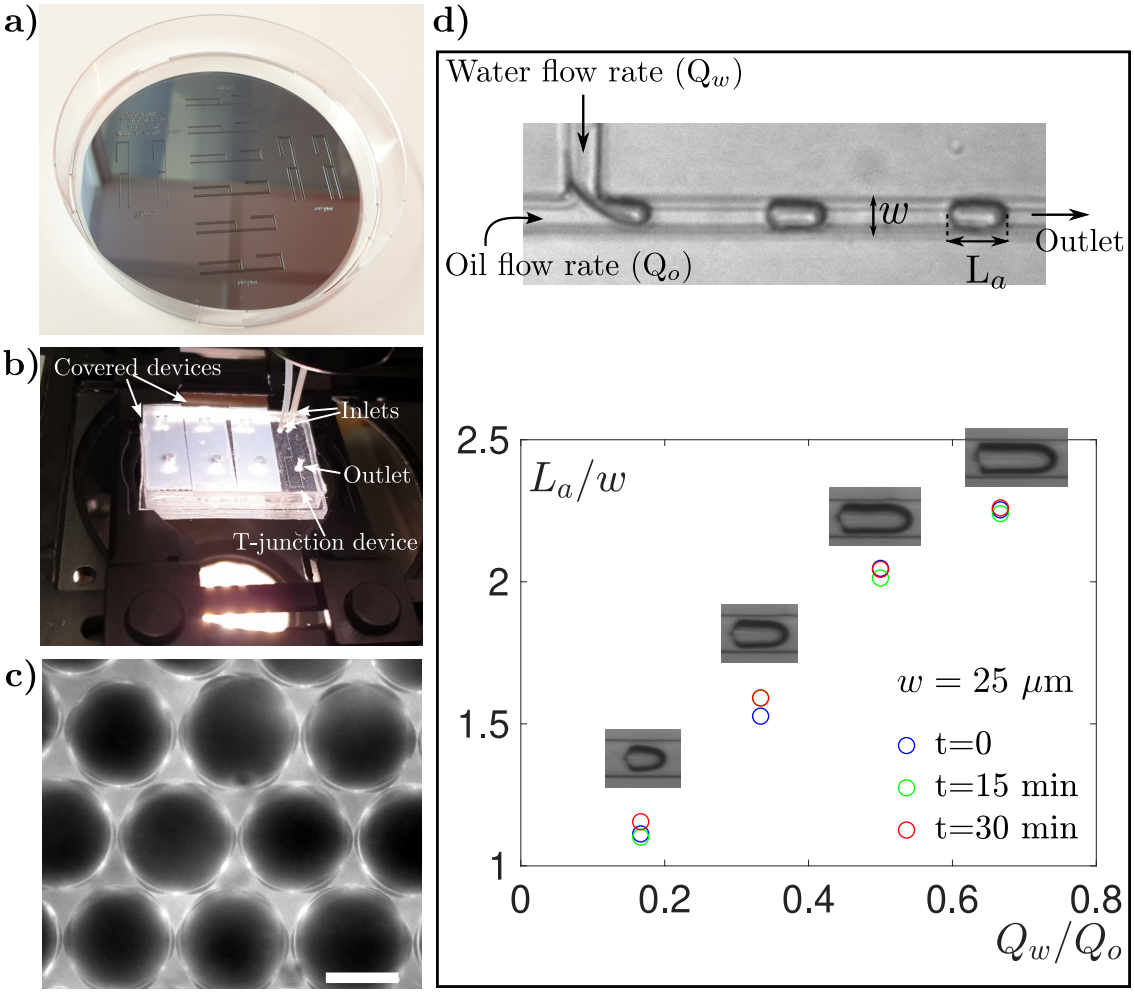

Figure 3.1.: Microfluidic droplet generation: **(a)** Master mold with the design of the T-junction device in a Petri dish. The design was produced with the MicroWriter. **(b)** PDMS chip with four T-junction devices on top of a microscope. Droplet is produced in one of the devices, while the rest is covered with Magic tape to avoid contamination and dust. The PTFE tubings are connected to the inlet and the outlet containing the produced droplets. **(c)** Homogeneous droplets produced with the T-junction devices observed under the microscope. The scale bar is 100 μm. **(d)** Dependence of flow rate on droplet size: The oil flow rate (Q_o) was fixed, and varied the water flow rate (Q_w). The ratio of droplet length (L_a) to width (w) was used as a measure of droplet size and plotted against the ratio of flow rates (water to oil). An increase in the water flow rates resulted in a large L_a/w, indicating bigger droplets (see the corresponding droplet image). The droplet images taken at three time points (0, 15, and 30 min) of the droplet generation had similar sizes, indicating the stability of the flow. A T-junction device with a width of 25 μm was used for this experiment.

T-junction device

The T-junction devices used for droplet production have a thickness of 50 μm. The width of the channels was changed depending on the experimental requirement. The commonly used width was 25 μm, and for some CSF experiments, we also used 50 and 100 μm. The channel (based on the carrier channel) has a total length of 26 mm, with the last 5 mm widened at a one-degree angle outwards. The dispersed phase channel was made parallel to the carrier channel from its inlet for 10 mm, then it joined the carrier channel at 90 degrees, making the T-junction. The droplets were formed at the T-junction, and they traveled around 16 mm to reach the outlet (see Figure 3.1b). In

the initial phase of the study, we had an issue with droplet merging. The long and wide outlet in the chip was to avoid the coalescence of droplets. The T-junction chips used in the study were treated with Aquapel, as discussed in the section 3.2.3.

Droplet production

We have used the CETONI syringe pump for the droplet generation (see section 3.2.4). First, the syringes were filled with the carrier and dispersed phase fluids. The continuous phase in our experiments was Squalene oil with Cithrol DPHS surfactant, and the dispersed phase was water (or the fluid to be encapsulated). We prepared Cithrol DPHS containing Squalene oil by mixing 1 mL Squalene oil with 50 mg Cithrol DPHS in 2 mL Eppendorf tube. The mixture was vortexed for 20 s and kept overnight in a thermomixer at 45°C and 1400 rpm to dissolve it completely.

To fill the syringes, we first connected the PTFE tubings to the syringes and then carefully placed them in the syringe pump and calibrated their position using the Qmix Elements software. The syringes were then filled using the software at a rate of 500 μL/h. While making droplets using CSF extract, we filled both syringes with Squalene oil containing Cithrol DPHS to limit extract usage, and it also helped in fast droplet production before the extract became bad. Just before the droplet production, we removed a small amount of Squalene oil from the dispersed phase syringe and filled it with 50 μL of extract. Since we need a long PTFE tubing to connect the syringe to the inlet of the T-junction device, the extract won't even reach inside the syringe. Before connecting the PTFE tubing to the inlet of the chip, we made sure that the carrier/dispersed phase reached the end of the PTFE tubes. This was to avoid bubbles being trapped inside the chip. Then we controlled the flow rates using the Qmix Elements software and generated the droplets, and it was monitored using the Zeiss Axiovert 25 microscope.

Flow rate dependence on droplet size

Flow rate dependence on droplets size was tested using a 25 μm wide T-junction device with Squalene oil (hereafter referred to as oil) as the carrier phase and water as the dispersed phase. The oil flow rate (Q_o) was fixed at 6 μL/h, and the water flow rate (Q_w) was changed from 2 to 10 μL/h. Increasing Q_w increased the droplets' length (L_a), indicating that the droplet size increased as the width (w) was fixed by the device geometry (see Figure 3.1d). We kept the device running at the specified flow rates for at least 30 min and took droplet images at regular intervals. Analysis of the images showed that the droplet size did not change over time, and it was indicative of the stability of our droplet production. The droplet size measured at the beginning (0 min), 15, and 30 min were shown along with its size ratio (L_a/w) in Figure 3.1d. The brightfield image of the produced droplets had homogeneous sizes indicating the stable production of droplets. The brightfield image of the produced droplets (see Figure 3.1c) had homogeneous sizes indicating the stable production of droplets.

3.2.6. Fabrication of PDMS microfluidic chambers for interphase and cycling extracts experiments

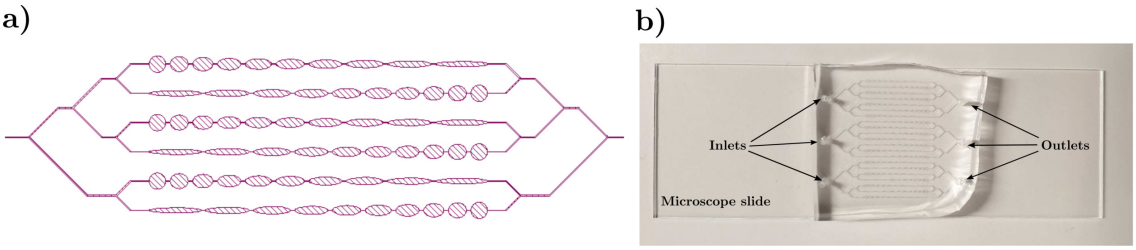

Figure 3.2.: PDMS microfluidic chamber design and chip: **(a)** The design used to produce the master mold with the MicroWriter contains six subchannels with different chamber geometries in an alternating sequence. **(b)** The fabricated PDMS microfluidic chip with three similar chamber systems with separate inlets and outlets.

The microfluidic chip used for the interphase and cycling experiments was similar and fabricated using the methods discussed earlier. The chip consisted of several chambers with varying geometries linked together by a small narrow channel. In addition, each chip contains three similar chamber channel systems (CCS), each with its own inlet and outlet. Furthermore, each chamber channel system has six subchannel systems with chambers of varying geometries. The chamber geometry was based on a circle, and by varying the aspect ratio, various geometries emerged, ranging from circles to elongated ellipses linked by a small channel. The chamber arrangement in the subchannel system was reversed in alternating subchannels (see Figure 3.2a). We fabricated chips with three different chamber sizes (based on circle diameter): 900 μm, 700 μm, and 500 μm, which we refer to as large, medium, and small chips in the following discussions. In all cases, the connecting channel was 20 μm wide, and the chips had a height of 220 μm (see Figure 3.2b for a representative microfluidic chip). The channels were rendered hydrophobic using the trichloro-(1H, 1H, 2H, 2H-perfluorooctyl)silane immediately after the bonding and soaked in water to avoid flow during imaging with the extract, as discussed in section 3.2.3.

3.3. Data Analysis

In this thesis, we used FIJI [154] or MATLAB to perform image analysis and MATLAB to analyze the corresponding data. The two main data analysis methods used in this thesis are single particle tracking (SPT) and Voronoi tesselation. We used the FIJI plugin TrackMate for SPT to study the effect of stirring in the biomimetic fluid. The self-organization of the *Xenopus* extract into cell-like compartments (protocells) was investigated with Voronoi tesselation using the Voronoi function of MATLAB. A brief description of these two methods is provided below.

3.3.1. Single particle tracking

SPT is one of the techniques capable of visualizing dynamic processes by understanding the motion of single particles and molecules in various environments with ultimate sensitivity and spatiotemporal resolution (for more details see reviews [155, 156]). The first application of SPT in biology was in the mid-1980s, and it was initially known as nanovid microscopy [157, 158]. Over the years, the simplicity of SPT, along with the advancements in microscopic techniques, molecular labelling strategies, trajectory reconstruction algorithms, data analysis capabilities, etc., led to various extraordinary understandings in biology and also evolved as a tool to study the complexity of living systems from a physics perspective [155, 159]. SPT was extremely useful in studying anomalous diffusion in living cells in depth (for example, see review [15]).

In SPT experiment, the motion of fluorescently tagged molecules inside the cells or fluorescent particles (quantum dots, polystyrene beads, etc.) was imaged by optical microscopy and analyzed using image processing methods. The reporter's (in our case, fluorescence beads) image collected at the detector appears as a diffraction pattern with the shape of concentric rings with decreasing intensity outwards from the center. The central ring (called the Airy disc) contains the most intensity. A 2D Gaussian (Equation 3.1) can approximate its profile with I_0 as the intensity of the central ring, and σ is the standard deviation of the intensity profile (also known as the point spread function (PSF) of the microscope).

$$I(x,y) \approx I_0 \exp\left\{-\frac{(x-x_0)^2}{2\sigma^2}\right\} \exp\left\{-\frac{(y-y_0)^2}{2\sigma^2}\right\} \tag{3.1}$$

Due to the diffraction limit of light, two objects cannot be resolved individually if their mutual distance is less than the full-width-at-half-maximum ($FWHM$), which is dependent on the wavelength (λ) of the excitation light and the numerical aperture (NA) of the objective.

$$FWHM = \sigma\sqrt{8\log 2} \approx \lambda/(2NA) \tag{3.2}$$

By acquiring several images at a high acquisition rate, the centroids of each reporter can be linked between frames to generate its trajectory. This can be analyzed to understand the motional behavior of reporters [155].

3.3.1.1. SPT of polystyrene beads in agitated fluid

We extracted the trajectories of 200 nm fluorescent polystyrene beads (PBs; 200 nm FluoSpheres carboxylate, yellow-green 505/515, 2% solid from Invitrogen) from the image stacks using the TrackMate plugin in FIJI (for an example of extracted trajectories, see Figure 3.3) introduced by Tinevez et al. [160]. Before using the TrackMate plugin, all images in the stacks underwent background correction, Gaussian filter application, and contrast adjustments with FIJI to improve the PBs detection. The background correction was done by subtracting all images in the stacks using

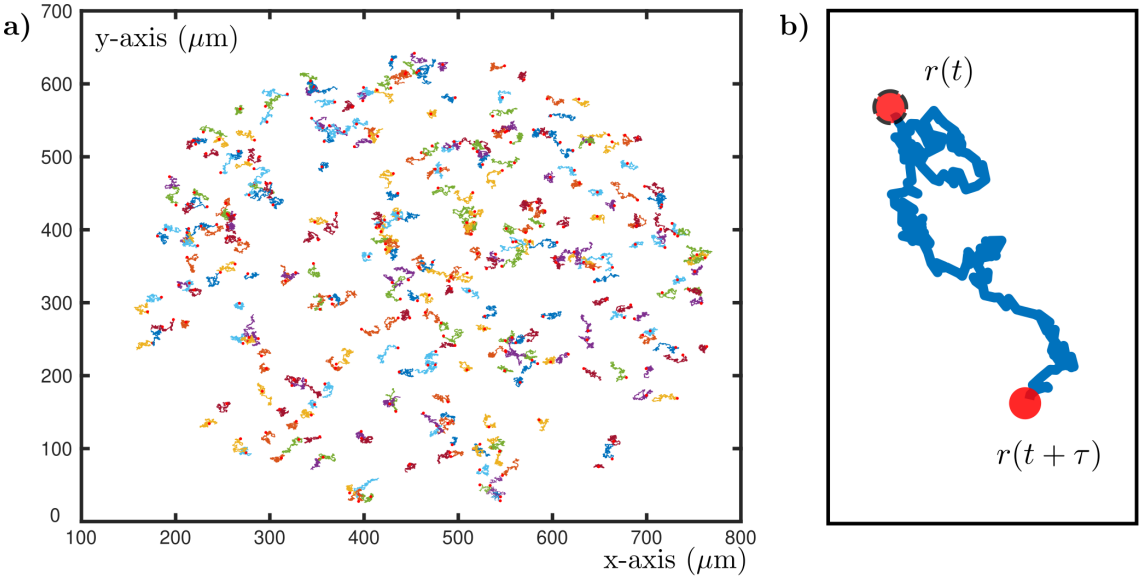

Figure 3.3.: SPT of PBs: (a) Trajectories of PBs inside the droplet at 0 Hz stirring frequency. **(b)** Representative trajectory (blue) with its initial ($r(t)$) and final times ($r(t+\tau)$) are represented using red circles.

mean pixel intensity from a homogeneous region around the droplet. The Gaussian filter has a radius of 0.65-pixel radius, and the contrast adjustment used saturated 0.3% of all the pixels. The particle localization in TrackMate was carried out using the *Laplace-of-Gaussian (LoG)* detector specifying the blob diameter (connected to FWHM of PBs) as 3.6 μm. The quality threshold of 15 was chosen to reduce background noise and unwanted detection. A median filter was used to reduce noise further and improve the signal-to-noise ratio. The detected PBs were linked between frames using the *simple linear assignment problem (LAP)* tracker with no additional filters. The maximum linking distance and gap closing distance in the LAP algorithm were set to 5 μm with zero gaps between the frames. This was to ensure that positions belonging to the same particle were linked. If aggregates were discovered during a visual inspection, they were removed from the list of trajectories. Spot statistics and tracks were exported from TrackMate as *.csv* and *.xml* files, respectively. Afterward, trajectories were converted to *ASCII* files in MATLAB for processing and handling. For each frequency, at least 246 trajectories, each with a minimum of 200 positions, were used for further analysis. For each condition, we cut the trajectories to obtain the same length for all analyses. The data analysis was done in MATLAB using custom-made scripts and the results are discussed in the section 4.6.

3.3.2. Voronoi tesselation

A Voronoi tesselation (VT) is a space partition into Voronoi cells based on a given set of generators (points) in that space. The Voronoi cells are polytopes (convex polygon in 2D) consisting of all the space closer to it than to any other generator. The VT was initially proposed by Peter Gustav Lejeune Dirichlet [161] and formally characterized by Georgy Voronoi in 1908 [162]. Different

names are designated to the same concept in different fields, such as Thiessen polygons, Dirichlet tesselation, Wigner-Seitz cells, Brillouin zones, etc. [163].

Mathematically, VT can be represented as a set of all Voronoi cell (V_i), which partitioned the space ($\Omega \subseteq \mathbb{R}^N$) with a set of n random distant points $\{z_i\}_{i=1}^n$. The points $\{z_i\}_{i=1}^n$ also known as the generators.

$$V_i = \{x \in \Omega, |x - z_i| < |x - z_j| \text{ for } j = 1, 2, ..., n \text{ and } i = 1, 2, ..., n \text{ with } j \neq i\} \quad (3.3)$$

Here $|.|$ denotes the Euclidean norm in $\mathbb{R}^N$ and clearly, we have $V_i \bigcap V_j = 0$ for $i \neq j$ and $\bigcup_{i=1}^k V_i = \Omega$ [164].

The VT was used in research to identify cells [165] and estimate parameters like perimeters, cell areas, etc [166]. In our work, we have used it to detect individual protocells (formed by self-organization in *Xenopus* extract) and extracted different parameters from it.

3.3.2.1. Protocell segmentation using Voronoi tesselation

Dr. Gires wrote the MATLAB script for the protocell segmentation, and I reused the codes to obtain the results discussed in this section.

As a first step, shading correction and merging of the images from the tile scan were performed using the Leica LAS X software. For the shading correction, a homogeneous tile outside the droplet without any debris from the same measurement was used to avoid imperfections when merging the tiles. The merging was done using auto-stitching, smoothing, and linear blending using the brightfield channel as a reference. The images from the Leica DMI6000B were resized by a factor of 1/4 in each direction to arrive at the same pixel dimension (3 μm/px) as Leica SP5 II. Subsequently, using the merged images, the time at which protocell formation begins and when it disappears was determined visually for each droplet preparation. The following operations were performed with MATLAB on the brightfield channel, which felt more accurate for segmentation than the fluorescence channel, to segment the protocells automatically.

- If different droplets in the same measurement were not separated during acquisition, a rectangular region of interest would be defined around the droplets for subsequent processing.
- The border of the extract droplet is automatically segmented, detecting the darkest pixels present at the boundary (see Figure 3.4a and b). If bubbles were present within the droplet, they were filtered out using the same method (used in one of the droplets). In cases where the droplet made contact with the tape, the contact region was manually segmented.
- The droplet image was binarized using the lowest of two thresholds obtained by Otsu's method (three-pixel classes with minimal intra-class variance using *multithresh* MATLAB function) as shown in Figure 3.4c and d.

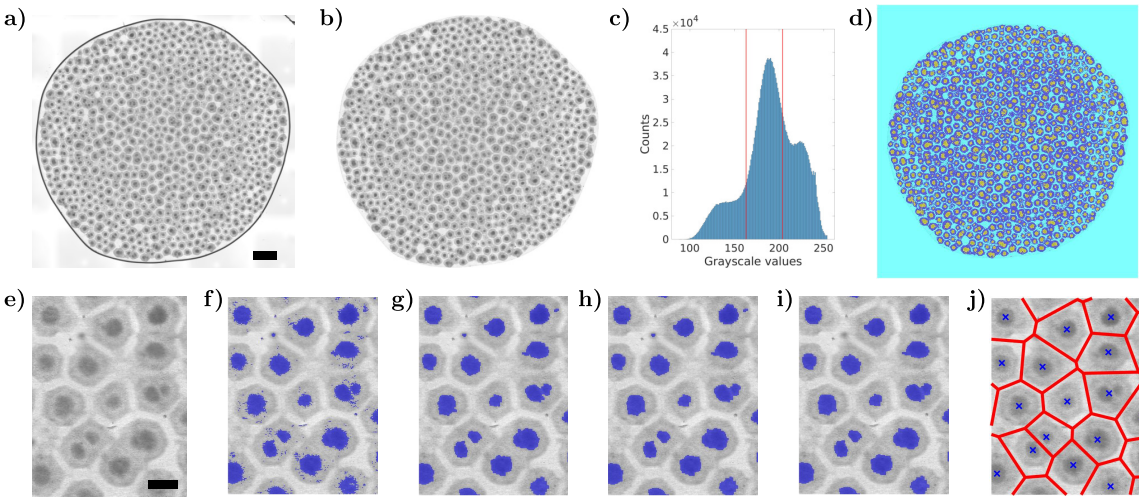

Figure 3.4.: Voronoi tesselation of protocell: **(a)** Representative merged tile scan brightfield image of a droplet with protocell patterning (0.1 μM at 175 min). **(b)** Same sample after masking. **(c)** Pixel grayscale value histogram inside the droplet with the two thresholds from Otsu's method, represented by red lines. **(d)** Multi-thresholded droplet with yellow, dark blue, and light blue colours representing the darkest, intermediate, and brightest pixels, respectively. **(e)** Zoomed region inside the droplet **(a)**. **(f)** Same image thresholded (as mentioned in **(c, d)**) with the darkest pixel in blue. **(g)** Image after hole filling and opening with a 3 x 3 structural element that removed the stray pixels. **(h)** After closing the image with the same structural element with an intermediate hole filling, creating a linked blue region. **(i)** The connected region was filtered using the area histogram, which removed the outliers. **(j)** Centroid positions of the connected region (blue crosses) with the associated Voronoi tesselation (red lines). The scale bar for **(a)** is 500 μm and for **(e)** is 100 μm.

- Additional filtering was then performed to obtain a single connected component of dark pixels (lowest threshold) within each protocell, defining its center. For this purpose, the following classical morphological operations were carried out in this order (see Figure 3.4f, g and h for illustration): Hole filling (with connectivity four), image opening (using a 3 x 3 square structural element), image dilation, hole filling, and image erosion using the same structural element. This allows the closing of some bright center areas that sometimes exist at the center of protocells.
- The connected sets of center black pixels (highlighted as blue) were filtered based on their area histogram (using a bin width according to Scott's rule, with area connectivity eight) to remove outliers (see Figure 3.4i for the filtered image).
- The centroid positions of these filtered connected components were calculated, and their Voronoi tesselation was computed (Figure 3.4j). Only the Voronoi cells, which were completely contained inside the droplets, were retained.
- The first tesselation for further analysis from each droplet was taken as the time step at which tesselation becomes accurate (by visual inspection). Also, a few intermediate steps were sometimes removed due to imperfections during visual inspections.
- Finally, different parameters were extracted from the tesselated images and used for further data analysis.

4

Creating magnetic stir bars for agitating biofluids

This chapter focuses on the effect of magnetic stirring in microdroplets. It starts with the synthesis and characterization methods used for the magnetic stir bars (MSBs). The later section discusses the development of the microscope-compatible stirring device and its controller to address the MSBs. Following this is the analysis of the rotational and magnetic characterization of the MSBs. The next section includes the stirring effect on diffusion, which was investigated using single particle tracking of polystyrene beads inside the aqueous droplet with MSBs. The final section focuses on the effect of MSBs agitation in the microtubule formed using Xenopus extract. Please note that references to figures in the Appendix section are indicated by a prefix 'A'.

4.1. Motivation and aim

The construction of a minimal compartmentalized system that mimics the living cell's characteristics and functions has attracted much interest in recent years [167–169]. High throughput cell-free extract or biofluid microdroplet system has been used to study various chemical and biological experiments. These include studying reaction kinetics [170], gene transcription in cell lysate [171, 172], for directed evolution experiments [173], reconstituting mitotic spindle [12, 13], and DNA amplification [174].

The inherent limitation of this microdroplet system was the slow diffusion-based mixing due to the laminar flows at this low Reynolds number regime. In addition, the macromolecular crowding in the cell-free extract causes slow or even anomalous diffusion, which can impede important reactions in the droplets [15, 16]. Our main aim was to develop a method to enhance the mixing within a biomimetic or biofluid droplet system and observe its effects on diffusion and dynamic self-organization.

There are several approaches have been adopted in the literature to enhance the mixing of microdroplets. For example, forcing the solution through complex channels [175], direct agitation with acoustic fields [176, 177] and even attempts to exploit an electric or magnetic field to drive tiny stir

bar encapsulated in the microdroplet [178–180]. Magnetic stirring is considered attractive for our experiments, as it has recently been shown that an ensemble of tiny stirring bars is able to generate a flow field inside the droplet and can easily be addressed with an external magnetic field [180].

There are several magnetic nanostructures discussed in the literature to induce mixing. For example, cobalt-based magnetic bars fabricated using laser micromachining [181], magnetic nanoparticles or polymer beads embedded with magnetic nanoparticles [182–186], star shaped micro stirrer made by soft lithography [187]. Here we followed a fairly straightforward method to create a magnetic stir bars by mimicking the natural synthesis of magnetosomes in magnetotactic bacteria [188, 189]. Also, by developing an inverted microscope-compatible stirring device, we aim to understand the effect of controlled stirring/agitation inside the biomimetic and *Xenopus* extract droplets.

4.2. Fabrication of magnetic stir bars

There were two steps involved in the synthesis of MSBs, namely ligand exchange of the commercially bought nanoparticles (NPs) and the creation of MSBs from this NPs. The chemicals used for these synthesis were oleic acid stabilized iron oxide (Fe_3O_4) nanoparticles (OA@NPs) dissolved in chloroform (SOR-30, Ocean NanoTech LLC), citric acid (Sigma Aldrich), dimethylformamide (Sigma Aldrich), dichlorobenzene (Sigma Aldrich), tetraethylorthosilicate (TEOS, Sigma Aldrich), and ammonia (Sigma Aldrich).

Ligand exchange

The first step in the synthesis of MSBs was the ligand exchange reaction of the commercially purchased suspension of spherical 30 nm OA@NPs. The 30 nm diameter of these ferrimagnetic particles were well in the range for a single magnetic domain. To make these NPs water-soluble, we performed a ligand exchange reaction which resulting in citric acid stabilized iron oxide NPs (CA@NPs) [179, 190]. For this purpose, 20 μL of the NPs suspension were mixed with 1.5 mL dimethylformamide, 1.5 mL dichlorobenzene and 150 mg citric acid in a 4 mL vial. The resulting black coloured solution containing vial (see Figure 4.1a) was sealed with Teflon tape and incubated in an oven at 100°C for 24 h. During this incubation period, the solution was vortexed 4-5 times to avoid clumping due to sedimentation. The solution turned brown (see Figure 4.1b) when the reaction was over and was centrifuged at 5,200 g for 5 min to remove the unreacted starting material. The CA@NPs (in the pellet form) obtained was redispersed in 1.5 mL deionized water and stored at 4°C.

Synthesis of magnetic stir bars

The MSBs were synthesized using the modified Stöber method [191] in the presence of a neodymium magnet. Stöber process was a sol-gel process well-known for the preparation of uniform sized silicon dioxide (SiO_2) particles [192] or for creating a uniform silica coating on various types of NPs

[193–195]. For our synthesis, a solvent mixture of 400 μL deionized water and 1 mL isopropanol was added to 200 μL hydrophilic CA@NPs in a 4 mL vial, followed by 10 μL TEOS (after 2 min sonication) and 40 μL ammonia. The resulting solution was vortexed for 5 s and immediately placed next to a neodymium magnet using a custom-made holder (see Figure 4.1c). During the incubation period of the synthesis, a static magnetic field from the neodymium magnet arranges the CA@NPs into chains, which were permanently fused with silica into magnetic rods. After an 18 h incubation period, the MSBs formed were concentrated at the vial wall next to the magnet. The transparent supernatant containing the unreacted starting material was carefully removed using a pipette. The MSBs obtained were mixed in 1 mL deionized water and centrifuged (at 2500 g for 6 min), and the purification process was repeated five times. Finally, the purified MSBs pellet was resuspended in 500 μL of deionized water in a new vial and kept at 4°C until use.

Discussion

The primary challenge we faced in the early stages of the project was related to the magnetic field arrangement required for MSBs synthesis. We understood that proper optimization of reaction conditions was necessary to achieve good MSBs. The magnetic direction, intensity, and field range significantly affected the MSBs synthesis. Synthesis without magnetic field results in silica-coated Fe_3O_4 NPs without any chain-like (or rod-like) structure [196, 197]. To tackle this issue, we tried different arrangements of the neodymium magnet to the vial (containing reactants). The most straightforward configuration was to keep the vial on top of the flat side of the cylindrical neodymium magnet. Unfortunately, the resulting MSBs were plagued with aggregates (Figure A.1a), possibly due to the sedimentation of reactants during the long incubation period. Here the magnetic field has a vertical orientation with some magnetic gradient. Therefore, NPs can assemble into vertical nanochain, but the magnetic gradient can induce the sedimentation of NPs to the bottom of the vial. Eventually, the adjacent nano chains can crosslink together with silica under the magnetic influence to form aggregated structures or thick MSBs.

The magnetic field strengths were also modulated using different sizes of neodymium magnets. But this also did not help to resolve the aggregation issue. The smallest magnet (10 mm diameter and 1 mm thickness) did not yield any MSBs. So we tried a different orientation of the neodymium magnet with respect to the vial. We changed the magnet to the side of the vial using a custom-made holder, resulting in MSBs with fewer aggregates. So we chose this orientation for further synthesis of MSBs used for different experiments discussed in the thesis. The neodymium magnet was aligned to have an equidistribution of the magnetic field throughout the solution in the vial. We kept the solution in the vial centered on the neodymium magnet, as shown in Figure 4.1c. The magnetic field strength chosen was sufficiently high (100-200 mT) to align CA@NPs to orient their easy axes and magnetization parallel to the magnetic field [198]. Due to the silica matrix, the magnetic orientation was fixed during the synthesis. Analyzing the wobbling motion of individual MSBs (one side attached to the coverslip) to theoretical predictions confirms its ferrimagnetic character [199], and it will be discussed in the later section.

The incubation time during the synthesis also affects the thickness of the silica coating over the MSBs. The thickness is reduced by reducing the synthesis time, similar to previous reports [179, 193]. Besides the incubation time, the amount of ammonia, TEOS, and CA@NPs influenced the width of the MSBs [180]. For us, 18 h incubation time with 40 μL ammonia and 10 μL TEOS and 200 μL CA@NPs yielded the best results. The synthesized MSBs were too small to be observed by the naked eye, but we saw blinking while keeping it on top of a rotational magnetic field (used a commercial stirrer). The blinking was due to light scattering. To characterize the MSBs, we used the scanning electron microscope and optical microscopy imaging. Later we used a stirrer compactable to the microscope to observe MSBs stirring, which will be discussed later.

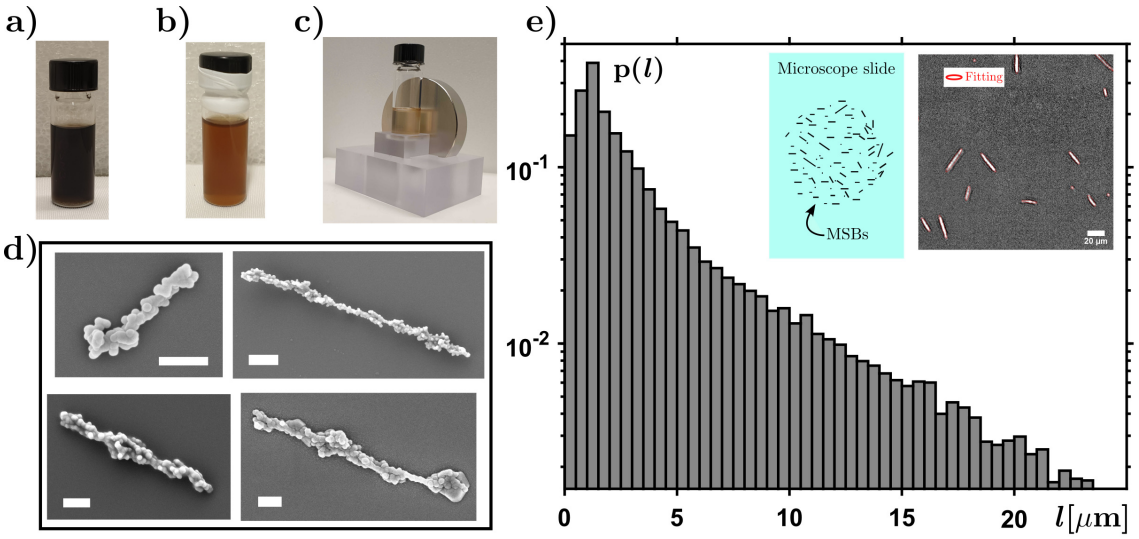

Figure 4.1.: MSBs synthesis and characterization: Suspension of Fe_3O_4 NPs **(a)** at the beginning and **(b)** at the end of ligand exchange reaction. **(c)** MSBs synthesis: The alignment of the neodymium magnet to the vial was fixed using a custom-made holder during the synthesis. **(d)** Scanning electron micrograph of representative MSBs. The scale bar for the images is 500 nm. **(e)** Length distribution ($p(l)$) of MSBs obtained from seven different batches (ensemble mean: $\langle l \rangle \approx 3.6$ μm). Insets contain the schematic of sample preparation for optical microscopy (MSBs dried on plasma coated microscope slide) and a cross-section of the sample with fitted MSBs (scale bar is 20 μm).

4.3. Shape and size characterization of MSBs

The MSBs synthesized using the modified Stöber method have distribution in their length and thickness, and a proper understanding of the distribution is necessary to use them in the experiments. We have carried out scanning electron microscope (SEM) and optical microscope imaging on these MSBs samples. Postdoctoral researcher Dr. Pierre-Yves Gires made a MATLAB code to detect MSBs from these images and extracted their size distribution. These results were published in our article in Nature Scientific Reports [200]. The results discussed in this thesis are from the re-analysis I have performed using the MATLAB code from Dr. Gires.

4.3.1. Scanning electron microscope imaging of MSBs

Sample preparation

The samples for the SEM images were prepared on cleaned silicon (Si) wafers. The Si wafers were cleaned as follows: The Si wafers were first washed with acetone and kept in a beaker containing acetone. They were vortexed for 5 s and kept in an oven at 55°C for 10 min. Then it was rinsed in deionized water and dried with N_2 gas. Finally, it was kept in the oven at 75°C for 10 min to have it dried completely and was stored in a Petri dish to avoid contamination. Immediately before SEM sample preparation, the Si wafer was cleaned using N_2 gas, and its surface was made hydrophilic with plasma (20 s plasma exposure at 920 mTorr and HIGH intensity). Then the Si wafer was placed on the magnetic stirrer, and 0.5 μL of three-fold diluted MSBs solution was poured over it under the fume hood. The Si wafer was left in this dust-free environment overnight to dry.

SEM imaging

The dried sample was then mounted on a standard SEM sample holder with conductive carbon adhesive tabs (Plano GmbH). It was sputtered with 2 nm platinum (using Cressington HR 208 sputter coater with Cressington MTM-20 thickness controller). The samples were examined using a Zeiss scanning electron microscope (Zeiss Ultra Plus: FE-SEM with Schottky-field-emission cathode, in-lens detector, and SE2 detector) using an accelerating voltage of 3 kV. The samples were looked at different resolutions to obtain a clear picture of their length and width distribution. It also gives us a clear insight into the successful synthesis of individual MSBs. The bright rod-like structures visible in the images were the MSBs (see Figure 4.1d).

4.3.2. Optical microscope imaging of MSBs

Sample preparation

Imaging samples were prepared on pre-cleaned, plasma-treated coverslips (Menzel Gläser, 24 x 60 mm, #1.5 thickness). The coverslips were pre-cleaned with isopropanol using a cotton tissue and dried under N_2 gas. Subsequently, they were exposed to plasma to make the surface hydrophilic (20 s exposure at 920 mTorr and HIGH intensity). 0.5 μL of 5 times diluted MSBs solution were pipetted on top of this coverslip and allowed it to dry under the fume hood in a dust free environment. A schematic of the prepared sample is in the inset of Figure 4.1e.

Optical imaging

The dried samples were imaged using a Leica DMI6000B inverted microscope (hereafter referred to as SD microsope) with a 20x objective (HC PL APO 20x/0.75 IMM CORR CS2) and a 1,392x1,040 pixel camera (Leica DFC360 FX), featuring a spatial resolution of 600 nm. The Leica LAS X software's automatic tile scan function captured the entire sample area under the brightfield mode

while maintaining aperture 13 and field diaphragm 46. Other parameters, like exposure, gain, etc., were adjusted based on the imaging sample. The automatic tile scan feature creates a single image by merging images taken at different sample positions. Here we had to visually select the borders of the sample containing MSBs and adjust the focus based on multiple regions in the sample (here, we used a nine-point focus). The software then adapts the focus throughout the sample and yields a merged image. The dark areas in these brightfield images correspond to the MSBs. Pretreatment of the glass surface with plasma and avoiding dust helped minimize irregular drying and obtain well-separated MSBs, which are evident in the microscopy images.

4.3.3. Image analysis and discussion

The SEM images of the MSBs give us an overview of their shape and size distribution. All the MSBs appear to have a slender, rod-like shape. More precisely, we observed MSBs with a typical diameter in the range of 300 nm, and length ranges from a few 100 nm to several micrometers. Longer MSBs appeared to be more bulky (as shown in the Figure 4.1d). During the initial synthesis, we also observed aggregated structures on the SEM images (Figure A.1a), which we were able to reduce by improving the synthesis protocol. The most significant improvement in the protocol was in the magnetic field arrangement, as mentioned in the section on the synthesis of the MSBs.

In order to have a better understanding of the MSBs length distribution, we have utilized the brightfield images from the optical microscope. As mentioned earlier, we could detect MSBs as dark areas in the bright background, which were then automatically detected using the MATLAB code developed by Dr. Gires. In detail, the code works as follows: The image was first thresholded and then inverted after subtracting the background. Subsequently, the noise was coarsely filtered by averaging a square region around each pixel. Finally, the connected regions fitted with an elliptic function (a small fitted region is given in Figure 4.1e inset), and the long axis of these ellipses were used as a measure for MSBs length, l. All the lengths below 500 nm were integrated into a single bin to consider the diffraction limit.

The resulting probability density function of MSB lengths, $p(l)$, covered a length range from few hundred nanometers up to 20 μm, following roughly an exponential profile (see Figure 4.1e). As expected for an exponential probability distribution, the mean length $l < 4$ μm was almost identical to the standard deviation ($\sigma(l) \approx \langle l \rangle$). Notably, MSBs samples from different synthesis did not show significant deviations from each other. Thus, a large collection of slender MSBs with lengths $l < 10$ μm was reliably obtained with our synthesis approach.

4.4. Stirring of MSBs using different stirring devices

The main idea of this project was to study the stirring effect in biomimetic systems, and as a first step, we successfully synthesized MSBs, as discussed in the previous section. However, incor-

porating these MSBs in tiny droplets and introducing the rotational motion, along with real-time observation, was still challenging. In that regard, we employed different stirring devices and strategies. In this section, I will discuss the different magnetic stirring devices used and developed as part of the thesis. I also discuss some earlier experiments carried out with these devices to study the stirring of MSBs.

4.4.1. Commerical magnetic stirrer

The first device we used to check the stirring of MSBs was a commercial stirrer from VWR (VWR VMS-C7 S1 digital hotplate stirrer). Since the MSBs were not visible to the naked eye and the stirrer was too large for a microscope, we relied on the effect of stirring. The effects observed with the commercial stirrer are given below.

Blinking MSBs: The first effect we noticed with the MSBs was blinking. The vial containing the MSBs was held on the stirrer, and the rotating magnetic field was applied. During stirring, the solution blinked synchronously with the rotating magnetic field (similar to the observation of [179]). The scattering of the light upon the MSBs rotation caused this effect and was also inductive of the stirring capability of MSBs.

Ink mixing in droplets: A microscope slide was placed on the stirrer with a Teflon sheet on its top. Then two 10 μL droplets were pipetted on this Teflon sheet, one containing MSBs and the other with pure Milli-Q water. Afterward, the stirrer was switched ON and started the rotation. Subsequently, simultaneously injected 2 μL of the ink into both droplets. We observed a swirling motion inside the droplet containing MSBs. However, the other droplet showed a normal spreading of the ink. This also validated the stirring action of the MSBs.

Besides the above experiments, we also used the VWR stirrer to prepare SEM and optical microscopy samples (discussed in the section 4.3). The samples were dried on the stirrer while keeping the rotation OFF. The magnet inside this commercial stirrer helps align the MSBs in the field direction. This reduced the uneven orientation of MSBs in the dried samples, which is evident from SEM imaging (Figure A.1b).

From the simple experiments discussed, we validated the stirring action of the MSBs. However, observing its action in detail was challenging. So we bought a small stirrer compatible with the optical microscope. The experiment performed with that stirrer is discussed in the following sections.

4.4.2. 2mag stirrer and controller

The stirrer compatible with the microscope was purchased from 2mag AG (MIXdrive 1 XS, hereafter mentioned as 2mag stirrer). The 2mag stirrer has a dimension of 48x48x18 mm with an approximate weight of 360 g (Figure 4.2b). As per the company datasheet, the rotating field gener-

ation was based on the "inductive 2mag-Magnetic-Drive concept" [201]. The 2mag stirrer consists of four inductive coils, providing an alternating current with a phase difference that yields the rotating magnetic field. We bought a driver from 2mag (MIXcontrol eco DINrail, referred to as 2mag controller later on) to operate the stirrer (Figure 4.2a). The 2mag controller has a maximum stirring power of 10 W and can generate stirring frequencies from 120 to 1200 rpm (2-20 Hz). The frequency modulation was done by changing the voltage from 0-10 V using an external power supply (QL355P, Aim-TTI) connected to the 2mag controller [201]. We also studied the magnetic field produced by the 2mag stirrer with the help of a Hall effect sensor (SS495A1, Honeywell) connected to an Arduino (see section A.3 for details). With the 2mag controller, the 2mag stirrer created a magnetic field of 30 mT.

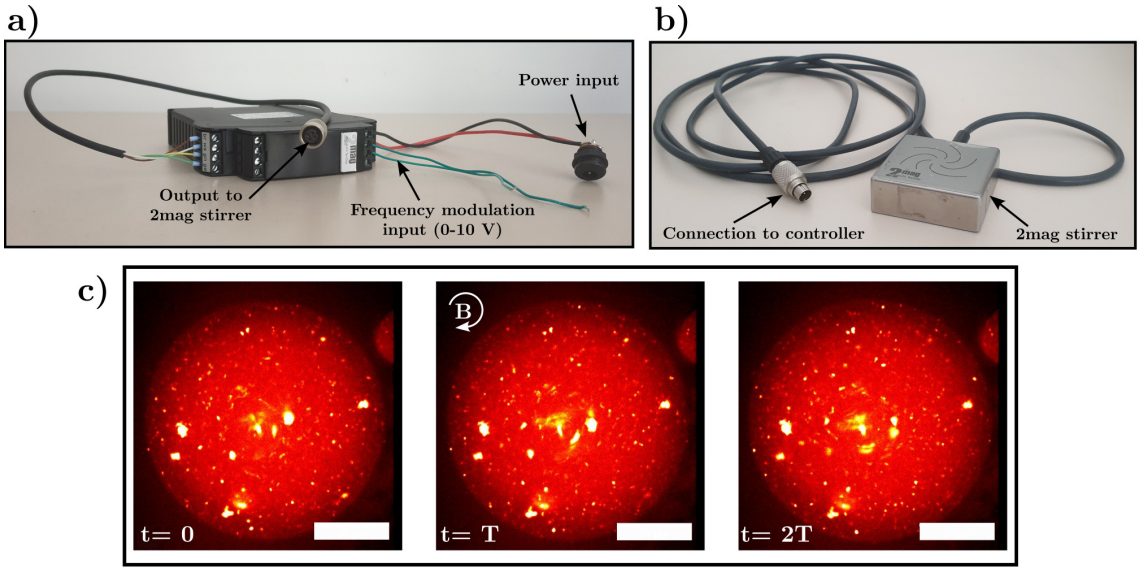

Figure 4.2.: 2mag controller and stirrer: **(a)** 2mag controller: The output of the 2mag controller is colour-coded and connected with a cord with one end having colour-coded wires. The power supply to control the rotation frequency is connected to the blue wires. The other connection (power input) is for 2mag controller power supply. **(b)** 2mag stirrer with its connector. **(c)** Droplet containing fluorescent beads and MSBs rotating at a frequency (f) of 10 Hz (time period, T = $1/f$ = 0.1 s). The bright spots visible in the droplet are fluorescent beads. Scale bar is 30 μm.

4.4.2.1. Experiments with 2mag controller

To verify the MSBs stirring efficiency of the 2mag stirrer and control system in small volumes, we used droplets containing MSBs and 200 nm polystyrene beads.

Sample preparation

The sample was prepared by mixing 6.25 μL of MSBs suspension with 144 μL of Mili-Q water and 50 μL of fluorescent beads suspension (200 nm FluoSpheres Carboxylate, yellow-green 505/515, 2% solid from Invitrogen; diluted 1:1000 and sonicated for 30 min). The droplets used for imaging were prepared using the T-junction microfluidic chip (as discussed in the section 3.2.5). Briefly, 30 μL of the suspension containing MSBs and fluorescent beads was added to the syringe used for

the dispersed phase. Then, the droplets were generated at a flow rate of 15 μL/h for the oil and 10 μL/h for the suspension. For the experiment, 10 μL of these droplets were added to an IBIDI chip containing Squalene oil (just enough to cover the droplets).

Imaging and stirring

Imaging was performed with the SD microscope equipped with a spinning disc unit (Yokogawa, CSU-X1) using an 63x oil immersion objective (HCX PL APO 63x/1.4) and an EM-CCD camera (Roper Evolve 512, 512 x 512 pixel, 0.2 μm per pixel, set to 16 bit mode). The sample was mounted on the SD holder and the 2mag stirrer (attached to a ruler and adjusted its height using spacers on the sides) was aligned on top of it. The 2mag stirrer was centered on the IBIDI chip (and thus the magnetic field) by visual observation using the transmitted light of the SD microscope. The fluorescent beads were excited at 488 nm and the fluorescence was detected in the range 500-550 nm.

Observation and discussion

As the MSBs are not labelled, we relied on the movement of the fluorescent beads to detect the stirring effect of the MSBs. That said, sometimes we observed MSBs as shadows in the fluorescence background of the beads. After turning on the rotating magnetic field, we observed the rotational motion of the fluorescent beads (see Figure 4.2c). We also observed an overall beating effect in the droplet that modulates with the stirring frequency. Both indicated that the MSBs could successfully stir/perturb small droplets. However, we noticed that the stirring effect induced in the droplet was too vigorous at the frequencies achievable with 2mag controller. Since we wanted to study a low-frequency regime and 2mag controller cannot go below 2 Hz, we developed a controller with the help of Mr. Thomas Braun (electronic workshop, University of Bayreuth) to investigate the low-frequency regime in a controlled manner.

4.4.2.2. Electronic workshop controller

Mr. Braun designed and programmed the controller after checking the 2mag controller outputs. The 2mag controller has four outputs that connect the two inductor pairs in the 2mag stirrer. The rotating magnetic field was created by using a phase shift of 90° in the current going to coil pairs. The magnetic field's rotation frequency was modulated by changing the current period. In the 2mag controller, we used a voltage input to modulate the magnetic field rotation frequency (1 to 10 V yields 2 to 20 Hz). The current output from the controller to the stirrer was given as a pulse width modulation (PWM) signal. The frequency of the PWM was responsible for creating a smooth rotating magnetic field. The 2mag controller contained a firmware in the microchip that restricted the low-frequency regime. Due to this reason, a controller was created using similar principles, which can go even to the lower frequencies. We later refer to this new controller as the electronic workshop controller (EW controller).

The central part of the EW controller was the power stage and the microcontroller. The microcontroller was programmed using the MPLAB development ecosystem with the help of a Microchip's PICkit™ 3 In-Circuit Debugger/Programmer. The EW controller can generate magnetic field rotation frequency from 0.01 to 10 Hz. Additionally, it can modulate the magnetic field intensity from 0 to 30 mT. The two knobs outside the protection casing were used to modulate the magnetic field rotation frequency ($FREQ$) and intensity ($CURRENT$). EW controller also had an inbuilt LCD that showed the output frequency and the field intensity. The controller was working on a 10 V power supply (QL355P, Aim-TTI with max. current 2 A) and had external switches to turn it ON and OFF. To avoid confusion, the four outputs of the EW controller (see Figure 4.3a and 4.5a) were colour-coded, similar to 2mag controller.

4.4.2.3. Experiments with EW controller

Sample preparation

The sample used contained 50% glycerol and it was prepared by mixing 251 mg of glycerol with 19 μL of 200 nm fluorescent beads suspension (diluted 1:1000, sonicated for 30 min, vortexed for 5 s before addition), 211 μL of Milli-Q water and 20 μL of MSBs suspension. For the experiment, 1 μL of this suspension was pipetted to the bottom of a glass bottom 8-well IBIDI chip containing 200 μL Squalene oil (see Figure 4.3b for a schematic representation of the sample).

Imaging and stirring

The sample was imaged with the same SD microscope with 20x objective (for details see section 4.3.2) and Leica DFC360 FX camera. The fluorescent beads were illuminated using a 480 $\pm$ 20 nm filter, and the fluorescence detection range was 527 $\pm$ 15 nm. The sample was first imaged in brightfield in a tile scan mode to see the overview of the droplet. Then placed and aligned the 2mag stirrer on top of the sample as discussed in the section 4.4.2.1. The sample was stirred using the EW controller at 50% magnetic field intensity and fluorescently imaged.

Discussion

The brightfield imaging with the 2mag stirrer enabled us to visualize the droplet shape and the uniform distribution of the MSBs. During the stirring experiments, we relayed upon the fluorescence of the fluorescent beads to observe the stirring action of the MSBs (as a shadow in the fluorescence background). In spite of the highly viscous nature ($\approx$ 5 mPas) of the environment, the MSBs were able to rotate with the field generated by 2mag stirrer using the EW controller. Because the EW controller can generate lower frequencies, we first investigated them. The MSBs were able to follow the low frequencies and they were rotating synchronously with the external driving frequency. Figure 4.3c represents the synchronous rotation of MSBs at 0.05 Hz, where despite the size, all the MSBs were following the 2mag stirrer driving frequency. Meanwhile, as the frequency

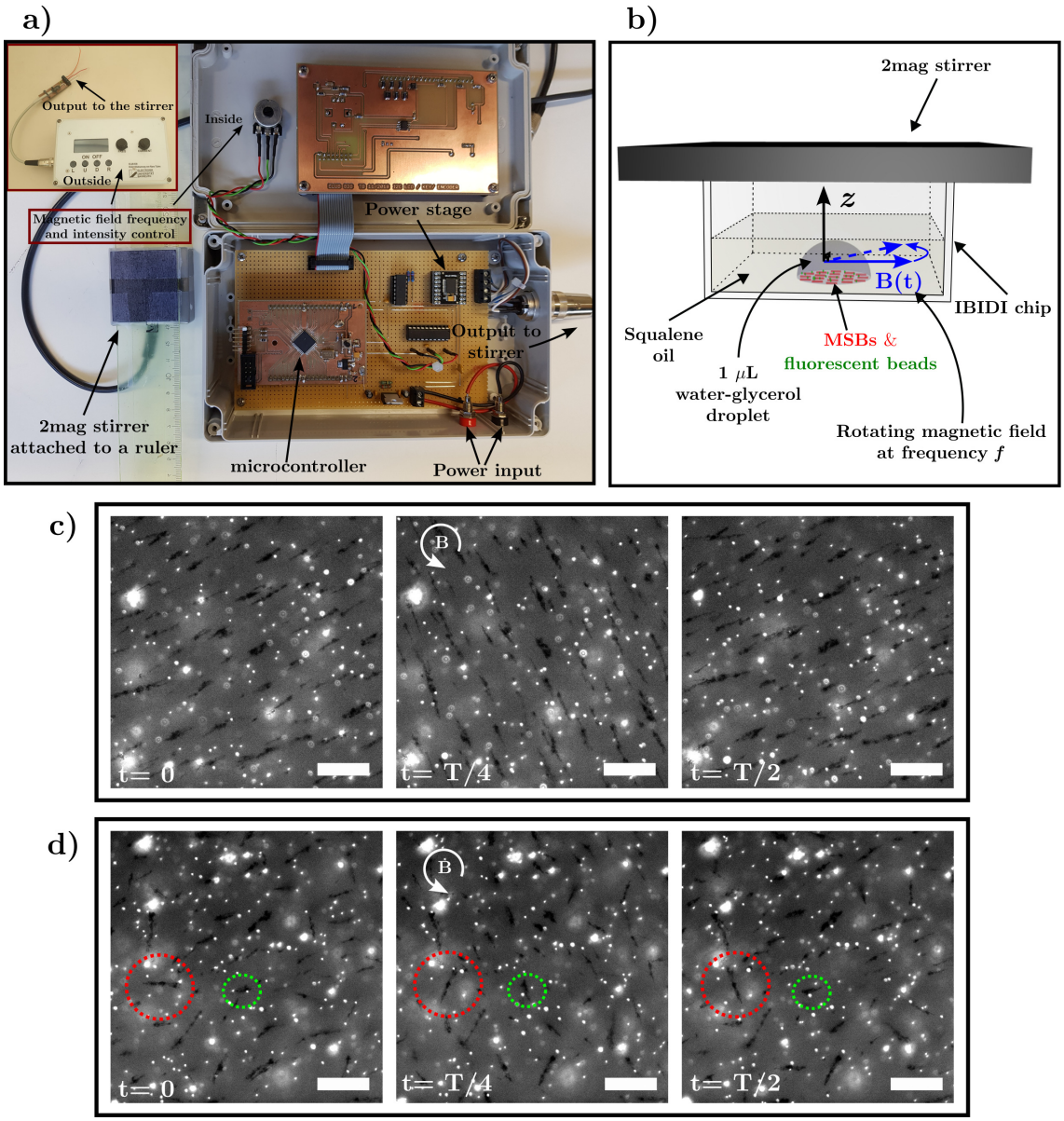

Figure 4.3.: EW controller and MSBs stirring: (a) EW controller with its main components labelled. The four output wires (see figure inset) are used to connect 2mag stirrer. Two knobs are used to control the frequency and intensity of the rotating magnetic field (see figure inset). **(b)** A schematic representation of the chamber used for the stirring experiments: water-glycerol droplet contains fluorescent beads and MSBs in an IBIDI chip filled with Squalene oil. The MSBs are addressed with a rotating magnetic field using the 2mag stirrer aligned on top of the IBIDI chip. **(c)** Representative images of the MSBs rotating at a frequency of 0.05 Hz. The MSBs are rotating synchronously with respect to the external field. **(d)** Representative images showing the asynchronous rotation of the MSBs at 0.4 Hz. The green circle contains a small MSB that follows the external magnetic field. However, the large MSB in the red circle does not follow the external magnetic field. Scale bar for **(c, d)** is 20 μm and T represents the time period.

increased, we noticed that the larger ones began to lag behind the driving frequency. For example, when we looked at 0.4 Hz (see Figure 4.3d), the larger MSBs (inside the red circle) lag behind the driving frequency, whereas the smaller ones (inside the green circle) were in sync. Together with the chaotic movements of some MSBs around, these created an asynchronous regime. At higher

driving frequencies, the smaller ones also become out of sync. Despite their asynchronous nature, these regions were intriguing because chaotic movement can disrupt the local environment.

The experiment revealed that the 2mag stirrer can effectively address the MSBs. However, observing the MSBs while stirring was difficult, limiting their use in several experiments. To address this issue, we fluorescently labelled the MSBs, which is discussed in the following section.

4.4.2.4. Fluorescence labelling of the MSBs

As mentioned earlier, we observed the MSBs as dark regions in brightfield imaging or as shadows on bright fluorescent backgrounds in fluorescence imaging. We wanted to observe MSBs and study their effects while stirring biomimetic fluids. Due to the current configuration of the 2mag magnetic stirrer, it was out of scope to use the transmission brightfield mode, and we were limited to fluorescence imaging. As discussed before, a uniform fluorescent background is necessary to detect these MSBs shadows. But we have experienced difficulty in identifying MSBs in weak fluorescence backgrounds, close to bright fluorescence sources, and in encapsulated droplets. In order to overcome this limitation, we have fluorescently labelled the MSBs with fluorescein isothiocyanate (FITC) or ATTO 390. In both cases, we had to go through a two-step process; the first step was to link the dye with (3-aminopropyl)triethoxysilane (APTES) and the second step was the synthesis of the fluorescently labelled MSBs using the APTES linked dye. APTES is one of the most widely used organosilanes, and its amino group facilitates subsequent functionalizations for a variety of applications, e.g. glycopeptides extraction using functionalized NPs [202], preparation of a biosensor platform to detect streptavidin [203], etc. The detailed protocol used for MSBs fluorescence labelling is discussed below.

4.4.2.4.1. Fluorescent labelling of MSBs with FITC

We considered FITC as the first candidate for the fluorescent labelling of MSBs. It is a derivative of fluorescein and has been used commonly in a variety of fluorescent labelling applications [204, 205]. The excitation/emission peak of FITC at 495/517 nm and can be linked using its reactive isothiocyanate group that can binds to amino, sulfhydryl, imidazoyl, tyrosyl or carbonyl groups [206]. The two step labelling protocol discussed below to link FITC with MSBs were inspired from Wacker et al. [207].

Linking FITC with APTES

In order to attach FITC to APTES, 0.13 g of APTES (Sigma Aldrich) was combined with 1 mg of FITC (Sigma Aldrich) in an opaque 2 mL vial containing 1.3 mL of absolute ethanol over 20 h using a thermomixer at room temperature. The vial was filled with N_2 gas and wrapped with aluminum foil before being kept in the thermomixer to prevent interactions with air and light. These FITC linked APTES (FA) was kept at 4°C and used for FITC labelled MSBs synthesis.

Synthesis of FITC linked MSBs

The synthesis of FITC labelled MSBs (FITC-MSBs) was carried out similar to that of MSBs synthesis discussed in section 4.2. In detail, 100 μL of unlabelled MSBs added to a solvent mixture of 1 mL isopropanol and 500 μL deionized water in a 4 mL vial. 10 μL of TEOS (after 5 s vortexing), 10 μL of FA, and 50 μL of ammonia (29% solution) were added to the solution and vortexed for 5 s. Then it was held near the neodymium magnet with the custom-made holder and covered with a cardboard box to avoid exposure to light. After 8 h of incubation, the FITC-MSBs accumulated on the wall near to the magnet. To purify the FITC-MSBs, the supernatant was carefully removed, 1 mL of deionized water was added, and the FITC-MSBs were centrifuged five times (3000 g for 5 min). The FITC-MSBs pellet obtained after purification was dissolved in 100 mL of deionized water and stored at 4°C in an opaque 2 mL vial.

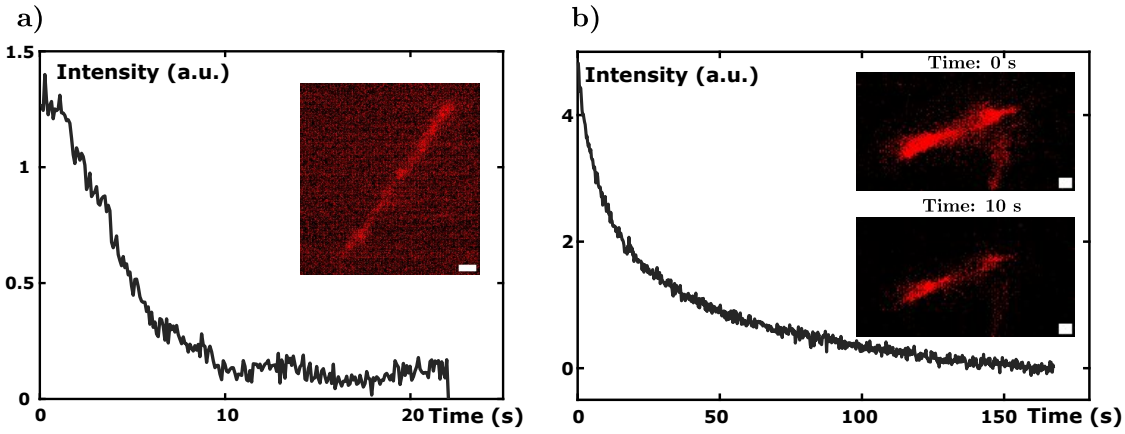

Figure 4.4.: Photobleaching curve of FITC and ATTO390 linked MSBs: Photobleaching curve of **(a)** FITC-MSBs and **(b)** ATTO-MSBs. Inset containing the fluorescent images of the **(a)** FITC-MSBs at 0 s and **(b)** ATTO-MSBs at 0 s and 10 s. Scale bar for the figures in the inset are 1 μm.

4.4.2.4.2. Fluorescent labelling of MSBs with ATTO 390

ATTO dyes are a new generation of fluorophores from ATTO-TEC GmbH characterized by its high extinction coefficient (strong absorption), high fluorescence quantum yield, excellent photostability and good water solubility. ATTO dyes are available in all the necessary emission/excitation ranges useful for life science applications. Also they are available in a range of conjugated forms useful for easy coupling with molecules. As mentioned before, these ATTO dyes are more photostable compare to its predecessors (FITC, AlexaFluor, etc.) [208]. The direct alternative for FITC is ATTO 488, but we have chosen ATTO 390 for labelling MSBs. The rationale for this was to free up the visible spectral region with higher excitation wavelength for further possible markers, i.e. the usual markers such as EGFP or rhodamine can be used together with MSBs. Here we used the NHS-ester derivative of the ATTO 390 which reacts with primary amines in physiologic to slightly alkaline conditions to yield stable amide bond [209, 210].

Linking ATTO 390 with APTES

To couple ATTO 390 with APTES, 0.4 mg of NHS ester derivative of ATTO 390 was dissolved in 196 μL of DMSO in an opaque 2 mL vial, and 4 μL of diluted APTES (diluted 10-fold in DMSO) was added. The resulting solution was immediately covered with aluminum foil to avoid exposure to light and kept overnight at 300 rpm at room temperature in a thermomixer. The resulting ATTO 390 linked APTES (AA) solution was stored at -20°C until use.

Synthesis of ATTO 390 linked MSBs

The synthesis and purification steps of MSBs labelled with ATTO 390 (ATTO-MSBs) was similar to that of FITC-MSBs discussed in the section 4.4.2.4.1, the only difference being that AA was used instead of FA. The ATTO-MSBs obtained after the synthesis was dissolved in 100 μL deionized water and stored at 4°C until use.

Discussion

We successfully linked both FITC and ATTO 390 dyes to the MSBs, which was evident from the fluorescent measurements (see Figure 4.4 inset). We used the IBIDI chambers with glass bottom to observe the fluorescent MSBs. The observation sample was made by pipetting 0.5 μL of the fluorescent MSBs solution in 200 μL of Squalene oil (Sigma Aldrich) in the IBIDI chip. The sample was observed using the SD microscope with a 20x objective (for details, see section 4.3.2) and Leica DFC360 FX camera. We stirred the MSBs using the 2mag stirrer with our EW controller.

We were able to stir the fluorescent MSBs using the 2mag stirrer. However, both dyes have undergone significant photobleaching in a short time. In both FITC and ATTO 390 cases, we have tried to reduce the excitation power to limit photobleaching (need a minimum power due to low signal-to-noise ratio (SNR)). Nevertheless, we couldn't overcome the photobleaching. The FITC-MSBs were photobleached to almost no fluorescence in 10 s (Figure 4.4a). The ATTO-MSBs were comparatively stable and had a better fluorescent signal. Although, the fluorescent signal becomes halved in about 12 s and becomes difficult to detect after 50 s due to the bad SNR (Figure 4.4b).

However, we utilized these fluorescent MSBs to study stirring in the small droplets (similar sample as discussed in section 4.4.2.1) and succeeded in following them in fluorescent microscopy. We were able to observe the synchronous and asynchronous regimes in the droplets, as discussed in the section 4.4.2.3. However, long measurement with MSBs was difficult due to the significant photobleaching. Additionally, we observed that the ATTO-MSBs started sticking to the glass bottom of the IBIDI chip (bulk samples). While studying the issue, we noticed that increasing the system's pH reduced the sticking behavior and allowed the MSBs to rotate freely. The pH value at which the MSBs started to rotate was 10, which is not suitable for most biological experiments. In addition, we had problems with the alignment of the 2mag stirrer on the sample. This was time consuming (causing problems for time-sensitive experiments), and occasionally misalignment caused us

to abort the experiments. Alignment problems usually result in flow in the sample, causing the region of interest to move out of the field of view during imaging. Therefore, we had to rethink the stirring strategy for further experiments and develop a device that could also use the transmission mode of the microscope.

4.4.3. Helmholtz coil based stirrer

The new stirrer we constructed was based on Helmholtz coils. The Helmholtz coil, named after the German physicist Hermann von Helmholtz, comprises two coaxial coils of equal radius placed parallelly at a distance equal to the coil's radius. When current flows through them in the same direction creates a uniform magnetic field in the space between the coils. When two Helmholtz coils were arranged orthogonally to each other and supplied with a current phase-shifted by 90°, a rotating magnetic field was generated at the center of the Helmholtz pairs. The frequency of the rotating magnetic field can be modulated with the frequency of the input current. The Biot-Savart law can be used to calculate the uniform magnetic field produced at the center.

Our Helmholtz stirrer (later on, mentioned as stirrer) consisted of custom-built coils, with each coil containing 100 loops of 0.5 mm diameter copper wire wound (using a winding machine) onto a 3D-printed bobbin having a inner diameter of 30 mm. The Helmholtz coil, as we know, is made up of two identically connected coils with current flowing in the same direction. So we connected one end of the copper wire from the two coils together, resulting in a continuous flow of current in the same direction after assembly. The other end of the coil's copper wire was connected to the stirrer controller (for example, to the output of the EW controller). We need two Helmholtz coils to generate the rotating magnetic field, as previously stated. The stirrer was made by screwing the Helmholtz coils orthogonally in a custom-made aluminum holder. The sample can be inserted into a groove in the center of one of the Helmholtz coils' 3D-printed bobbins. The stirrer was operated using the EW controller or a custom made Arduino based controller.

4.4.3.1. EW controller

The connection between the EW controller and the stirrer was similar to the section 4.4.2.2 (see also Figure 4.5a). In detail, the four input wire (colour coded) from the stirrer was connected to the controller using the crocodile cables. The connection to the coils belonging to the same Helmholtz coil was also colour coded (white for one Helmholtz coil, red for the other). The EW controller was then connected to a 10 V power supply with a maximum current of 2 A. The magnetic field intensity produced by the stirrer was controlled using the $CURRENT$ knob. The field it could produce was measured using the Hall effect sensor at 20% current was 0.6 mT (see section A.3 for details). Since the field intensity is directly proportional to the current, we used a simple MATLAB fit to find the corresponding field intensity for the measurements. The frequency of rotation was controlled using the $FREQ$ knob in the controller. There was some issue with the EW controller in

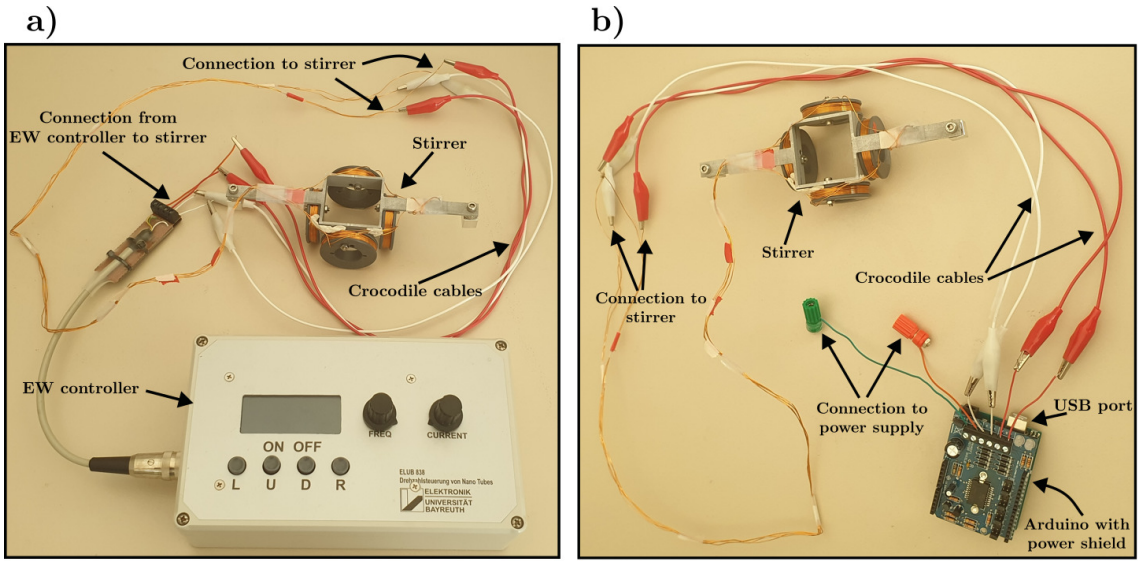

Figure 4.5.: Helmholtz coil based stirrer with its controllers: The rotating magnetic field in the stirrer was created using **(a)** EW controller and **(b)** Arduino controller. Crocodile cables were used in both cases to connect the controller output to the stirrer. The colour code (red and white) was used to distinguish between the two Helmholtz coil connections; the same colour cable was used to connect both ends of a single Helmholtz coil. In **(a)**, the frequency was controlled using the $FREQ$ knob and magnetic field intensity using the $CURRENT$ knob. In **(b)**, the frequency was controlled by modifying the compiled program in Arduino. Magnetic field intensity was adjusted by changing current in the power supply.

later experiments with *Xenopus* extracts, and it couldn't reach higher fields, so we used an Arduino-based controller for that cases.

4.4.3.2. Arduino controller

The main components of this controller includes the Arduino UNO Rev3, motor power shield (VMA03, Velleman N. V.) and the power supply (QL355P, Aim-TTI). The Arduino controller was made by mounting the motor power shield on the Arduino UNO. This controller was powered by an external power supply (Figure 4.5b to see the wire with the banana jack used for the power connection), which allowed it to generate a higher output power and thus a stronger magnetic field. The maximum voltage used for this controller was 16 V and the current was varied to produce different magnetic fields. The magnetic field generated at 2 A was 1.9 mT (using the Hall effect sensor as described in section A.3).

The motor shield has two channels (A and B), and each channel has a (+) and (-) screw terminal. These channels can operate independently, and we used them to drive the Helmholtz coils (one channel for one Helmholtz coil). The wires from the channels are colour-coded (red for A and white for B) and connected to the Helmholtz coil using similarly colour-coded crocodile cables (see Figure 4.5b). The Arduino was programmed using Arduino IDE to create the rotating magnetic field. This program generated PWM sinusoidal output having a phase lag of 90° between the channels (see section A.5 for the Arduino code). The frequency of rotation depends on the compiled

code. To change the rotation frequency, we must recompile the code with a new frequency into Arduino. The controller needed to be disconnected from the computer and switched off the power supply to stop the rotation. It is better to avoid higher current and longer stirring experiments with both controllers to prevent the stirrer from heating up.

4.5. Rotational and magnetic characterization of MSB

We understood from the discussion in the previous sections that the MSBs could be driven inside the droplets using our magnetic stirrers. However, an in-depth study of MSB rotation dynamics and its magnetic behaviour have not been discussed yet, and this section explores these aspects. For these experiments, we addressed the MSBs in aqueous droplets using a rotating magnetic field utilizing the real-time brightfield imaging capability of the Helmholtz stirrer along with its EW controller. The experiments and analyses discussed in this section were carried out jointly with Dr. Gires. Some of the details discussed in this section have already been published in Nature Scientific Reports [200].

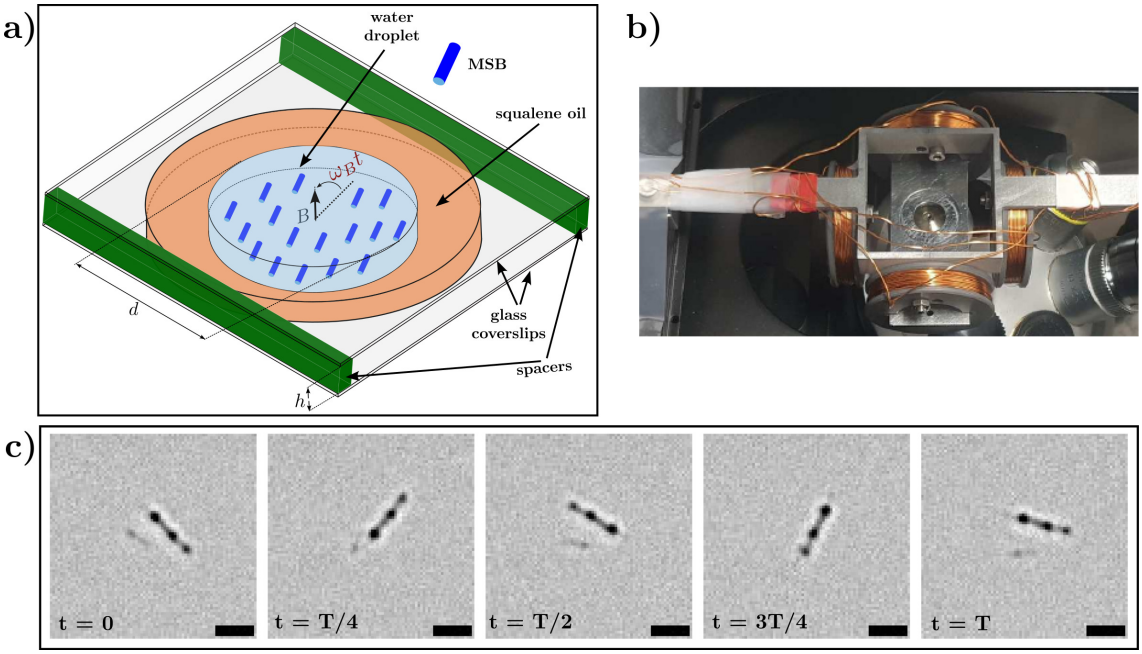

Figure 4.6.: MSB sample and stirring: **(a)** Schematic representation of the sample: an aqueous droplet of MSB surrounded by Squalene oil, sandwiched between two coverslips (sample thickness h = 287.5 μm, diameter d = 620 μm). Due to alternating magnetic field **B**, MSB undergoes synchronous rotation with angular frequency, ω_B. **(b)** Sample mounted in the inverted SD microscope, positioned in the center of the Helmholtz stirrer. **(c)** Representative snapshots of a single rotating MNB in an aqueous microdroplet when driving it with an alternating magnetic field (f =0.5 Hz). The scale bar is 10 μm and T represents the time period.

4.5.1. Sample preparation and stirring

To prepare the sample, first diluted 8 μL of MSBs suspension in 1.5 mL of water. Then, 0.4 μL of this suspension was pipetted into a 4 μL Squalene oil droplet sandwiched between two 15 mm diameter coverslips using a spacer in a custom-made aluminum holder (schematic of the sample given in Figure 4.6a). The spacer was made up of four layers of magic tape (thickness 50 μm each) and one double-sided tape (87.5 μm). For observation, this sample was mounted on the Helmholtz stirrer with the observation area centered on the intersection of these orthogonally arranged Helmholtz coils and placed on the inverted SD microscope (for an example, see Figure 4.6b). Transmission brightfield imaging of this droplet upon stirring was performed with 10x objective (HC PL S-APO, 10x/0.30 DRY) and Leica DFC360 FX camera. The MSBs were addressed with a rotational magnetic field using the EW controller in a frequency (f) range of 0 to 10 Hz with tunable magnetic field strength (here, 0.75 mT for rotational dynamics and 0.9 mT for magnetic behaviour). The magnetic field strengths used here were significantly below the coercive field of magnetite (20 mT) [211], i.e. the magnetization of MSB remained almost constant.

4.5.2. Rotational dynamics of MSB

We observed the expected rotation of the MSBs while addressing them with the Helmholtz stirrer and were also able to image this with the transmission brightfield microscopy (which was impossible with the previous stirrers). See Figure 4.6c, for representative images of MSB synchronous rotation at an addressed frequency of 0.5 Hz, where MSB appears as dark ellipsoidal region. As the stirring frequency increased, we noticed that the visible length of the rotating MSB started getting smaller, and it appeared like a rotating sphere at a higher frequency (see Figure 4.7a for an example). When we observed the MSB dynamics in detail, we realized that the MSB has a tilted rotation above a certain frequency.

For a quantitative analysis of the MSB dynamics, the MSB orientation with respect to the coordinate system was determined. As shown in the sketch (see Figure 4.7b), the optical axis was chosen in the z-direction, while the rotating magnetic field coincided with the imaging plane (xy-plane). From the recorded two-dimensional image time series of MSB rotation driven at different angular frequencies $\omega = 2\pi f$ with $f \in [0, 10]$, we extracted the projected length of the MSB perpendicular to the optical axis, $l_p = l_0 \sin\theta$, and angle φ in the xy-plane. The MATLAB code used for the data extraction was similar to the one used for the MSB length characterization (as discussed in section 4.3). As discussed before, the elliptical fitting of MSB was utilized to extract these parameters from the images.

As a result of the analysis, we found that the angular velocity of the MSB, $\omega_{MSB} = \Delta\varphi/\Delta t$ extracted from the image time series, perfectly coincides with the driving frequency of the magnetic stirrer, ω (see Figure 4.7c). As seen visually, the projected length of the MSB l_p matches the actual length l_0 only at low frequencies; however, a gradual decrease was observed for all MSBs examined,

starting at $\omega \approx 5\,rad/s$ (see Figure 4.7c). These results showed that the MSB started to tilt out of the imaging plane above a certain frequency and behaved as a flat rotor only in sufficiently low magnetic driving frequencies. This progressive tilting with stirring frequency emerges from balancing magnetic and friction-induced torques. A precession motion phase-locked to the magnetic field with a lower moment of inertia was observed for higher frequencies. This precession motion is also known as wobbling motion and is expected for both, ferrimagnetic and superparamagnetic rods [212, 213].

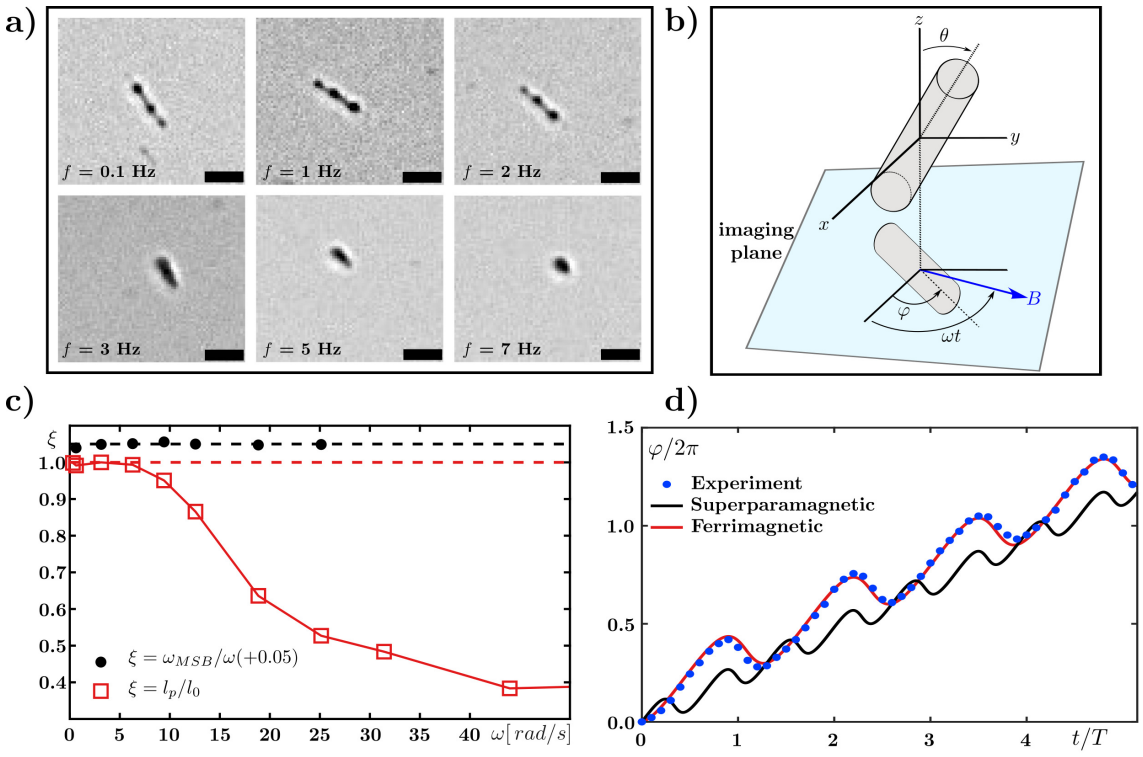

Figure 4.7.: MSB magnetic properties and projected length variation with stirring frequency: **(a)** MSB projected length (l_p, visible on optical imaging) varies with stirring frequency: it appears to have the same length at lower stirring frequencies (see f = 0.1 Hz and 1 Hz) and starts to reduce upon higher stirring frequencies (see f > 1 Hz). Scale bar is 10 μm. **(b)** Sketch of the coordinate system for evaluations: The magnetic field (B) rotates with an angular frequency ω in the xy-plane (the imaging plane), perpendicular to the optical axis (z-axis). Upon the MSB tilting, the apparent length projected on the imaging plane, $l_p = l_0 sin\theta$, where l_0 is the actual length, and θ is the angle made by the MSB to the z-axis. The MSBs angle to the x-axis is given as φ. **(c)** Evolution of projected length: For a representative MSB with l_0 =16.6 μm, its angular velocity (ω_{MSB}) followed well the drive frequency (ω) of the stirrer (black-filled circles), i.e., the ratio, $\xi = \omega_{MSB}/\omega$ was unity over a long range (this data was shifted up by 0.05 for better visibility). Due to the relatively short acquisition time of 54 ms, determining ω_{MSB} for $\omega > 25\,rad/s$ was difficult. On the contrary, the projected length, l_p was only agreed with l_0 for small driving frequencies (open red squares), i.e, the ratio, $\xi = l_p/l_o \approx 1$ only for $\omega < 5\,rad/s$. For higher frequencies, the MSB was titled concerning the xy-plane, reducing the projected length. An empirical fit $\xi = 0.75 + 0.25\cos(\omega/7.5)$ for $\omega > 4\,rad/s$ (red line) describes the data well. **(d)** Magnetic behaviour of MSB: The oscillation angle, $\varphi = \omega t - \beta$ of an occasionally hinged MSB (blue circles), driven with a frequency, $\omega = 3.14\,rad/s$, was well described by the dynamics of a ferrimagnetic rod (red line) compared to the dynamics of a superparamagnetic rod (black line).

4.5.3. Magnetic behaviour of MSB

The magnetic behaviour of Fe_3O_4 nanoparticles depended on their size and was widely estimated to be in a superparamagnetic regime around 20 nm [214] and have multi-domains above 50 nm [215]. We were interested in understanding the magnetic behaviour of the resulting MSB, as our purchased NPs were in the same range, and the manufacturer did not provide magnetic characterization. Therefore, we analyzed the wobbling motion of the MSBs to determine whether they behave ferrimagnetically or superparamagnetically.

To investigate the magnetic behaviour, we used those rods, one end of which was occasionally attached to the coverslip and performed a pinned rotation in response to the driving magnetic field. From the time series images of the MSB rotation, the center-of-mass region and the angle with respect to the imaging coordinate system ($\beta = \omega t - \varphi$) were retrieved using a MATLAB script (similar to the script discussed in the section 4.5.2). In the hinged MSB scenario, the evolution of the angle β has been predicted to be given by $d\beta/dt = \omega(1 - \gamma sin(a\beta))$ with $a = 1$ for ferrimagnetic rods [199] and $a = 2$ for superparamagnetic rods [216]. Here free parameter γ controls the gross slope of $\beta(t)$, on top of which the characteristic oscillations were superimposed.

As a representative, magnetic behaviour analyzed using a MSB with 8 μm length was shown in the Figure 4.7d. The one-end pinned MSB reached an asynchronous regime at a sufficiently high stirring frequency, $\omega = 3.14\,rad/s$. The angular evolution data obtained showed good overall agreement with the theoretical prediction at $\gamma = 0.64$ (see Figure 4.7d), but only the ferrimagnetic case (with $a = 1$) was able to capture the oscillations. The superparamagnetic oscillation showed significant deviation. From this experiments, we could conclude that the synthesized MSBs exhibit ferrimagnetic behaviour.

4.6. Quantifying the effect of MSBs agitation in droplet

After successfully characterizing the MSBs and developing microscope compatible stirrer, we were interested in studying the effect of stirring in microdroplets. In this regard, we explored the diffusional motion of fluorescent particles inside a microdroplet in the presence of MSBs. In this section, I will discuss the experimental procedures, SPT of fluorescent particles and findings from the statistical analysis of the data. The experiment discussed in this section was done together with Dr. Gires. I have carried out the SPT of the tracer beads and initial analysis. Dr. Gires and Prof. Weiss carried out the detailed analysis of the data. The Figures shown in the thesis were created by reanalyzing the data using MATLAB code from Prof. Weiss. The details discussed in this section have already been published in the journal, Physical Chemistry Chemical Physics [217].

4.6.1. Sample preparation for stirring

The sample prepared for studying diffusion in the agitating fluid was similar to section 4.5.1. Here 8 μL of MSBs suspension was mixed with 1.5 μL of Milli-Q water and 0.5 μL of 200 nm diameter fluorescent tracer beads (PBs; stock solution was prepared by diluting 1:10^4 in Milli-Q water and sonicated for 15 min). The observation sample was prepared by pipetting 0.4 μL of the solution in a 4 μL Squalene oil droplet on a 15 mm coverslip placed at the center slot of a custom-made aluminum holder. Then it was squeezed with another 15 mm coverslip using a custom spacer completes the observation sample. The spacer constitutes of four pieces of magic tape (50 μm thickness each) and one double-sided tape (87.5 μm thickness). A schematic of the resulting sample is given in Figure 4.8a. This sample was then aligned at the center of the Helmholtz stirrer and mounted on the SD microscope (see Figure 4.6b for an example) for observation. Here we used EW controller to drive the rotating magnetic field in the frequency (f) range of 0 to 10 Hz, with a magnetic field intensity of 0.5 mT.

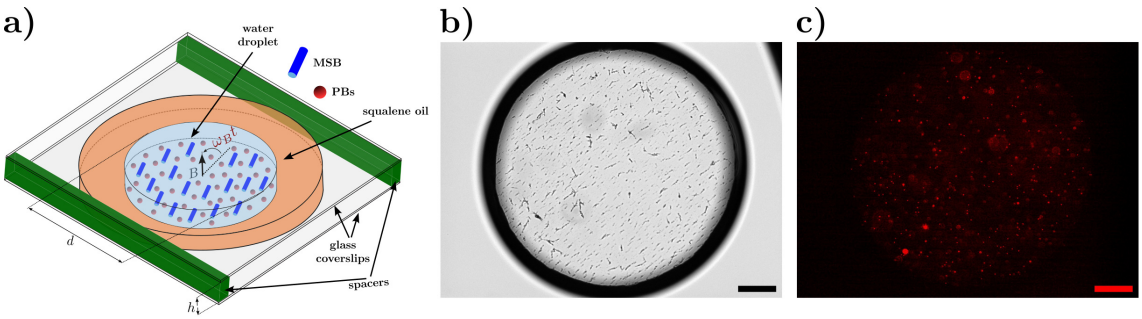

Figure 4.8.: Schematic and images of aqueous droplet containing MSBs and PBs: **(a)** Schematic representation of the sample: an aqueous droplet of MSBs and PBs surrounded by Squalene oil, sandwiched between two coverslips (sample thickness h = 287.5 μm, diameter d = 620 μm). Representative **(b)** transmission brightfield and **(c)** fluorescence images of the droplet taken at f = 0.01 Hz. In subfigure **(b)**, the dark circular ring denotes the droplet boundary, and dark connected pixels inside droplets are the MSBs. In subfigure **(c)**, the bright red pixels inside the droplets are the PBs. The scale bar of the subfigures **(b, c)** are 100 μm.

4.6.2. Imaging and SPT tracking

The droplet imaging was performed using the SD inverted microscope with 10x objective (HC PL S-APO 10x/0.30 DRY) and Leica DFC360 FX camera (1392 x 1040 pixels and pixel pitch of 645 nm). The MSBs were imaged with the transmission brightfield mode. The PBs imaging was performed in the fluorescence mode with 480 $\pm$ 20 nm illumination filter and 527 $\pm$ 15 nm detection. The frame rate (Δt) for the fluorescence imaging was 118 ms.

As a straightforward method, we relied on the SPT analysis of the PBs trajectories from the recorded time series images (see section 3.3.1.1 for detailed discussion of our tracking method) to study diffusional transport. The SPT algorithm allowed the detection of PBs fluorescence peak position with a subpixel resolution and position uncertainty around 80 nm. As finite and short

trajectories often cause problems to extract valuable information's [218], we had at least 246 trajectories for each frequency, with a minimum of N = 200 positions. From the recorded trajectories, a large variety of statistical measures can be analyzed to study diffusional transport (for a review, see [113]). Here I will be discussing mainly about the time/ensemble averaged MSD and velocity autocorrelation function, analyzed from the PBs trajectories in the presence and absence of stirring.

4.6.3. Results and discussion

To explore the local effect of controlled noise in droplets, we prepared aqueous microdroplets containing MSBs and fluorescent PBs. As discussed before, PBs motion captured with SPT was used to understand this effect. Bearing in mind with the potential application in biological fluids, the PBs radius was chosen to be around 100 nm (similar to many cell organelles). A schematic of prepared sample is given in Figure 4.8a. Upon addressing the droplets with rotating magnetic field, we observed the anticipated rotation of MSBs and diffusional motion of PBs. See supplementary movies in ref. [217] for an overview (a representative screenshot of transmission brightfield image of MSBs and fluorescent image of PBs are given in Figure 4.8 b and c respectively). A quantitative analysis of PBs diffusive motion in the presence and absence of MSBs stirring are discussed in the following sections.

4.6.3.1. MSD, anomaly exponents and generalized transport coefficients

As mentioned in section 2.3, MSD was used to quantify the effect of MSBs agitation in droplets. The same aqueous droplet with MSBs and PBs were used for the stirring experiments at different frequencies ($f \in [\,0, 10]$ Hz) to avoid the effect of any external factors. Time series images of PBs were recorded at a frame rate (Δt) of 118 ms and used for SPT analysis. From the trajectories obtained with atleast $N = 200$ positions, time-averaged MSD (TA-MSD) was calculated for all frequencies with a lag time, $\tau = k\Delta t$, using the following equation,

$$\langle r^2(\tau)\rangle_t = \frac{1}{N-k}\sum_{i=1}^{N-k}\left[\,r((i+k)\Delta t) - r(i\Delta t)\right]^2. \tag{4.1}$$

In addition to individual TA-MSDs, an ensemble average of all TA-MSDs, $\langle r^2(\tau)\rangle_{t,E}$ at each stirring frequencies (f) were also calculated.

As discussed in section 2.3.1, the MSD related to the anomaly exponent (α) and generalized transport coefficient (K) with the following relation,

$$\langle r^2(\tau)\rangle = K\tau^{\alpha} \tag{4.2}$$

The $\langle r^2(\tau)\rangle$ here is either $\langle r^2(\tau)\rangle_t$ and $\langle r^2(\tau)\rangle_{t,E}$ since this relation is expected for both cases. This Equation 4.2 can capture the features of the anomalous diffusion (subdiffusion with $\alpha < 1$ and superdiffusion with $\alpha > 1$) as well as Brownian diffusion ($\alpha = 1$).

Fitting all the individual TA-MSDs using Equation 4.2 with linear regression of $\log(\langle r^2(\tau)\rangle_t)$ $vs.$ $\log(\tau)$ yielded the probability density functions (PDFs) of anomaly exponent, $p(\alpha)$, and generalized transport coefficients, $p(K)$. The fitting process relies on finite averages at every lag time, so the fitting process was restricted to $\tau < 10\Delta t$. Insufficient averaging due to statistical fluctuations can spoil the fitting at higher lag times. The mean of PDFs of the anomaly exponents and generalized transport coefficients of TA-MSDs will be denoted hereafter as $\langle\alpha\rangle$ and $\langle K\rangle$, respectively. Due to the fitting restriction, PDFs and their mean encoded information on short-time scales. The ensemble-averaged TA-MSD, $\langle r^2(\tau)\rangle_{t,E}$ (EA-TA-MSDs) were also analyzed using the same Equation 4.2. Since ensemble averaging smoothen out the fluctuations in individual TA-MSDs, all lag times were included in the fitting process. The resulting parameters, α_e and K_e encoded characteristics of all available time scales.

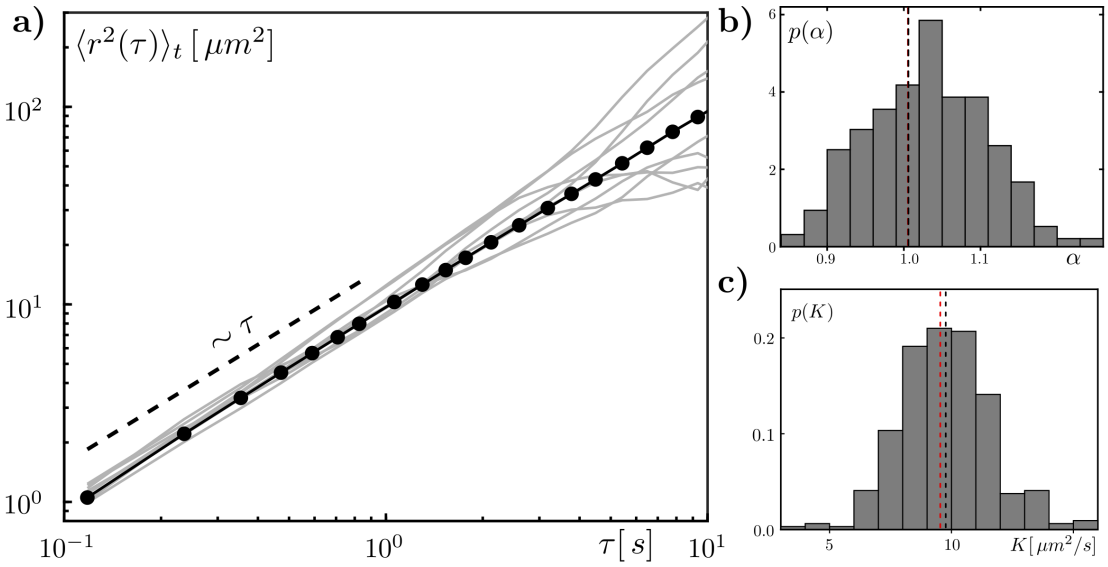

Figure 4.9.: The MSD, anomaly exponent and generalized transport coefficient in the absence of stirring: (a) Representative individual TA-MSDs, $\langle r^2(\tau)\rangle_t$ (grey lines), and the ensemble average of all TA-MSDs, $\langle r^2(\tau)\rangle_{t,E}$ (black line with circles), of the diffusing PBs in the absence of stirring ($f = 0$ Hz) are shown in logarithmic scaling. The fitting of the MSD (see black dashed line) shows anticipated normal diffusion ($\alpha \approx 1$). **(b)** The PDF of anomaly exponents, $p(\alpha)$, extracted by fitting all individual TA-MSDs, is peaked around $\alpha = 1$ with a mean value of 1.03 ± 0.08 (black dashed vertical line). The value ($\alpha_e = 1.01$) obtained by fitting the ensemble-averaged TA-MSD is denoted by the vertical red dashed line. **(c)** The PDF of the generalized diffusion coefficients, $p(K)$, from all the individual TA-MSDs, is peaked around $10\,\mu m^2/s$ with the mean value denoted by the vertical black dashed line. The K_e obtained by fitting ensemble averaged TA-MSD is marked with the vertical red dashed line. Since $\alpha \approx 1$, the K is expressed in the unit of normal diffusion constant, $\mu m^2/s$.

The diffusion behaviour of PBs without MSBs stirring

For the evaluation of stirring effects in the diffusional motion, initially, PBs trajectories in the absence of stirring were analyzed as a control. All the TA-MSDs curves followed the anticipated

linear scaling, evident from the double logarithmic plot in Figure 4.9a. Due to the finite time series length, all the TA-MSDs exhibited fluctuation around the mean. This fluctuation was also captured in the PDF of the anomaly exponent, $p(\alpha)$ (Figure 4.9b). The mean value of the PDF of $p(\alpha)$ ($\langle\alpha\rangle = 1.03$, black vertical dashed line in Figure 4.9b) was approximately equal to one, as expected in normal diffusion. Similarly, the anomaly exponent (α_e), obtained by fitting the associated EA-TA-MSDs, was also close to unity (1.02, red vertical dashed line in Figure 4.9b). As a side note, minor deviations from unity are frequently observed in SPT experiments [159, 219].

The fitting of the TA-MSDs, PDF $p(K)$ (Figure 4.9c) of the generalized diffusion coefficient, was obtained with a mean value $K = 9.78\,\mu m^2/s$ (black dashed line in Figure 4.9c). Similarly, fitting EA-TA-MSD, K_e of $9.54\,\mu m^2/s$ (red dashed line in Figure 4.9c), was obtained. These experimentally determined values were closer to the theoretical prediction, $K_\alpha = 4D_0 = 9.2\,\mu m^2/s$. Here, $D_0 = K_B T_0/(6\pi\eta R) \approx 2.3\,\mu m^2/s$ is the theorectically predicted diffusion coefficient for 100 nm beads in water using Einstein-Stokes equation (see section 2.3). As uncertainties in the precise value of K was observed in several experimental methods [159] and our experimental values were in the expected range, we concluded that the PBs were undergoing normal diffusion without stirring.

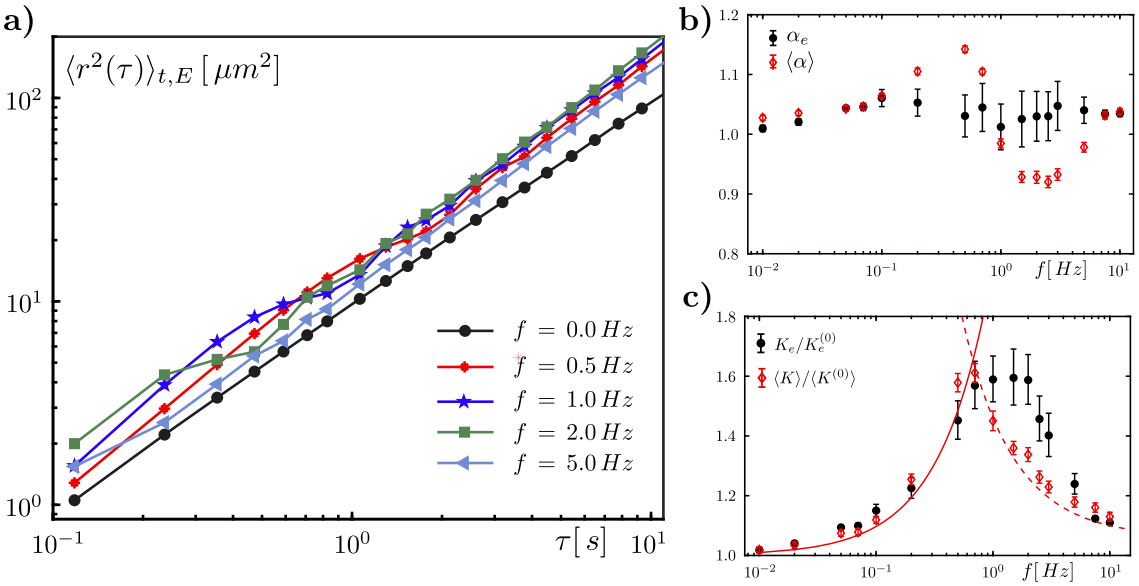

Figure 4.10.: The MSD, anomaly exponent and generalized transport coefficient at different stirring frequencies: **(a)** Representative ensemble averaged TA-MSDs at the indicated stirring frequencies in the logarithmic scale show roughly normal behaviour. But the anomaly exponent, generalized diffusion coefficient, and bumpy features in the MSD vary with the stirring frequencies (f). **(b)** The anomaly exponents from the ensemble averaged TA-MSD, α_e (black circles) shows only minor deviations from unity for all the frequencies. However, the mean value from the PDF of all TA-MSDs ($\langle\alpha\rangle$, red open diamonds) shows significant deviations above 0.5 Hz. The excursion related to the bumps in the MSD. **(c)** The normalized generalized transport coefficients for the ensemble-averaged TA-MSD (K_e, black circles) and the mean of the PDF, $p(K)$ from all individual TA-MSDs ($\langle K\rangle$, red open diamonds) show a significant increase at intermediate stirring frequencies compared to their respective values in the absence of stirring (denoted by a superscript "(0)"). The fit $y = 1 + f$ well represents the linear growth up to $0.5\,Hz$ with $y = \langle K\rangle/\langle K^{(0)}\rangle$ and $\langle K^{(0)}\rangle$ denoting the value at $f = 0$ Hz (red line). The power law decrease for frequencies $f > 0.6$ Hz due to MSBs tilting can be represented by the fit, $y = 1 + 0.5/f$. The error bars are the standard deviation for $\langle\alpha\rangle$ and $\langle K\rangle$, and 95% confidence bound of the fitting parameter for α_e and K_e.

The influence of MSBs stirring on the diffusion of PBs

As the unstirred PBs showed the predicted normal diffusion, we expected to observe superdiffusive or ballistic signatures in the presence of stirring ($f > 0\,Hz$). Observing the rotation of MSBs enforced this idea, and we analyzed the PBs trajectories using the same methods. However, EA-TA-MSDs (see Figure 4.10a) obtained with stirring remained to have a linear scaling, instead of having superdiffusive signatures. The EA-TA-MSDs had elevated K_e with bumpy signatures. The bumpy signature seemed to carry the stirring information (see bumps at 0.5 Hz, 1 Hz, and 2 Hz for reference). Also, a non-monotonous dependence of K_e to stirring frequency was visible in the curves.

To understand these features in detail, we calculated the mean anomaly exponents ($\langle\alpha\rangle$ and α_e) and generalized transport coefficients ($\langle K\rangle$ and K_e) at each stirring frequency (f). The $\langle\alpha\rangle$ and $\langle K\rangle$ were obtained from the PDFs $p(\alpha)$ and $p(K)$ from the TA-MSDs. Fitting the EA-TA-MSD yielded the α_e and K_e. The α_e remained closer to unity for all the probed stirring frequencies (see Figure 4.10b). In contrast, $\langle\alpha\rangle$ showed significant excursion at intermediate values of f and was connected to the visible bumps in the MSD (see Figure 4.10a). The visible bump position (τ_b) in the MSDs was observed to migrate towards lower time lags as $\tau_b \sim 1/f$ for increasing f.

The generalised transport coefficients (both $\langle K\rangle$ and K_e) showed a significant increase at intermediate values of f, which eventually subsided for large f (see Figure 4.10c). Thus, despite synchronous stirring with MSBs, the apparent mode of motion remained normally diffusive with an increased diffusion coefficient for intermediate stirring frequencies. According to the Einstein-Stokes theorem, the stirring introduced an active noise with energy in the order of K_BT to the PBs motion.

The underlying reason behind the non-monotonous behavior of K is connected to the tilting of MSBs discussed in section 4.5. An approximate prediction of K variation with f can be obtained via Peclet number (P), considering the measured values of K are proportional to P.

$$P = \frac{l_p^2}{TD_0} \sim \frac{fl_p^2}{D_0} \tag{4.3}$$

Here l_p is the projected length of the MSBs, D_0 is the constant thermal diffusion coefficient of the PBs and $f = 1/T$.

Since l_p is constant for low stirring frequencies, P increases with f ($K \sim P \sim f$) for $f \leq 0.5$ Hz, which agrees with the experimental data (see Figure 4.10c). At higher stirring frequencies, the tilting of the MSBs leads to reduced l_p. By approximating $l_p \sim f$ for $f > 0.5$ Hz, yielding $K \sim P \sim 1/f$, which agrees with the experimental results (see Figure 4.10c).

To further explore the signature of stirring in the apparent normal diffusion of PBs, we investigated the velocity autocorrelation function of the trajectories, which is discussed in the following section.

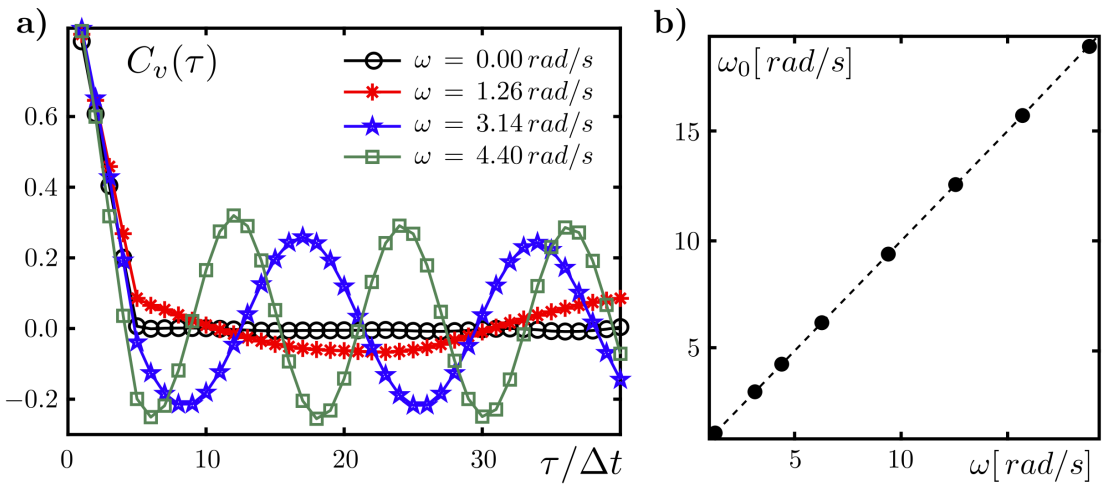

Figure 4.11.: The VACF at different stirring frequencies: **(a)** Representative VACF curves, without stirring (black circles) and with the indicated stirring frequencies (red asterisks, blue pentagons and green squares), calculated for $\delta t = 5\Delta t$. Without stirring, no correlations were observed for $\tau > 5\Delta t$, indicating a memoryless random walk. On the other hand, oscillatory correlations were observed while stirring. **(b)** The oscillation frequency (ω_0) extracted from the VACF corresponded nicely with the stirring frequencies (ω) in the range $1\,rad/s \leq \omega \leq 20\,rad/s$.

4.6.3.2. The velocity autocorrelation function

The MSD analysis reported almost normal diffusion even in the presence of stirring. We have explored other observables to identify the signatures of additional noise introduced by stirring. Since the velocity autocorrelation function was reported to have sensitivity towards altered random walk (see section 2.3.2), we studied the normalized, ensemble- and time- averaged velocity autocorrelation function (VACF),

$$C_v(\tau) = \frac{\langle v(t)v(t+\tau)\rangle_{t,E}}{\langle v(t)^2\rangle_{t,E}} \tag{4.4}$$

Here $v(t) = [r(t+\delta t) - r(t)]/\delta t$ is the instantaneous velocity of the PBs at time t, calculated using the distance travelled in the period δt. Also note that the frequency (f) discussed in this section is given in terms of the angular frequency ω, where $\omega = 2\pi f$.

Without stirring ($\omega = 0$), as expected, the VACF function decreases from one to zero for $\tau \leq \delta t$ and disappears for $\tau > \delta t$ (see Figure 4.11a, black circles), a typical signature of a normal random walk without memory [113]. However, the function showed oscillatory correlations upon stirring ($\omega > 0$). See Figure 4.11a with red, blue, and green symbols for an overview of oscillatory correlations at the indicated frequencies. In addition, looking at the VACF of individual trajectories shows random fluctuations rather than a deterministic periodic back-and-forth motion (more information see ref. [217]). The oscillation frequency (ω_0) retrieved from the VACF was in good agreement with the stirring frequency (ω) in the range of $1\,rad/s \leq \omega \leq 20\,rad/s$ (see Figure

4.11b). Thus, from the analysis, we can conclude that the VACF can capture the signatures of the almost normal diffusion of PBs with an increased transport coefficient upon stirring.

4.6.4. Conclusion

We understood from the above analysis that MSD and VACF captured the signatures of stirring from the PBs trajectories. Instead of observing a superdiffusive behaviour upon stirring, an apparent normal diffusion with an enhanced transport coefficient was observed. The transport coefficient has a non-monotonous behaviour upon stirring due to the tilting of MSBs at higher frequencies. Complementary to these analyses, as discussed in the ref. [217], the power spectral density of the individual trajectories also captured the stirring frequencies. The ergodicity breaking parameter also showed that intermediate stirring frequencies induce higher spreading of the TA-MSDs corresponding to their respective ensemble averages [217]. Summing up, an effect of stirring in the diffusion of PBs was found. However, the tilting of MSBs due to the low magnetic field strength of the stirrer and the bad temporal resolution masked many of the features. With the current system, we were only able to observe normal diffusion with a maximum two-fold enhanced diffusion coefficient. The stirring signatures of stirring can be better identified with an improved temporal resolution. Decorrelating the stirrers with a higher magnetic field can further enhance the stirring.

4.7. Stirring experiments with biofluids

After the successful synthesis of MSBs and observing its stirring action in biomimetic fluids, we were interested in analyzing the compatibility of MSBs in biofluid systems. The biofluid system used here was *Xenopus* extract. For this purpose, the MSBs were incorporated in the extract and produced droplets. I will be discussing about the incorporation method of MSBs inside CSF extract, production of microdroplets using T-junction device and pipetting method, deduction of stirring action of MSBs using microtubules movements etc., in this section. The experiments discussed here were done together with Dr. Gires and the figures shown here were produced by reanalyzing the data using Dr. Gires MATLAB code. Some part of this section was already published in Nature Scientific Reports [200].

4.7.1. Encapsulation of MSBs in microdroplets using microfluidics chip and stirring

We utilized a T-junction device to check the feasibility of MSBs encapsulation in droplets using microfluidics devices. The T-junction device used here was Aquapel treated and the encapsulation procedure was similar to the one discussed in section 3.2.5. The Squalene oil with Cithrol DPHS surfactant acted as continuous phase (or carrier fluid) and MSBs containing CSF extract was the discontinuous phase. The MSBs containing CSF extract was prepared in the following way: 10 μL

of the MSB solution was centrifuged at 10,000 g for 10 min and carefully removed the supernatant. The remaining pellet was resuspended in 10 μL of CSF extract and mixed by gentle flickering and inverting the Eppendorf tube. Deep-frozen CSF extract (prepared as discussed in section 3.1) stored at -80°C was used for the feasibility test.

As discussed in section 3.2.5, the CSF extract containing MSBs was first injected into the PTFE tubing at 50 μL/h speed. The microdroplets were produced in the T-junction device by keeping the flow rates of both carrier fluid and discontinuous phase at 50 μL/h. We observed a successful production of CSF extract microdroplets containing MSBs inside the chip (see Figure 4.12a as an example). As clearly visible, the MSBs remained dispersed inside the extract droplet and did not dispersed into the carrier fluid.

During the production of microdroplets, the encapsulated MSBs were addressed with an external rotating magnetic field. To this end, the T-junction device was kept inside the Helmholtz stirrer and an Ardruino controller was used to produce a magnetic field with an intensity of 1.9 mT. The stirring action was observed using the Zeiss Axiovert 25 inverted microscope with 10x objective. Up on addressing with a frequency of 0.1 Hz, we observed the anticipated rotation of MSBs. From this observation, it was concluded that, the MSBs were compatible with microfluidics and can exert stirring motions in complex biofluid microdroplets.

4.7.2. Production of labelled microtubules inside CSF extract

The microtubules were produced in the CSF extract using the previously reported methods [12]. A deep-frozen CSF extract (prepared as discussed in section 3.1) stored at -80°C was used for the microtubule preparation. 1 μL of 1 mM GTP containing GT buffer and 9 μL thawed CSF extract was added to 20 μg of tetramethylrhodamine tubulin (Cat. # TL331M, Cytoskeleton Inc.), to prepare the diluted Rhodamine tubulin. 3 μL of diluted Rhodamine tubulin was added to 25 μL of thawed CSF extract in a 1.5 mL Eppendorf tube. This was mixed by pipetting and inverting the Eppendorf tube. Resting this extract in room temperature produced the labelled microtubules.

4.7.3. Effect of MSBs stirring on extract with labelled microtubules

The experiments conducted to evaluate the effect of active noise induced by MSBs in microtubule labelled extract will be discussed in this section. Polydisperse droplets were prepared using the pipetting method and the microtubule motion was analyzed using the average Pearson correlation coefficient for this purpose. Details to this end are discussed below.

4.7.3.1. Sample preparation, imaging and stirring

The polydisperse droplets were prepared by the pipetting method discussed in Good et al. [135]. For this purpose, 10 μL of the MSBs suspension was centrifuged at 10,000 g for 10 min and

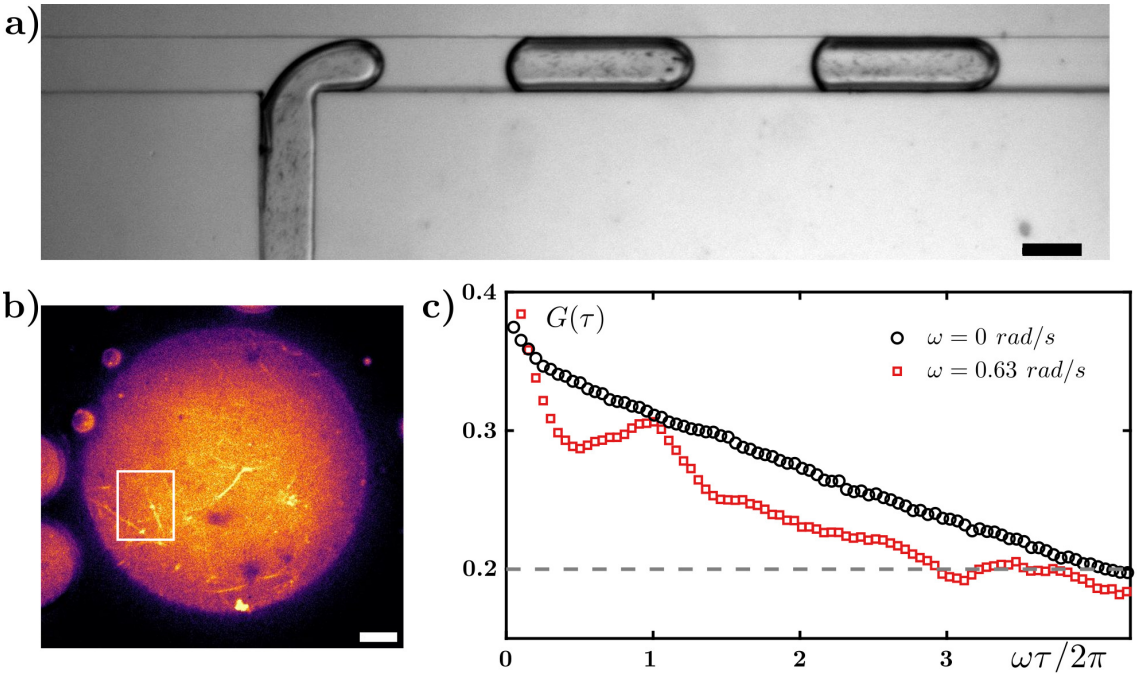

Figure 4.12.: Stirring *Xenopus* extract droplet: **(a)** Production of CSF extract microdroplets containing MSBs (seen as tiny dark rods) using a T-junction microfluidic device. Squalene oil with Cithrol DPHS is the continuous phase and CSF extract with MSBs is the discontinuous phase. The scale bar is 150 μm. **(b)** A representative microdroplet containing microtubules (bright yellow pixels) and MSBs (dark pixels inside the droplet). This rectangular region of interest (inside the white rectangle) was used for calculating $G(\tau)$, discussed in subfigure **(c)**. Scale bar is 10 μm. **(c)** The average Pearson coefficient $G(\tau)$ of microtubules shows a monotonous decay in the absence of stirring. Upon active stirring with MSBs, $G(\tau)$ shows a fast decay with some oscillatory features which reflect the action of nearby MSBs.

removed the supernatant. The resulting pellet was resuspended in 10 μL of Rhodamine labelled tubulin containing CSF extract (prepared as mention in section 4.7.2) by pipetting (using a cutted tip) and inverting the Eppendorf tube. The polydisperse droplet produced by pipetting 5 μL of this MSB containing Rhodamine labelled CSF extract suspension in 20 μL of Squalene oil with Cithrol DPHS surfactant, inside a 1.5 mL Eppendorf tube. The shear force created by keeping the pipette tip (P20) pressed against the bottom of the Eppendorf tube during pipetting the suspension (5-10 times) resulted in the polydisperse droplets formation.

The observation sample was prepared by transferring 10 μL of the sedimented droplets in a cylindrical chamber made up of SecureSeal™ double side adhesive tape spacer (9 mm diameter and 120 μm thickness) on a glass slide and immediately covered with a coverslip. The sample was placed at the center of the Helmholtz coil and mounted on the inverted SD microscope. Confocal fluorescence imaging was performed with 63x oil immersion objective (HCX PL APO 63x/1.4) using 561 nm excitation laser (Coherent sapphire) and a 575 – 625 nm detection filter. Images were taken with an EM-CCD camera (Roper Evolve 512, 512 x 512 pixel, 0.2 μm per pixel, set to 16-bit mode) connected to the spinning disc unit (Yokogawa, CSU X1) at a frame rate of 503 ms.

4.7.3.2. Results and discussion

The successful encapsulation of MSBs and the formation of microtubules were evident from the fluorescence images. For example, see Figure 4.12b, where microtubules are the bright yellow pixels and MSBs as the dark pixels. Active motion of microtubules was observed in the droplets, even in the absence of external stirring, due to its internal energy-driven dynamics. Adding external noise by operating the MSBs (using f = 0.1 Hz) showed marked deviation to its undulations (for an example, see supplementary movies 4 and 5 in ref. [200]). The MSBs were not performing a stirring motion but rather had a tumbling motion. This behaviour was due to the presence of a dense microtubule network and other internal macromolecules inside the viscous extract droplet. A less deterministic motion is also beneficial for introducing active noise to the biofluid system.

The correlation coefficient ($G(\tau)$) of the image series was calculated on a microdroplet to quantify the effects of stirring. In order to avoid direct signatures from the MSBs motion, a region of interest with n_p pixels was selected inside the microdroplet that contain only microtubules and void of nearby MSBs (see the region inside the white square in Figure 4.12b). The $G(\tau)$ was calculated from this new cropped image time series $I(t)$ for a time lag $\tau = t_2 - t_1$, using the following equation.

$$G(\tau) = \left\langle \frac{(I(t_1) - \langle I(t_1)\rangle)(I(t_2) - \langle I(t_2)\rangle)}{n_p\sqrt{\sigma^2(I(t_1))\sigma^2(I(t_2))}} \right\rangle_{t_1} \tag{4.5}$$

Here $\sigma^2(I(t))$ is the variance of all the pixel fluorescence values at a given time, t.

The $G(\tau)$ shows a monotonous and featureless decay curve in the absence of stirring (see Figure 4.12c). The stirring induced a rapid decay of the $G(\tau)$, indicating the noise introduced by the MSBs disturbed the correlated motion of microtubules inside the microdroplet. The decay curve also had an oscillatory behaviour and a peak corresponding to the stirring frequency. This indicated that the tumbling action of the nearby MSBs shook the microtubules. The findings from the experiments suggested that MSBs are good candidates for introducing externally controlled noise in biologically active fluids and artificial fluids.

4.8. Summary of the chapter

This chapter summarizes the successful synthesis of MSBs to their application in biological fluids. As discussed, MSBs were synthesized using the Stöber method and successfully characterized. Microscope compactible stirring devices and controllers for addressing the MSBs were also successfully fabricated. The feasibility of the MSBs agitation was analyzed using the SPT of PBs inside a droplet. Even though the tilting of the MSBs at higher frequencies was an issue, we were able to introduce a two-fold enhancement in the diffusion coefficient upon stirring. Finally, we understood that MSBs could be encapsulated in biological fluid and introduce active noise inside

the system. With further improvements, MSBs can be used as versatile tool to enhance mixing in biomimetic or artificial fluids.

5

Structure and pattern formation in biofluids

This chapter focuses on experiments to identify the effect of confinement and chemical perturbation on the structure and pattern formation in Xenopus extract. The first section discusses the protocol developed for obtaining mitotic spindle and aster in cell-like droplets. The second section deals with the cell-like pattern formation using interphase extract. This section discusses the effect of taxol on pattern formation and quantifies its effect over time using the parameters obtained through Voronoi tesselation. The effect of chamber geometry on pattern formation is also analyzed here. The final section deals with the protocol developed to obtain cell-like division using cycling extracts. The preliminary observation on the effect of chamber geometry on the cell-like division is also discussed here. Please note that references to figures in the Appendix section are indicated by a prefix 'A'.

5.1. Assembly of mitotic spindle and aster in *Xenopus laevis* extracts

The *Xenopus* egg was arrested in the metaphase state of meiosis II prior to fertilization by the action of cytostatic factor (CSF) [220]. The cytoplasmic extract prepared from the egg has been extensively used in the literature to study cell cycle in vitro [55]. Here we used the CSF extract to study asters and the mitotic spindles. Four ways (see section 2.2) are discussed in the literature to prepare the mitotic spindle with this CSF extract: CSF spindle, cycled spindle, chromatin coated bead spindle, and Ran spindle [86, 87, 90]. Researchers used this in vitro system to expand their knowledge of mitotic spindle formation. A lot of works looked into the proteins and mechanisms involved in the spindle formation [55, 93, 94, 96, 97]. Some intriguing works addressed the factors affecting the scaling of mitotic spindles with respect to their cell boundaries [12, 13, 221]. They found that the spindle length scales with the droplet volume up to a certain limit and then becomes constant. This scaling mechanism was predicted with a limiting component model, and it was also reported that the coupling weakens at higher volumes. It was intriguing to investigate how this scaling will

alter in the presence of MSBs agitation. Due to our interest in this fascinating system, we looked at mitotic spindle formation in droplets intending to study the effect of mechanical perturbation on mitotic spindle size. With this in mind, we first learned to make mitotic spindle assembly reactions using the cycled spindle method and checked these spindles formation in fixed samples. Later we encapsulated this spindle assembly reaction in oil droplets using T-junction microfluidic devices and studied the formation of mitotic spindle/aster in droplets. The following section describes this project, which was carried out jointly with Dr. Gires.

5.1.1. In vitro mitotic spindle assembly

The spindle assembly reaction with CSF extract was adapted from the works of Hazel et al. [13] and Good et al. [12, 135]. We also benefitted from the experience of Prof. Stemmann's lab (Genetics, University of Bayreuth). The first step in this experiment was to determine the quality of the CSF extract, as it was critical for a successful mitotic spindle reaction. If the eggs and their extract were visually looking good, the below-mentioned quality test was performed before using it for mitotic spindle assay.

5.1.1.1. Quality check of the CSF extract

We determined the quality of the extract by examining the nuclear structure of the sperm head added to the CSF extract in the presence and absence of Ca^{2+} (used the 25x Ca^{2+}, see Appendix A.1 for details). The addition of Ca^{2+} mimics fertilization and induces interphase entry of the extract. The sperm head decondensed to a spherical shape with a nuclear envelope at the interphase stage [23]. However, in the current CSF arrest state, it retains the condensed snake-like shape (precisely, a corkscrew shape [222]). The quality control experiment was performed as follows;

Two Eppendorf tubes were used to perform the quality experiment, one for Ca^{2+} presence (Eppi A) and one for Ca^{2+} absence (Eppi B). In both Eppendorf tubes, 20 μL of extract and 1 μL of sperm heads (stock solution contains 14,470 sperm heads per μL) were added. Also, 1 μL Ca^{2+} was added to Eppi A to induce interphase entry. The reaction mixture in the Eppendorf tubes were gently mixed using a pipette with a cut-off pipette tip and kept at room temperature for 30 min. Observation samples were prepared from these Eppendorf tubes to observe the shape of the sperm head.

The observation sample was prepared on a microscope slide by adding 3 μL of Spindle-Fix to 1 μL of the reaction mixture and immediately covered it with a coverslip. The DAPI enabled us to observe the sperm nuclei under fluorescent imaging. In a good quality extract, the following will be observed: (i) the sperm head will retain its snake-like shape without Ca^{2+}, and (ii) spherical nuclei will be visible for extract cycled with Ca^{2+}. The extracts that cannot show these features are considered of bad quality. Our experiments were conducted using good-quality extracts.

5.1.1.2. Mitotic spindle assembly reaction

The mitotic spindle reactions with *Xenopus laevis* using cycled spindle method required 50 μL CSF extract, 2 μL of *Xenopus laevis* sperm heads at a final concentration around 500 per μL, 3 μL of rhodamine-labelled porcine brain tubulin solution (Rhod-tubulin), and 1 μL DAPI/Hoechst dye (10 mg/mL stock solution, Sigma Aldrich). Metaphase arrested spindle was visualized by incorporating Rhodamine tubulin and DAPI/Hoechst. DAPI/Hoechst labels the DNA and Rhodamine tubulin for the microtubules. Rhod-tubulin was prepared by mixing 1 μL of 1 mM GTP GT buffer and 9 μL of fresh CSF extract in 20 μg of tetramethylrhodamine tubulin (Cat. # TL331M, Cytoskeleton Inc.).

The 1.5 mL Eppendorf tubes were used for the spindle assembly reaction as it allows proper gas exchange. In an Eppendorf tube, 25 μL fresh CSF extract, 1 μL demembranated sperm heads, 1.5 μL Rhod-tubulin, and 0.5 μL DAPI/Hoechst were added and mixed gently with a cut-off pipette tip. This was then incubated for 10 min at 22°C. Progression of the extract through interphase was induced by adding 1 μL Ca^{2+} and incubating at 22°C for 80-90 min. An equal volume (25 μL) of fresh CSF extract (containing 1.5 μL Rhod-tubulin and 0.5 μL DAPI/Hoechst) was added to induce the mitotic spindle formation and metaphase arrest. Samples were taken at regular intervals to check the mitotic spindle formation.

5.1.1.3. Sample preparation and imaging

Samples were prepared by squashing the spindle assembly reaction with Spindle-Fix between a microscope slide and a coverslip. In detail, 1 μL of the spindle assembly reaction was pipetted onto a microscope slide, and 3 μL of Spindle-Fix was placed on top. A coverslip was then placed slowly on top, avoiding air bubbles. We sealed the coverslip with nail polish and stowed it at 4°C for long-term storage.

Fluorescence imaging of the mitotic spindle was performed with SP5 confocal laser scanning microscope. Rhodamine tubulin was imaged using an excitation wavelength of 561 nm and a detection range of 575-650 nm. DAPI and Hoechst used an excitation wavelength of 405 nm and a 420-500 nm detection range. Images were acquired with mono-directional scanning (scanning frequency ranges 400-1400 Hz, depending on zoom factor), using a HCPL APO 100x/1.40 OIL or a HCXPL APO 63x/1.4 OIL CS2 objective at room temperature.

5.1.1.4. Result and discussion

Fixed samples were prepared at 15 min intervals to observe the formation of bipolar mitotic spindles. The bipolar mitotic spindles were observed within 60 min on these samples, and the success depended entirely on the extract quality. The mitotic spindle formed has the typical fusiform structure with microtubules emanating from both poles and the chromosomes arranged at the equator

using these microtubules. Representative images of the mitotic spindles observed are given in the Figure 5.1a and b, where red is the microtubules and blue is the chromosome (the colour-coded images were created with FIJI). Sometimes, unusual structures, such as multiple mitotic spindles sharing a common pole, were also observed in the fixed samples (see Figure 5.1c for a representative image with two mitotic spindles sharing a common pole). Other than the bipolar spindles, aster-like structures and other random microtubule structures were also observed in the samples. The bipolar spindle formed with a well-aligned chromosome in the equatorial plane was reminiscent of the mitotic spindles observed in somatic cells. The chromosome arrangement in the metaphase plate significantly varies with extracts. The chromosomes in a good extract were tightly focused at the equator, whereas the chromosomes in a less robust extract were both in the equator and scattered around either side of the extract. The most frequently observed mitotic spindle length in these fixed samples was $\sim$20 μm, which was in range with the previous realizations [223].

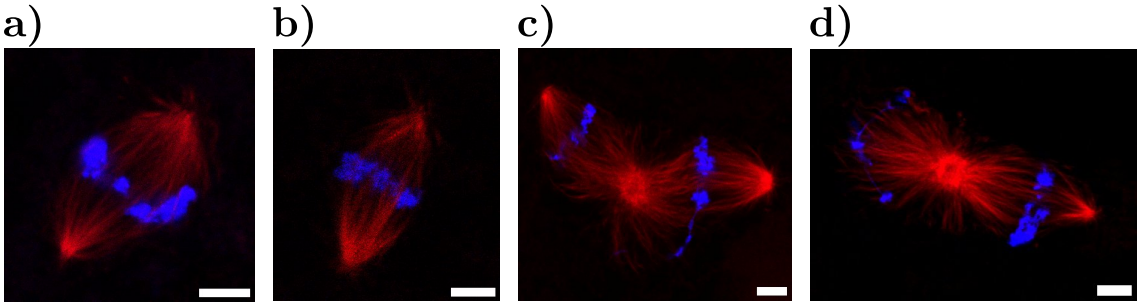

Figure 5.1.: Representative images of mitotic spindles in the bulk sample: **(a)** and **(b)** are the normal mitotic spindles. **(c)** Two bipolar mitotic spindles share a common pole. **(d)** A bipolar mitotic spindle and a half spindle share a common pole. Here red represents the microtubules and blue is the chromosome. The scale bar for all images are 5 μm.

There were some stages in the project where we could not obtain the mitotic spindles. In order to improve the yield of mitotic spindles, the extract was supplemented with protease inhibitors, ATP regeneration energy mix and cytochalasin D (instead of cytochalasin B). The extract with these additives produced mitotic spindles, whereas the control experiments without them also resulted in the same. Even though these additives have some influence on mitotic spindle formation, the main factor is the inherent extract quality. The stressed state of the frog and the extract preparation protocols has a significant impact on the result. After several successful realizations, we became confident using the mitotic spindle formation assay to create droplets. The following section will go over the experiments that were carried out with these mitotic spindle assay droplets.

5.1.2. Mitotic spindle in droplets

After clearly establishing the mitotic spindle assay protocol and having the idea of perturbing the mitotic spindle formation in a confined environment, mitotic spindle reaction containing droplets were produced. As inspired from the studies of Good et al. [12] and Hazel et al. [13] about controlling the spindle length by volume and shape modulation of extract droplets, we prepared extract

droplets in Squalene oil with the idea of perturbing the spindle assembly using MSBs agitation. The following section will discuss our experiments and findings with the extract droplets.

5.1.2.1. Sample preparation and imaging

The preparation of the spindle assembly reaction was discussed in section 5.1.1.2. The concentration of 500 sperm heads/μL was used in the bulk experiments and there was a risk of spindle fusion at higher concentrations [135]. However, a higher concentration of sperm heads was necessary to obtain at least one sperm head in the encapsulated droplets. The sperm head concentration also needed to be adjusted depending on the size of the droplets [135]. Here we used 1000 sperm heads/μL in our droplet experiments. The concentration of other materials and steps remained the same as in section 5.1.1.2. In the experiments to investigate the effects of MSBs agitation on mitotic spindle formation, MSBs were also added to the CSF extract. For this purpose, 10 μL of MSBs were centrifuged at 10,000 g for 10 min and the pellet obtained was added to the extract. The MSBs were mixed by careful pipetting with a cut-off pipette tip and inverting the Eppendorf tube.

The extract, which was cycled back to the mitotic state, was immediately used for droplet production. We used two approaches to produce the droplets containing spindle assembly reaction: (i) the microfluidic method and (ii) pipetting method (both methods are previously discussed in sections 4.7.1 and 4.7.3.1, respectively).

Microfluidic method: Monodisperse droplets were produced by this method. For this purpose, 30-50 μL of the prepared spindle assembly reaction was immediately inserted into the PTFE tubing of the dispersed phase syringe prefilled with Squalene oil containing Cithrol DPHS (to limit the extract volume required for the experiment). Then both the carrier fluid (Squalene oil with Cithrol DPHS) and the dispersed phase tubings were plugged into the inlet of the PDMS T-junction device. Droplets were produced by adjusting the flow rates of the carrier liquid and the dispersed phase. The flow rate usually starts at 50 μL/h for both phases and was adjusted later based on a visual inspection of the droplet production.

Pipetting method: For producing polydisperse droplets, we added 5 μL of the spindle assembly reaction to 50 μL of Squalene oil with Cithrol DPHS in a 1.5 mL Eppendorf tube. Using a P200 with the pipette set at 50 μL, pipetting up and down 5-10 times, keeping the tip pressed at the bottom of the tube produced the droplets.

Observation sample preparation and imaging

The observation sample was usually prepared by transferring 5 μL of the generated droplet into a glass-bottomed IBIDI chip containing 200 μL of Squalene oil. The droplets inside these cham-

bers sometimes moved while imaging. Due to this reason, samples were also prepared using SecureSeal™ chambers (9 mm diameter and 120 μm thickness). Here, 4 μL of these droplets were squeezed between a microscope slide and coverslip with the SecureSeal™ spacer. For the experiments requiring a rotating magnetic field, the Helmholtz stirrer with Arduino controller was used with a magnetic field of 2.4 mT.

The produced droplets were imaged using the SD or SP5 microscopes: Imaging with the SD microscope was performed with 20x and 63x oil immersion objectives using the DFC360 FX camera in epifluorescence mode or with the Roper Evolve EM CCD camera utilizing the spinning disc unit. The SP5 imaging was also performed with the 20x, 63x oil immersion, and 100x oil immersion objectives. Images were recorded at 512 x 512 pixels with pixel size chosen according to Nyquist's theorem with monodirectional scanning (scan frequency was above 400 Hz and adapted with the image resolution). The DAPI/Hoechst was excited at 405 nm with a 416-500 nm detection range. Rhodamine tubulin was excited at 561 nm and detected around 575-650 nm (the corresponding filter sets were used in the SD microscope). The SP5 microscope was mainly used for high-resolution imaging to detect mitotic spindles, and the SD microscope was employed for simple droplet observation with occasional high-resolution imaging. Both microscopes were also used to obtain transmission brightfield images of the droplets.

5.1.2.2. Results and discussion

The *Xenopus* extract cycled back to the mitotic phase from interphase and was immediately encapsulated into cell-like droplets to study the mitotic spindle formation inside a confined environment. The successful production of the extract-encapsulated droplets is evident in Figure 5.2a. The background fluorescence enabled us to distinguish the droplet and its shape and size. Some reconstituted microtubule structures can be identified from the fluorescence intensity inside the monodisperse droplets. Some representative structures observed in these droplets are shown in Figure 5.2b-e. The most prominent structures observed in these droplets included aster-like structures (Figure 5.2e) and some random microtubule organizations. Half spindles (Figure 5.2d) and spindle-like structures (Figure 5.2b, c) were also observed in the produced droplets. The frequency of these observations was very less compared to the random structures. These observations were similar to the previous realizations by Good et al. [12] and Hazel et al. [13]. The droplet production protocol and the stochastic nature of the distribution of sperm heads and other constituents in the encapsulated droplet may influence this reduced frequency in mitotic spindle observation and the occurrence of different microtubule structures.

We faced several challenges with this project, which are discussed here. (i) The main problem was concerned with the quality of the extract; bad-quality extracts resulted in the mitotic spindle not being obtained in the droplets. The day-to-day variability of the extract quality was the real challenge in optimizing the protocol. Some periods during the project when we could not obtain extracts also affected the project. Since this variability in quality and availability are intrinsic to the

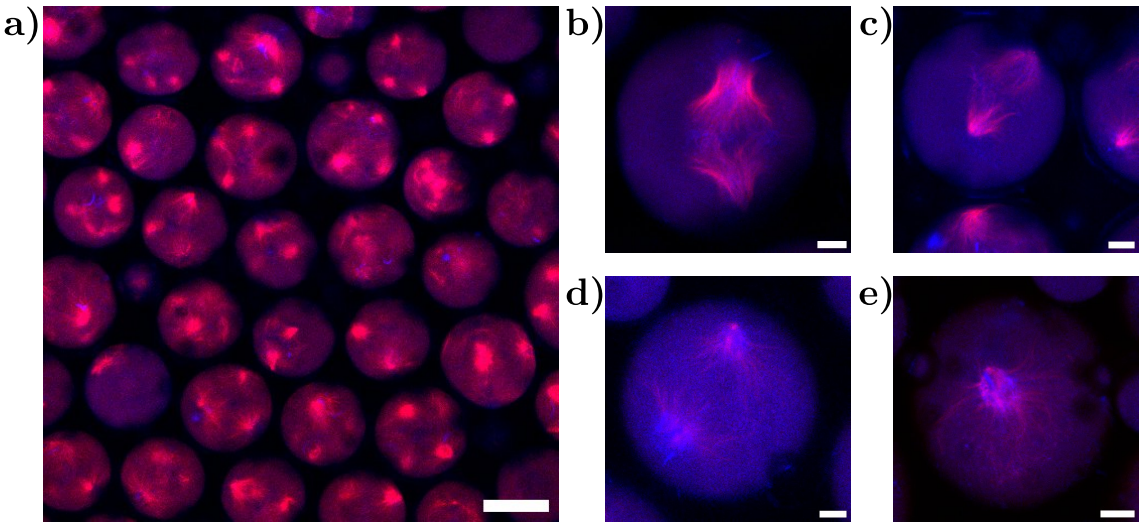

Figure 5.2.: Spindle assembly reaction inside droplets: **(a)** Images of droplets containing cycled extract in chamber. The shape of the droplets are distinguishable from the fluorescent background. Some organized structures are visible inside the droplets. Representative images of the droplet with organized **(b)** mitotic spindle-like structures, **(c)** bipolar mitotic spindle, **(d)** half spindles like structures, and **(e)** aster-like structure. The microtubules are labelled with Rhodamine tubulin (red) and chromosomes with DAPI/Hoechst (blue). The scale bar for **(a)** is 100 μm and **(b, c, d, e)** are 20 μm.

biological system (frog and its eggs), the improvement was out of our hands. (ii) Initial phases of the project were also plagued with bonding issues with the PDMS chip, which was later solved by improving the bonding protocol. The main improvement in the protocol was finding the time and intensity of plasma exposure. We found that exposing the surfaces for 20 s at HIGH intensity plasma resulted in good bonding. (iii) There were also some stages during the project where sticking extract to the microfluidics channel's border resulted in experiment failure. It was solved later by flushing the channels with Squalene oil before introducing extract for droplet production (or using the pipetting method to produce droplets). Solving issues (ii) and (iii) with good extract helped us to produce droplets and achieve mitotic spindle and aster-like structures inside the droplet.

After successfully realizing the mitotic spindle structures inside the droplet, we encapsulated MSBs containing extract to study the effect of the mechanical perturbation on mitotic spindle formation and its length scaling. Despite several experiments with different extract batches, we rarely observed mitotic spindle structures in these droplets. Nevertheless, aster-like structures and random microtubule organizations were frequently observed in these droplets. When these droplets were addressed with a rotating magnetic field, a global rotation or shaking was observed and went out of focus during measurements. Due to this reason, we could not extract any valuable insights from this experiment. Achieving a good mitotic spindle alongside addressable MSBs was challenging, as obtaining a mitotic spindle alone inside the droplet has a stochastic nature. In addition, we could not significantly improve the protocol for obtaining mitotic spindles with MSBs during this period due to the unavailability of good-quality extracts. Nevertheless, we observed the deformation of the mitotic spindle shape upon MSBs agitation in a large droplet (see Appendix A.6).

5.1.2.3. Conclusion

In conclusion, we successfully prepared CSF extract and realized mitotic spindle and aster formation in cell-like extract droplets. Even though we saw the deformation ability of MSBs in large droplets, we could not successfully study the effect of MSBs agitation on mitotic spindle formation in droplets. The main reasons for this were the day-to-day variability in the extract quality and the difficulty of these experimental procedures.

5.2. Self-organization of interphase extract into protocells

In the most general sense, self-organization is the ability of a system to organize itself into ordered spatiotemporal patterns by its own internal interactions. The self-organization is well studied, and it has also been widely recognized as a core principle for pattern formation in various systems. Self-organization can be set apart from self-assembly as it requires constant energy for maintaining order and self-organization, therefore it is typically occurs in non-equilibrium or dissipative systems [1].

In 2019, Cheng et al. showed a spontaneous de novo self-organization of homogenized egg extracts from the amphibian *Xenopus laevis* into cell-like compartments (will be refers as protocells here after). The protocell formation were completed within 30 min in the presence of demembranated sperm heads with a typical diameter of 300-400 μm, which did not appear to be coordinated by any propagating signal. Similar protocells were formed in the absence of sperm heads but it took much longer to form. The interphase extracts contain cycloheximide, which inhibit protein synthesis, so the protocell formation was independent of any genomic input [14]. The protocell patterns formed resembled the cells in *Drosophila* wings [224, 225], the monolayers of epithelial tissue [226], or the spatially ordered arrangements in oocytes [227]. The formation of protocells was indeed a self-organization phenomenon, as it is abolished by adenosine triphosphate (ATP) depletion as well as blocking microtubule polymerization and dynein motors; but inhibiting kinesin motors and actomyosin has little or no effect [14].

Due to its reduced complexity, we used this as a model system to investigate the general principle of spatial organization and compartmentalization in living matter. To this end, we examined three different aspects:

1. Explored the formation of protocells in a chamber over time and quantified the effect.
2. Determined the effect of the microtubule-stabilizing drug taxol on protocell formation and compared it with no drug case.
3. Investigated the effects of spatial confinement in protocell formation using microfluidic chambers.

The first and second points were thoroughly addressed in our article published in Development [228]. In this article, we attempted to quantify the phenomena of protocell formation and identify

the signs of disordered hyperuniformity. With the support of Ph.D. student Mr. Sebastian W. Krauss, I performed the experiments for this work and did the initial data analysis. Postdoc Dr. Pierre-Yves Gires and Prof. Matthias Weiss performed the in-depth data analysis. Therefore, I concentrated on the study's experimental part and the main outcomes in this thesis. The results were obtained by reanalyzing the data using Dr. Gires' MATLAB scripts. The buffers and materials related to this work are provided in the appendix section A.1.

5.2.1. Protocells formation in chambers

5.2.1.1. Sample preparation and imaging of protocell evolution

Sample preparation: For imaging protocell evolution in chambers, the interphase extract (see section 3.1 and A.1 for the extract preparation protocol) was supplemented with 1 μm polystyrene beads (1% by volume of stock solution), FITC-dextran (1% by volume of stock solution). The same pattern was produced in the absence of FITC-dextran or polystyrene beads. However, the contrast between the protocell centers and their periphery was significantly lower, which made image analysis more difficult. By making up the difference with pure DMSO, the DMSO concentration of the extract was kept constant at 1% volume fraction in all instances. Taxol (0 - 2 μM) was also added to some extracts to enhance microtubule stabilization without causing major changes in the cytoskeleton [229]. Gently flickering, pipetting three to four times with a cut tip, and carefully inverting the Eppendorf tube were used to merge added components to the extract. The extract needs to be well mixed and handled with caution to get good consistent results. If not, it can distort the results.

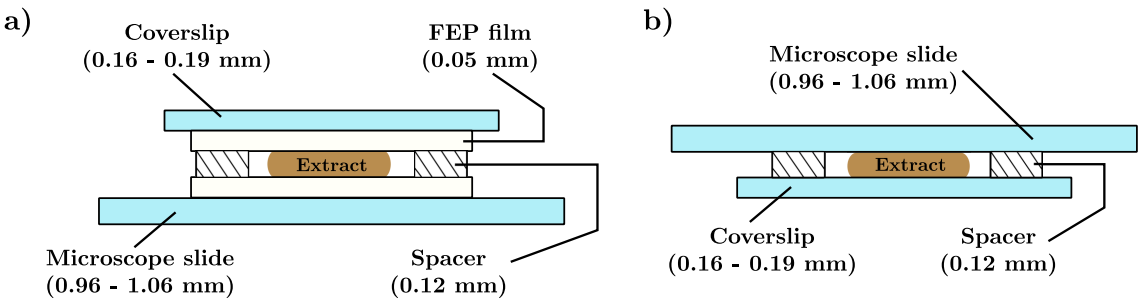

Figure 5.3.: Design of the imaging chambers: (a) Chamber design used for imaging the protocells droplet in low magnification. **(b)** Chamber design used for imaging microtubules. Here Aquapel treated microscope slide and coverslip were used instead of FEP film to adapt the working distance of the objective.

We used SecureSeal™ double-sided adhesive spacers to prepare the imaging chambers. These spacers have a thickness of 120 μm and punched holes of 9 mm in diameter. First, we covered the coverslip and microscope slide with fluorinated ethylene propylene (FEP) tape. This FEP coating was done at least one day in advance to avoid an uneven surface that would affect pattern formation. We attached the SecureSeal™ spacer to the FEP-coated surface of the microscope slide. We have at

least four chambers in a sample to get the maximum possible data. After filling each chamber with 4 μL of the prepared extract, the chamber was immediately sealed with the FEP-coated side of the coverslip to prevent evaporation (For chamber design, see Figure 5.3a). We immediately used this sample for imaging the protocell formation.

Protocell imaging: These samples were imaged with one of the following two microscopes in a tile-scan mode: a SD inverted microscope with an HC PL S-APO 10x/0.30 DRY objective and a Leica DFC360 FX camera or a SP5 confocal laser scanning microscope with an HCX PL APO CS 10x/0.40 DRY UV objective with 3.03 μm pixel width (512 x 512 pixel tiles) and open pinhole. In both cases, brightfield images were recorded, with an additional fluorescence channel on the SP5 for detecting FITC-dextran (Excitation: 496 nm, Emission: 511-550 nm). The extract was imaged for more than four hours at room temperature ($\sim$20°C) with a minimal time interval between consecutive tile scans.

5.2.1.2. Sample preparation and imaging of microtubules in the protocell

Sample preparation: To visualize microtubules in protocells, resuspended rhodamine-labelled tubulin from the bovine brain in 1 μL of a 1 mM GTP-containing general tubulin buffer and 8 μL of fresh interphase extract. An imaging solution was then prepared by combining 3 μL of this solution with 50 μL of premixed interphase extract prepared in the previous section 5.2.1.1.

The imaging samples were prepared in the Aquapel treated microscope slide and coverslip in the 120 μm thick SecureSeal™ double-sided adhesive spacer with a 9 mm diameter punched hole. To improve the temporal resolution of the imaging, we only have one chamber in the microtubule imaging sample. We prepared the sample by attaching the SecureSeal™ spacer to the microscope slide and pipetting 3 μL of the extract into the chamber. Finally, the chamber was quickly sealed with a coverslip to avoid evaporation (For chamber design, see Figure 5.3b). The sample was immediately imaged with the microscope.

Imaging microtubules in the protocell: Fluorescence imaging was performed with a SP5 confocal laser scanning microscope in a tile-scan mode, using an excitation wavelength of 561 nm and a detection range of 575-650 nm. Images (512 x 512 pixels, pixel size chosen according to Nyquist's theorem) were acquired with mono-directional scanning (scan frequency 400 Hz) within a maximum period of two hours, using a HCPL APO 100x/1.40 OIL or a HCXPL APO 63x/1.4 OIL CS2 objective at room temperature ($\sim$20°C).

5.2.1.3. Results and discussion

The self-organization of homogenized *Xenopus* interphase extract in chambers (Figure 5.4a) into cell-like compartments (hereafter referred to as protocells) was observed within 30-50 min at room temperature (Figure 5.4b). This self-organization of slab-like droplets into protocells were similar to the previous report by Cheng and Ferrell [14]. Instead of the random emergence of protocells at different spatial locations, the entire protocell has emerged simultaneously. This suggests a global onset of pattern formation similar to Turing pattern formation or spinodal decomposition. These formed protocells were also increasing in size over time by merging nearby protocells. After about three hours, the protocell pattern started to fade and disintegrate, likely due to the lack of energy molecules required to sustain the active process. Due to the presence of microtubules, endoplas-

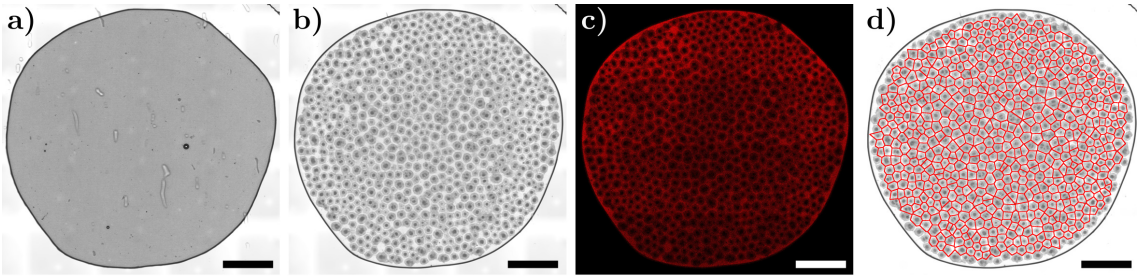

Figure 5.4.: Representative images of protocell formation in chamber: Brightfield images of the slab-like droplet **(a)** before and **(b)** after protocell formation. **(c)** Fluorescence image of the protocell reveals the accumulation of FITC-dextran in the boundary zones between protocells. **(d)** A Voronoi tesselation captures the protocell geometry. The taxol concentration inside this extract is 0.1 μM. Images were taken **(a)** 7 min and **(b, c, d)** 175 min after chamber sealing. The scale bar is 1 mm.

mic reticulum (ER) and mitochondria, the protocells showed higher absorption than the boundary zone, which is mostly free of these components [14]. Therefore in transmission brightfield imaging, protocells appear as dark grey region with brighter boundary zone (see Figure 5.4b). Since microtubules are denser around the periphery, the center of the protocells also has a lower absorbance. Due to the shuttling of mitochondria and other organelles, the center of the protocells is crowded, and microtubules may be responsible for this influx [14]. Trace amounts of 1 μm polystyrene beads (hereafter referred to as beads) and FITC-dextran were added to the interphase extract to exploit and understand this permanent radial influx. The experiment carried out for tuning the beads concentration is discussed in Figure A.7.

The added beads were eventually concentrated at the center of the protocell. In contrast, most of the inert FITC-dextran was excluded from the interior of the protocell and accumulated in the boundary region (Figure 5.4c). This exclusion of inert macromolecules was similar to the observation in living culture cells [230]. From the observations, adding beads and FITC-dextran did not seem to perturb the protocell formation.

The effect of the microtubule-stabilizing drug taxol on protocell formation was also studied using this system. The addition of taxol affected the protocell size, decreasing protocell size as taxol

concentration increased. Before going into the detailed analysis of the protocell and its evolution over time, we can look at the different factors affecting the experimental realization and image analysis of the protocell.

Factors affected the protocell formation experiment

The factors that affected successful protocell formation and the subsequent image analysis include extract quality, issues with homogenization and mixing of extract, chamber sealing time, bubbles in the chamber, intensity fluctuation during acquisition, etc. These factors are discussed in greater detail below.

Quality of the extract: Only good-quality extracts resulted in the successful formation of protocells. Each experimental day is unique, as the quality of the eggs and subsequent extract depends on the laying frog. From our experience, stressed frogs lay bad-quality eggs or no eggs. Problems that occur during the extract preparation can also affect the quality. Due to these reasons, we can expect an extract to extract quality variation. So we tested all the extracts made that day and continued only with the one showing successful protocell formation.

Homogenization and mixing of the extract: Homogenization of the extract was one of the most important prerequisites for good protocell formation. We tried different approaches, such as vortexing, pipetting with a cut-off tip, and multiple inversions of the Eppendorf tube. The extracts homogenized by vortexing did not result in protocell formation. However, extract homogenized by gentle pipetting by cut-off pipette tip and inverting the Eppendorf tube resulted in protocell formation. So gentle handling of the extract is necessary to obtain protocells. In addition, mixing the extract unevenly can lead to non-homogeneous protocell formation. In our experiments with taxol, improper mixing led to non-homogeneous protocell formation, and these results can sometimes mislead us from the actual outcome (see Figure A.6a for a representative image with non-homogeneous protocells).

Inhomogeneity of the surface: The bubbles and debris trapped in the FEP film were one of the problems encountered at the beginning of the project. These bubbles and debris created an inhomogeneous surface and affected the protocell formation and the subsequent image analysis. Improving the FEP film covering protocol and resting the covered microscope slides and coverslips for more than 12 h reduced the inhomogeneity.

Sealing time of the chamber: Due to the time clock of the extract and the long duration of experiments, multiple chambers were imaged simultaneously. The most common observation with these samples was the ring-shaped structure reminiscent of the extract droplet pipetted into the chamber. This ring structure also affected the formation of protocells around them and subsequent

image analyses. Thus, the experiment with different chamber sealing times revealed that sealing the chamber immediately after placing the droplet helped to prevent ring formation (see Figure A.5). The ring structure formation was due to the sedimentation of molecules at the droplet boundaries and was time sensitive. We concluded that immediate sealing would limit this sedimentation and result in a uniform slab-like droplet. As a result, in our subsequent experiments, the chambers were closed in less than a minute, allowing us to reduce the ring formation problem.

Bubbles in the extract droplet: The bubbles trapped inside the droplet were also a problem with the protocell experiment (see Figure A.6b for a representative droplet with bubble). Most of the time, it came from the extract's mixing step inside the Eppendorf tube. This problem can be eliminated by carefully carrying out the mixing step. We removed some bubbles inside the pipetted droplet using a syringe needle before the chamber sealing. As discussed in section 3.3.2.1, the remaining bubbles were filtered out during image analysis to extract the protocell information.

Intensity fluctuation: The protocell formation was imaged using transmission brightfield imaging in a tiles scan mode. In some experiments, there were problems with intensity fluctuations between the tiles (see Figure A.6b for a representative image of a droplet with merged tiles having different contrast, which comes from the intensity fluctuation during measurement). These intensity fluctuations were a problem for our image analysis script. It came from the transmission light bulb and changing it solved this problem.

In addition to above, concentration of DMSO and beads inside the droplet was also investigated. The DMSO was also known to stabilize microtubules; however, only higher concentrations affected the protocell formation in our observations, and at 1%, protocell patterns remained similar to the untreated extracts. From the experiments it was identified that 1% DMSO concentration and the presence of beads had no significant effect on protocell formation. By using the improved experimental protocol, we obtained sufficient data to analyze the protocell formation and its evolution in the presence and absence of taxol. This analysis is discussed in the following section.

Protocell formation and its time evolution

The protocell geometry and its time evolution were analyzed using the Voronoi tesselation (see section 3.3.2.1 for the detailed discussion of the image analysis and Figure 5.4d for a representative tesselation). The good contrast between the protocell center and boundary zone enabled us to use the Voronoi tesselation to extract the protocell geometry. In addition, the beads accumulated at the protocell's center also enhanced the contrast and helped in image analysis.

This tesselation approach enabled us to deeply analyze the protocell geometry and its time evolution rather than mere visual quantification. As a first step, we looked at the local geometry of protocells at two different times, right after the protocell first appeared and 1-2 h later. The proto-

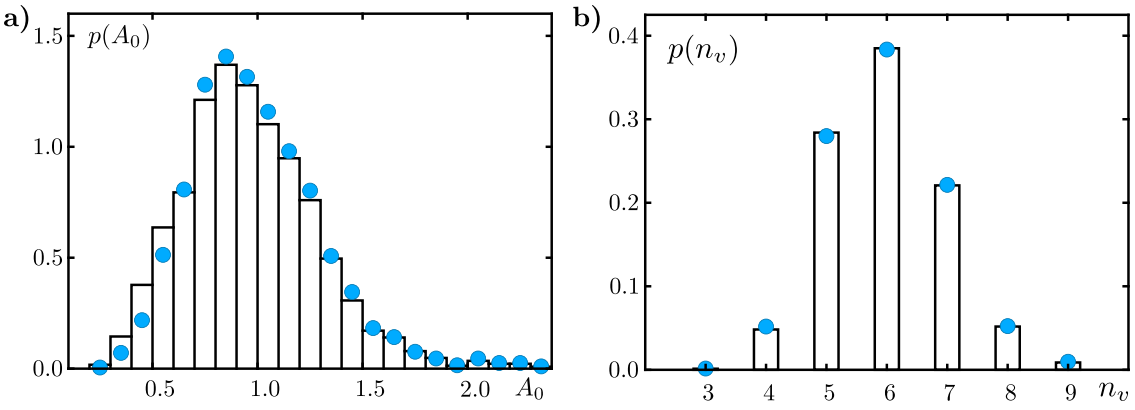

Figure 5.5.: Analysis of protocells geometry: (a) The PDF of the normalized areas, $p(A_0)$, right after the first emergence of protocells (black histogram) and 1-2 h later (blue circles) have a narrow peak around unity and are similar. **(b)** The PDF of the vertex numbers, $p(n_v)$, of protocells also has a similar pattern at the first emergence of pattern formation (black histogram) and 1-2 h later (blue circles). The most frequent phenotype is the hexagons, followed by the pentagons and heptagons.

cell area, A and vertex number, n_v were extracted from images of different experiments and times using the Voronoi cells. In order to consider the varying average protocell areas, normalized area $A_0 = A/\langle A \rangle$, was calculated by dividing with the mean area of the respective image. Since a Kolmogorov-Smirnov test (5% level, performed by Prof. Weiss) revealed no significant difference between the normalized quantities for different experiments, we combine these with comparable time points to obtain the probability density functions (PDFs) $p(A_0)$ and $p(n_v)$. The extracts with low amounts of taxol ($\leq 0.1\,\mu$M) were added to the above PDFs as it does not show a significant difference with extracts without taxol.

The data analysis affirmed the visual impression of more or less homogeneous nature of the protocells. The PDF of the normalized protocell areas ($p(A_0)$) had a narrow distribution around unity, and this feature was held constant at different time points of the protocell evolution (see Figure 5.5a). This quantification was similar to the observations with the MDCK-II tissue growth on surfaces with different rigidities [226]. Furthermore, analysis of the PDF of vertex numbers ($p(n_v)$) revealed that hexagonal cells predominate with a considerable number of pentagonal and heptagonal cells with the rare occurrence of higher vertex numbers (see Figure 5.5b) suggests a slightly disordered hexagonal arrangement of protocells. This was similar to the patterns observed in *Drosophila* syncytial blastoderms [231], epithelial monolayers [226], and the aster arrangement of *Phallusia* oocytes [227].

Taxol-induced changes in the protocell pattern formation and its time evolution

One of the main components contributing to protocell formation is the arrangement of microtubules [14]. The confocal fluorescence imaging of the microtubule using labelled tubulin unraveled the radially arranged microtubules inside the protocells (see Figure 5.6b). Since microtubules are the main component of protocell structure, we investigated the effect of stabilizing the microtubule

polymerization in pattern formation. Taxol is an anti-cancer drug known to stabilize microtubules without inducing major changes to cytoskeletal elements [229]. So we supplemented fresh interphase extracts with different concentrations of taxol, as discussed in section 5.2.1.1. The taxol introduction resulted in changes in the length scale of protocells size. Increasing the taxol concentrations resulted in smaller protocells (see Figure 5.6a).

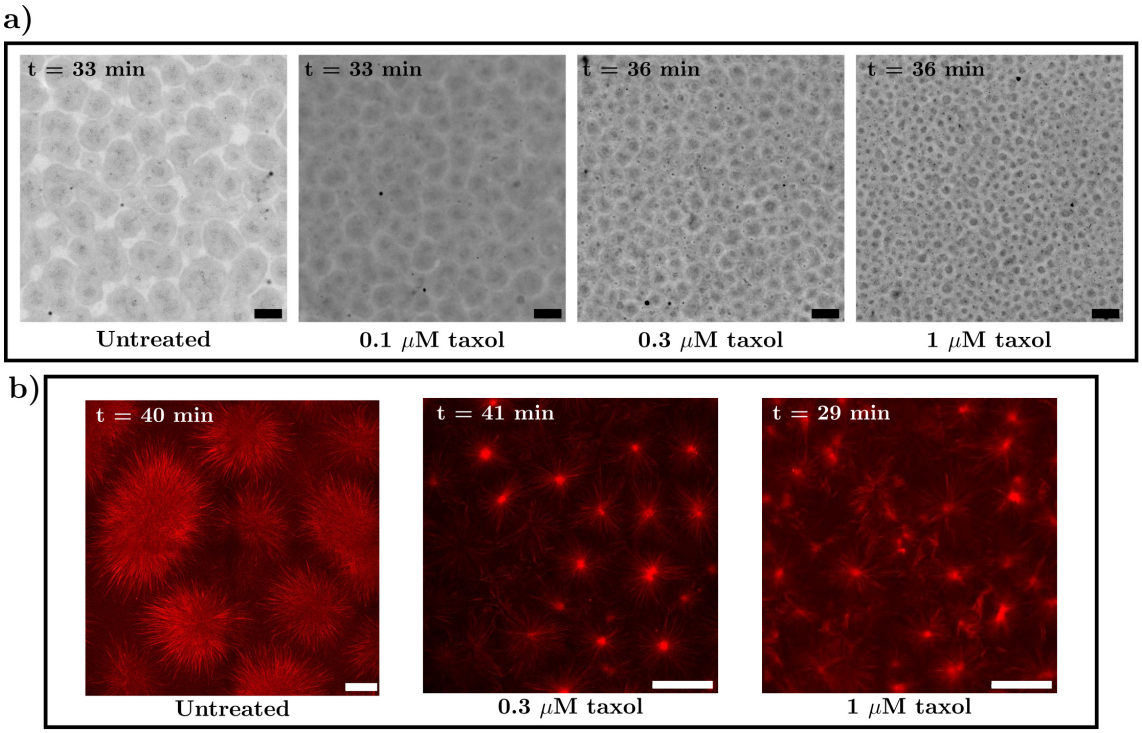

Figure 5.6.: Effect of taxol on protocells: Representative **(a)** transmission brightfield images and **(b)** fluorescence microtubule images of the protocells at the indicated taxol concentration and time. **(a)** Reduction in the protocell size was visible with increasing taxol concentration. **(b)** In line with brightfield images, the size of the radial flower-like microtubule arrangement also reduced its size upon increasing the taxol concentration. The scale bar for **(a)** is 200 μm and **(b)** is 50 μm.

A uniform distribution of microtubules was observed in the confocal fluorescence imaging of untreated extract at the beginning, which was later radially arranged to form the protocells (see Figure A.8a). It was similar to the previous observation in *Xenopus* cell-free extract system with fluorescent tubulin and artificial centrosomes [232], and in the artificial system made from purified components [11, 233, 234]. In the presence of taxol, several concentrated microtubule regions were initially observed and were not as tidy as in the untreated case (see Figure A.8). These concentrated regions formed radial microtubule structures with a reduced length scale, resulting in smaller protocell sizes (see Figure 5.6). The protocell pattern's decreasing length scale was most likely due to a reduced fraction of long microtubules caused by taxol-induced suppression of microtubule dynamics [235, 236].

The above observations can be explained by the following; (i) the lack of translation due to cycloheximide addition in the interphase extract results in a limited pool of tubulin and microtubule

associated proteins (MAPs) [237]. (ii) The dynamic instability of the microtubules will eventually result in longer microtubules at the expense of unsuccessful shorter ones. (iii) The taxol addition, in turn, stabilizes the microtubule seeds, resulting in more shorter microtubules and their bundles. This can, in turn, result in more number of shorter protocells in the presence of taxol.

An increasing size due to the fusion of neighbouring protocells was also observed in the later stages of the protocell's time evolution (see Figure A.10 for an example). This fusion was possibly driven by the cross-linking of anti-parallel microtubules by dynein motors at the junction of two protocells, similar to the scenario presented by Mitchison et al. [232] and the simulation by Khetan et al. [227]. The pattern formation starts to disintegrate after about two hours. The process of disappearing of the pattern starts at the outer borders of the extract and progresses in a wave-like manner towards the center (see ref. [238] for a detailed discussion about apoptosis and its trigger wave). Eventually, the extract appears as a homogeneous liquid with some granularity. We believe that this is due to the lack of energy-rich molecules (e.g., GTP and ATP) in the system because they have already been consumed. However, it may also be due to some internal clocks in the system, as it was unable to continue cell division like a normal frog egg.

The images were analyzed using Voronoi tesselation as before to quantify the effects of taxol addition. The average protocell area ($\langle A_P \rangle$) calculated at 70-90 min after the chamber sealing revealed the visual impression of a reduction in protocell size upon increasing the taxol concentration (Figure 5.7a). Similar observations were reported by Khetan et al. in the microtubule aster of *Phallusia* oocytes [227]. In addition, the mean average fractions ($\langle \phi \rangle$) of the pentagons, hexagons and heptagons were also unaltered upon taxol addition (Figure 5.7b). The PDFs of the normalized areas of the protocells treated with taxol also had a similar shape to the untreated extract (see ref. [228]). From this analysis, we can understand that the taxol addition preserved all geometrical features while only reducing the intrinsic length scale. This can be linked with the shorter microtubule resulting from the taxol stabilization.

To understand the dynamics of the protocell temporal evolution, we analyzed the average protocell area, $\langle A_P \rangle$, as a function of time for all the different taxol concentrations. At all concentrations, the protocell showed linear growth following $\langle A_P \rangle \approx \gamma t$ (see Figure 5.7c and A.9a), with the growth rate (γ) decreasing with an increase in taxol concentration (Figure 5.7d). In line with the results, the number of protocells also reduces at a rate $\sim 1/t$ (see Figure A.9b), implying a constant overall protocell area. Adding to that, a small variation in the $\langle A_P \rangle$ can be observed between different experiments for the same concentration, but overall features exhibit similar behaviour (Figure 5.7c). As discussed, the reduction in protocell number was due to the merging of nearby protocells (see Figure A.10). In addition to the above analyses, the analysis of the long-range order of protocell patterns revealed that they do not exhibit hyperuniformity at any given time, despite the possibility of appearing visually similar to a near-crystalline arrangement (see ref. [228] for details).

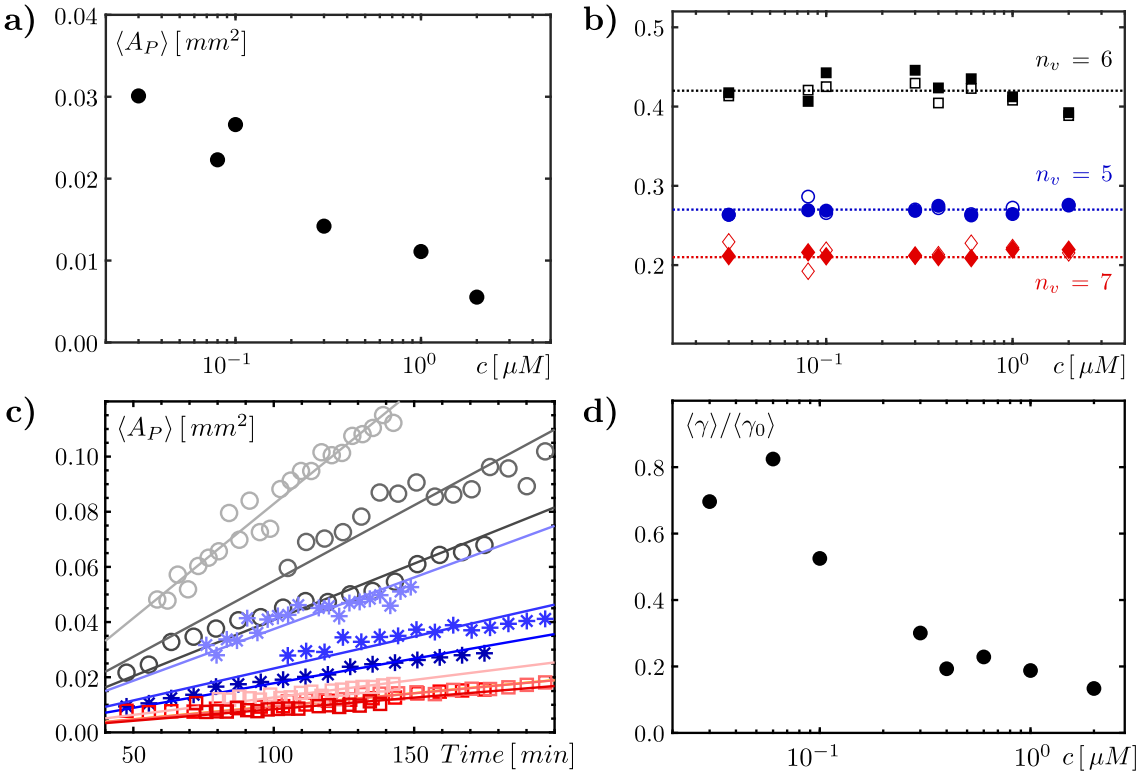

Figure 5.7.: Analysis of taxol-induced effect on protocell geometry and its time evolution: **(a)** The average protocell area ($\langle A_P \rangle$) obtained at 70-90 min after starting the experiments decreases with increasing taxol concentration (c). **(b)** The average fraction ($\langle \phi \rangle$) of pentagonal, hexagonal and heptagonal protocells remained constant across all taxol concentrations c, regardless of when the pattern formed (open and filled symbols; immediately after the pattern emergence and 1-2 h later). **(c)** Representative time courses of the average protocell area ($\langle A_P \rangle$) for different concentrations (circles, asterisks, squares for c = 0, 0.1, 1 μM; different colours indicate different experimental repeats) captured by an linear relation $\langle A_P \rangle = \gamma t$ (full lines). **(d)** The mean area growth rate, $\langle \gamma \rangle$, decreases with increasing taxol concentrations, c, and reaches about 15-20 % of the value for the untreated extract, $\langle \gamma_0 \rangle$ at 2 μM.

Based on our analysis, the protocell patterns emerged simultaneously at all positions by the uptake of materials from the surroundings. The taxol addition stabilized microtubules, created shorter microtubules that resulted in smaller protocells. The protocells enlarged over time by merging nearby protocells at a growth rate dependent on the concentration, which decreased with an increase in the concentration. Furthermore, the geometrical features of the pattern other than the intrinsic length scale were invariant over different taxol concentrations and times.

Stirring of protocells

A small amount of MSBs were added to the fresh interphase extract to investigate the effects of MSB stirring/agitation on protocell formation (see Figure A.11 for an overview of protocell stirring). Similar to the polystyrene beads, the MSBs also resulted in protocell formation. Addressing the MSBs with a rotating magnetic field of 0.1 Hz from the beginning also did not hamper the protocell formation. The MSBs were rotating initially but were trapped and immobile once the extract started

forming the protocells. Like polystyrene beads, MSBs were transported to the protocell's center and appeared as aggregates. The MSBs rotated again only once the protocells started to disintegrate after 1-2 h. The rotation started at the droplet's border and moved to the center along with the protocell disintegration wave.

5.2.1.4. Conclusion

In conclusion, we studied the protocell formation and its time evolution in the presence and absence of taxol. The protocell formation pattern was similar to the observation with aster arrays of *Phallusia* oocytes and *Drosophila* syncytial blastoderm. The protocell length scale reduced with increasing taxol concentrations with similar geometrical features. The protocell size increased over time and its growth rate decreased with increasing taxol concentration. Furthermore, the addition of beads, FITC-dextran and MSBs did not affect the protocell formation. Adding to that, we also observed the stabilizing effect of taxol on microtubules using confocal fluorescence microscopy. Therefore, an in vitro system like this can reduce the living system's complexity and reveal its common principles.

5.2.2. Protocells formation in microfluidic channels

After successfully studying the protocell formation in a large slab-like droplet, we were intrigued to study the effect of the chamber size and shape on the protocell formation. Most fascinating were the sizes and shapes resembling an egg. So we prepared chambers in the microfluidic chip with varying geometries using our knowledge of the microfluidic system and handling *Xenopus* extracts in microfluidic channels. The experiments in these chambers are discussed in this section and were carried out together with Ph.D. student Mr. Sebastian W. Krauss.

5.2.2.1. Sample preparation, chamber filling and imaging

Sample preparation: Similar to the protocol discussed in section 5.2.1.1, the interphase extract was supplemented with 1 μm polystyrene beads (1% of the volume of the stock solution), FITC-dextran (1% of the volume of the stock solution), and small amounts of taxol (0 - 1 μm). In addition, the DMSO concentration in the extract was maintained at 1% volume fraction.

Chamber filling with extract: The microfluidic chips with different chamber geometries were prepared as discussed in section 3.2.6 and soaked in Milli-Q water at least a day in advance to reduce flow inside the system. The Milli-Q water inside the soaked chip was flushed with a pipette before beginning the extract filling. Then a small piece of PTFE tubing was inserted into the outlet to mimic the conditions in the inlet. One end of the long PTFE tubing (inner diameter 0.5 mm and outer diameter 1.58 mm) with proper cut ends was carefully attached to an 18-gauge needle

connected to a 1 mL syringe. Then the extract was carefully sucked into the other end of the PTFE tubing, avoiding any trapped bubbles. Subsequently, the extract-filled end of the PTFE tubing was connected to the microfluidic chip's inlet. The chambers were then carefully filled with this extract, avoiding bubbles. When the extract was coming out of the outlet, filling the chambers, the inlet tube was carefully cut with a scissor so that the inlet tube had the same length as the outlet tube, making a similar situation on both ends. Finally, the inlets and outlets were sealed immediately using vacuum grease to avoid evaporation (see Figure 5.8a for a representative filled microfluidic chamber).

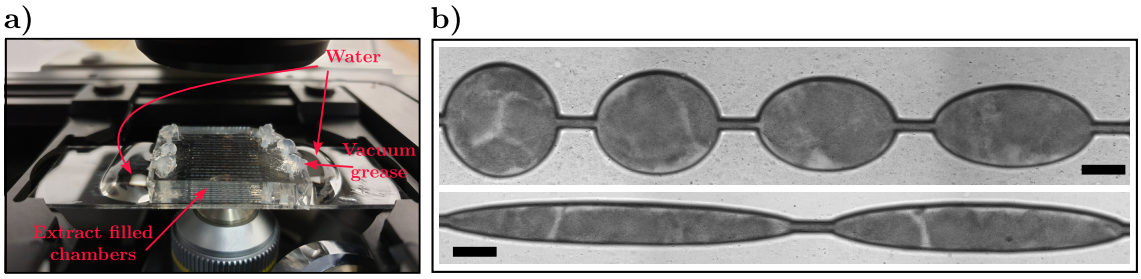

Figure 5.8.: Extract filled chamber and its brightfield image: (a) Representative image of a microfluidic chip with extract-filled chambers mounted on the inverted microscope. The inlets and outlets were sealed with vacuum grease and Milli-Q water was pipetted on either side of the PDMS to reduce flow inside the chamber. **(b)** Protocells formed with untreated extract in the small microfluidic chambers at 97 min (just before pattern disappearance). The protocells formed adapted their shape based on the chamber geometry and have a size of more than half of the chamber in most cases. The scale bar of the image is 200 μm.

Imaging: These samples were imaged in transmission brightfield mode with one of the following two microscopes in a tile-scan mode: the SD inverted microscope with an HC PLS-APO 10x/0.30 DRY objective and a Leica DFC360 FX camera or the SP5 confocal laser scanning microscope with an HCX PL APO CS 10x/0.40 DRY UV objective with 3.03 μm pixel width (512 x 512 pixel tiles) and open pinhole. While the chip was imaged under the microscope, a drop of Milli-Q water was pipetted onto the slide, as shown in Figure 5.8a, to reduce the flow in the microfluidic chambers. The extract was imaged for over three hours at room temperature with a minimal time interval between consecutive tile scans.

5.2.2.2. Results and discussion

Similar extract as in section 5.2.1.1 was used in the microfluidic chambers to comply with the results obtained from the SecureSeal™ chambers. Pattern formation was observed in the microfluidic chambers within 30-50 min, consistent with the result obtained from SecureSeal™ chambers. In this case, too, the pattern emerged at all locations at the same time. The pattern formed in these chambers had the effect of their confined geometry. Each chamber channel system (CCS) had six replicas of ten different chamber geometries. The three CCS in one PDMS chip resulted in 18

chambers with the same geometry. Thus, working with these microfluidic chambers provides good statistics from a single experiment.

The main issues we faced with these extracts were the bubbles and the internal flow inside the system. The internal flow disrupted the protocell self-organization. Soaking the microfluidic chip in Milli-Q water at least a day in advance and adding Milli-Q water on either side of the chip helped to reduce the internal flow. The bubbles also lead to internal flow in channels by changing their size over time. However, bubble formation was reduced by carefully avoiding bubbles during extract preparation and when filling the chamber. The other factor that causes flow inside the chamber is evaporation; sealing the inlet and outlet with vacuum grease solved this problem. Furthermore, there were issues with filling the extract; incomplete filling of the chambers was common in the beginning. Adjusting the filling method and geometries to the current one (with fewer corners) and soaking the chip in Milli-Q water resulted in filled chambers.

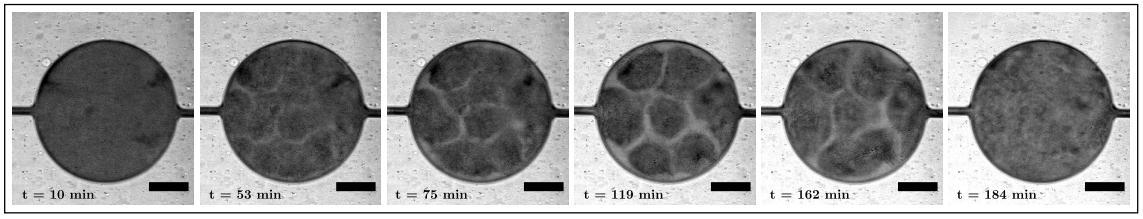

Figure 5.9.: Formation of protocells in circular microfluidic chambers: The circular microfluidic chamber with 0.1 µM taxol shows a symmetric protocell formation over time. The protocell having a well-distinguishable structure was observed with a diameter of 200 μm at 119 min. The protocell structure started disintegrating after 162 min and completely disintegrated to become a uniform extract with granularity at 184 min. The scale bar of the images is 200 μm.

In untreated extracts (without taxol), the patterns observed had more than half the size of the chambers (see Figure 5.8b). Only in small circular chambers we observed more than two protocell patterns (around 250 μm diameter). The patterns observed in other geometries had uneven sizes. The remaining part of the protocell may be in the neighbouring chambers. Furthermore, a clear separation between individual protocells was difficult to recognize, even with the eyes for most stacks in temporal development, which made automatic image segmentation difficult. As we know, taxol addition results in smaller protocells, supplemented with small amounts of taxol (0 - 1 μM) in the fresh extract.

A higher concentration of taxol (1 μM) resulted in the formation of smaller protocells similar to the observation in SecureSeal™ chambers. The size of the protocells was around 50-70 μm and was uniformly distributed in all the chamber geometries (see Figure A.12). However, these protocells were only clearly visible before the pattern disappearance. Nevertheless, still, due to the low contrast between protocells and their boundary zone, the individual protocells were difficult to observe.

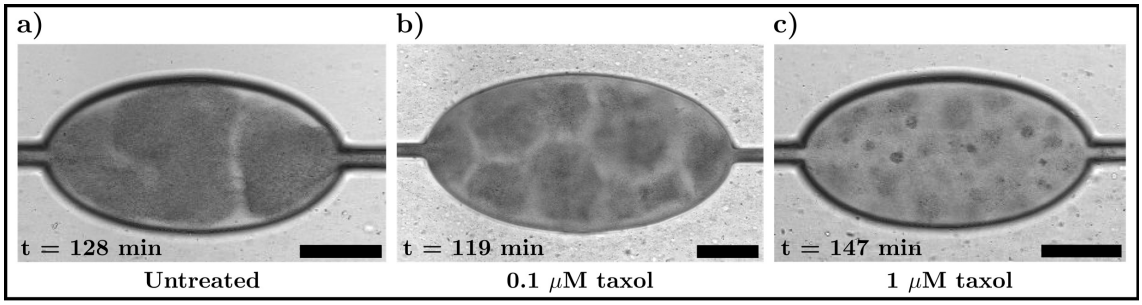

Figure 5.10.: The protocell size in microfluidic chambers with taxol concentration: Representative images show protocells formed in the elliptical microfluidic chamber with the extract supplemented with different concentrations of taxol. Increasing taxol concentration reduced the protocell sizes. The images were taken at the time points when distinguishable protocells were visible in the chamber. The scale bar of the images is 200 μm.

Lower concentrations of taxol yielded medium-sized (around 200 μm in diameter for 0.1 μM taxol), much better distinguishable protocells (see Figure 5.9 and A.13). When analyzing the time evolution of protocell formation in the microfluidic chambers, the merging of the protocell was also observed, as discussed in the SecureSeal™ chamber (see Figure A.13, as an example, which shows the time evolution of protocells with the extract containing 0.1 μM taxol). The merging event can be distinguishable in the earlier time points after the pattern emergence, but due to the low contrast of the image, it was difficult to observe even by eye. The protocell started to emerge around 40-60 min, but well-defined structures were seen only at the end, just before the pattern disappearance. The size of the protocell described here was obtained at this time point. The number and orientation of the protocells were clearly random and depended on the chamber geometries. Adding to that, the protocell emergence and its disappearance occur simultaneously in all the chambers.

As discussed, the protocell size reduces with increasing taxol concentration, and the orientation depends on the chamber geometries. This protocell pattern formation with different concentrations of taxol resembles the different stages of cell division in embryos. For example, the pattern formation in the elliptical chamber showed in Figure 5.10 resembles the different stages of embryonic division in *Caenorhabditis elegans* [239, 240]. The pattern at 1 μM taxol concentration mimics *Drosophila melanogaster* embryo [241].

Adding to that, we also encountered an interesting finding while working with the microfluidic chambers. As mentioned earlier, we have three CCS in a single PDMS chip. The CCS that filled the last showed a significant difference in the formed pattern compared to that in the first filled CCS chambers (see Figure A.13 and A.14 for a comparison). The reason may be linked to the extract's filling time, as all three CCS was filled with the same extract taken in the PTFE tubing. The long exposure (2-6 min) at room temperature during the extract filling may result in the initiation of protocell formation inside the PTFE tubing and subsequent disturbance while filling the chambers may contribute to this different phenotype. Even in this case, the protocell pattern formed in the microfluidic chamber was influenced by the chamber geometry.

Furthermore, the protocell formed at the boundaries of the chamber showed some rotational behaviour. This rotation may be due to the pulling force from the microtubule aster, as discussed in Sulerud et al. [242]. However, we did not investigate this observation in greater detail and it can be an interesting feature to explore in the future.

In addition, a detailed analysis of this pattern formation in different geometries using automatic image segmentation is a work in progress. The low contrast in the obtained images is the current issue. This issue can be overcome by a better image analysis algorithm or by improving the experimental protocol. So there is still a lot of work to be done on these roads to get a good statistical overview of the observed features.

5.2.2.3. Conclusion

In conclusion, we developed a system to study the influence of chamber geometry in protocell patterns in high throughput using a microfluidic chip. Also we discussed protocol improvements, such as soaking the chip in water, vacuum grease application, etc., to limit the flow inside the chamber that can influence the pattern formation. We also observed that the taxol concentration would reduce the protocell size and the chamber geometry influenced the pattern formation. A detailed analysis of the pattern using automatic detection is still in progress and is work for the future. Finally, the formed pattern resembles different stages in the embryonic division. So this simple in vitro system can be used to study the effect of shape dependence of the confined space in the cellular organization in greater detail.

5.3. Cell-like protocell division with cycling extracts

One of the fundamental processes in life is cell division, where the cell duplicates its content and splits into daughter cells. This process is highly regulated, and *Xenopus* extract helped to identify some of its regulatory mechanisms [243, 244]. The cycling extract is an interesting in vitro system that can perform multiple periodic cell divisions similar to a fertilized egg [23]. The biochemical cell cycle regulatory circuit is centered on the Cdk1 complex with positive and negative feedback loops [245]. The absence of cycloheximide in the cycling extract permits cyclin B synthesis and results in periodic cell cycles [14]. The cycling extract was used in the literature to study cell divisions, mitotic trigger waves, factors affecting trigger wave speed and its origin [44, 140, 246–248], etc. However, a deep understanding of the effect of cell division on geometrical confinement is yet to be done. The geometrical dependence of extract confinement will be discussed in this section. Before going to microfluidic chambers in different geometries, we first look into a simple slab-like droplet in SecureSeal™ chambers to establish the protocol. The experiments discussed here are done together with Ph.D. student Mr. Sebastian W. Krauss.

5.3.1. Protocell division in chambers

5.3.1.1. Sample preparation and imaging

Sample preparation: The cycling *Xenopus laevis* egg extract (see section 3.1 and A.1 for the extract preparation protocol) was supplemented with sperm heads to image protocell division in the chamber. The sperm head concentration was adjusted based on the previous experimental results, and it was discovered that 100 sperm heads/μL was a good choice for our current chamber. We obtained this sperm head concentration based on the experiments with sperm head concentrations ranging from 50-144 sperm heads/μL. The extract was mixed by gentle flickering, pipetting 3-4 times with a cut-off tip, and carefully inverting the Eppendorf tube. The extract must be uniformly mixed and gently handled to observe cell cycling.

The chamber was made with a microscope slide and coverslip hydrophobized with Aquapel instead of FEP film. The chamber design is similar to section 5.2.1.2 (see Figure 5.3b). The imaging chamber was made by sandwiching the extract between a microscopic slide and a coverslip, separated by the SecureSeal™ double-sided adhesive spacer having a 9 mm punched hole and 120 μm thickness. First, stick the SecureSeal™ spacer on the microscopic slide and pipette 3 μL of the extract into the chamber. The chamber was immediately closed with a coverslip to avoid evaporation. We have only a single chamber in the sample to improve temporal resolution.

Imaging: We imaged the cycling sample with one of the following two microscopes in a tile-scan mode: a SD inverted microscope with an HC PL S-APO 10x/0.30 DRY objective and a Leica DFC360FX camera or a SP5 confocal laser scanning microscope with an HCX PL APO CS 10x/0.40 DRY UV objective with 3.03 μm pixel width (512 x 512 pixel tiles) and open pinhole. In both cases, brightfield images were recorded. The extract was imaged for more than six hours at room temperature ($\sim$20°C) with a minimal time interval between consecutive tile scans.

5.3.1.2. Results and discussion

The successful preparation of the viable cycling extract was evident from the experiments in the SecureSeal™ chamber. Here we observed multiple divisions of the self-organized protocells, similar to the previous observations with the cycling extract in Teflon tubes [44, 140, 247], droplets in glass tubes [248], and slab-like droplets in chambers [14, 246].

The cycling extract filled in the chamber was initially in the first interphase stage after the meiotic exit [14] and appeared homogeneous in the transmission brightfield imaging. At around 38 min, nucleation began around the sperm heads, and protocells emerged throughout the droplets at around 74 min (see Figure 5.11). The protocells that emerged were similar to those formed in the interphase arrested extract. The cycling extracts were prepared without cycloheximide, which permits cyclin synthesis and allows multiple cell cycle events by the periodical activation and inactivation of Cdk1

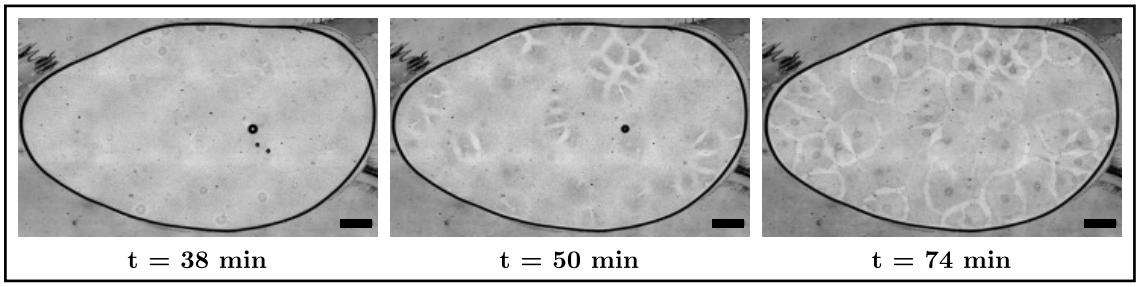

Figure 5.11.: Cell-like protocell formation in chambers with cycling extracts: Time-lapse images of protocell formation in cycling extracts supplemented with 100 sperm heads/μL. The nucleation around sperm heads became apparent at 38 min and some protocells emerged at 50 min. The mother protocells were formed at all positions in the droplet around 74 min. The scale bar is 500 μm.

[14, 44, 248]. In line with this knowledge, we observed around six consecutive cell divisions in this chamber, resulting in smaller daughter cells (see Figure A.15).

The sperm head nuclei reached the interphase state around 70 min inside the chamber at room temperature. Subsequently, it underwent multiple cycles of interphase and mitosis approximately every 40 min (see Figure A.15). The division cycle occurred in the slab-like extract droplet in a wave-like manner. The mitotic entry wave started at the border of the droplet and went radially to the center. These mitotic entry exit waves always started at the borders (See Figure A.16 for two representative waves). So these waves may be the Cdk1 trigger wave, demonstrated in the *Xenopus* cell-free system by Chang et al. [44]. A similar observation, like the triggering wave emanating from the droplet boundary, was also reported by Nolet et al. [247]. The mitotic waves were also observed in the syncytium of the *Drosophila* embryo [249, 250]. The wave-like propagation of the mitotic state spatially coordinates the cell cycle and has its origin in the cell nuclei [246, 247].

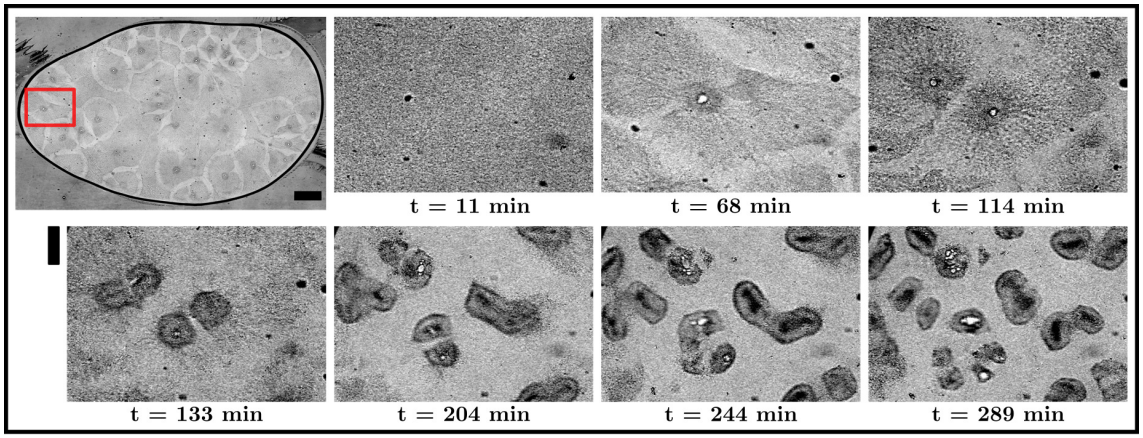

Figure 5.12.: Cell-like protocell division in chambers: Time-lapse images of the protocell undergoing five cell-like divisions in a cycling extract supplemented with 100 sperm heads/μL. The mother protocell was chosen from the region of interest marked (red rectangular region) in the slab-like droplet. Initially, the extract was homogenous, and the mother protocell became apparent around 68 min with the white nuclei at the center. Subsequently, the protocells started to undergo cell-like divisions. Images were taken when the daughter cells became evident after the cell divisions. The scale bar of the droplet is 500 μm and for the cross section is 200 μm.

In order to understand division cycles inside the slab-like droplet, we closely monitored the division of a protocell over time (see Figure 5.12). Delineated mother protocell was visible around 68 min. In the first two protocell divisions, the division direction was mutually perpendicular to each other. After the second division, not all daughter protocells were clearly separated and individually recognizable (see Figure 5.12 at 68, 114 and 133 min). So the division direction was not estimated after the second division (see Figure 5.12 from 204 min). However, judging by the visual impression of the elongated and joined daughter cells, it seems to have followed a similar trend as the first two divisions. Adding to that, sometimes observed more than two daughter protocells formed from a single mother protocell. Nevertheless, we observed several consecutive cell-like divisions in this in vitro system. This membraneless periodic cell division (see Figure A.15) looks similar to the earlier divisions in *Drosophila* embryos [251, 252].

Detailed analysis and quantification of the observables were not done in this system. The main reason was that we needed more experimental realizations to obtain enough statistics of the observed results. The cycling extract was sensitive to the steps and their corresponding time in the preparation protocol. So we took some time to establish a flawless protocol in the lab. The intermediate problem with the centrifuge used for egg crushing also delayed the process. However, we obtained preliminary results, which can be improved in the future to study cell-like division in greater detail.

5.3.1.3. Conclusion

In conclusion, we successfully established the cycling extract protocol and constituted multiple cell-like division in vitro in slab-like extract droplets. The division cycle occurred in a wave-like manner, which always originated in the droplet boundary and travelled radially inwards. The division cycles looked similar to the earlier stages of *Drosophila* embryos. Thus this system can be used in the future to study cell division in greater detail and to understand the factors that might affect protocell size, cycle time and the number of cycles that can reconstitute.

5.3.2. Protocell division in microfluidics chambers

After successfully establishing the cycling extract system, we were intrigued to study the effect of chamber geometry on the cell-like divisions. The cycling extracts in confined geometries like Teflon tubes provided good insight into the mitotic trigger wave and its origin. The Teflon tube size greatly influenced the trigger wave origin; the thinnest one has an internal wave origin, while the wave originated in the boundaries of the thicker one [247]. However, the influence of other microfluidic confined geometries on cell cycle and pattern formation is not studied in detail. Similar to the previous section, we used elliptical geometries with different aspect ratios (circle to elongated ellipse) for the cycling extract confinement. We expect different phenotypes in these microfluidic chamber confinements as the mechanical interaction is known to influence the cellular

arrangements in the early embryogenesis of *Caenorhabditis elegans* [240, 253]. In this section, we will discuss the influence of extract confinement on different microfluidic chambers on cell division. The experiments discussed in this section were carried out together with Ph.D. student Mr. Sebastian W. Krauss.

5.3.2.1. Sample preparation, chamber filling and imaging

Sample preparation: The extract preparation protocol is the same as that discussed in section 5.3.1.1. For this cell-like protocell division experiment in the microfluidic chambers, the cycling extract was supplemented with 100 sperm heads/μL. The extract was mixed carefully using a pipette with a cut pipette tip and inverting the Eppendorf tube 3-4 times.

Chamber filling with cycling extract: The microfluidic chip and the chamber filling protocol used for the cycling extract were the same as the ones used for the interphase extract (see section 3.2.6 and 5.2.2.1). The only difference was that we used the cycling extract supplemented with sperm heads instead of the interphase extract. In brief, the Milli-Q water inside the soaked chip was flushed out and carefully filled with the cycling extract avoiding trapped bubbles using the PTFE tubing connected to a 1 mL syringe. Then the inlets and outlets were sealed with vacuum grease to prevent evaporation (see Figure 5.8a for a representative image of a filled chamber).

Imaging: Brightfield imaging of the protocell division in microfluidic chambers was performed similarly to section 5.2.2.1 and 5.3.1.1. The tile scan images were acquired with the SD or SP5 microscope using the 10x objectives. In both cases, the extract was imaged for more than six hours at room temperature with a minimal time interval between consecutive tile scans.

5.3.2.2. Results and discussion

To explore the effect of geometrical confinement on cell-like division, we filled the microfluidic chambers with the cycling extract containing 100 sperm heads/μL. The observations given below are from the preliminary experiments. Further experiments and analysis are needed to affirm the common trends. We observed multiple cell-like divisions in the preliminary experiments, and the findings are discussed in this section.

The pattern started to emerge around the sperm heads in the microfluidic chambers at about 20 min (see Figure 5.13, A.17 and A.18). However, the initial organization was not symmetric and looked like the sperm head distribution inside the chamber affected the pattern. This difference in size may be due to the formation of protocells with and without sperm head nucleation [14]. The initial patterns then gathered the components in its vicinity and became a condensed structure with the sperm head at its center at around 50-70 min. The chamber geometry seems to affect these

patterns formed (see Figure A.17 and A.18). The distinguishable cell-like patterns formed were sometimes merged to become a single condensed protocell (see Figure A.17 from 42 to 105 min).

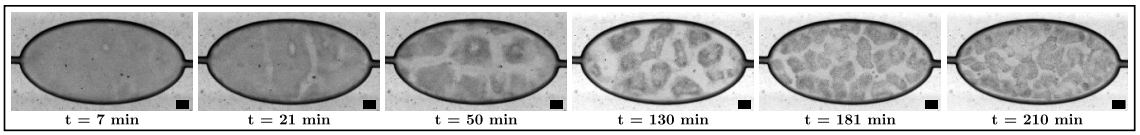

Figure 5.13.: Cell-like division in microfluidic chamber: Time-lapse images of protocell formation and cell-like division in an elliptical microfluidic chamber filled with cycling extract containing 100 sperm heads/μL. The protocell formed around 21 min. Subsequently, it underwent protocell divisions. The image sequence was not based on the time of the successive protocell divisions, as the daughter protocells were not clearly distinguishable after the second division. The scale bar is 100 μm.

Later these protocell structures underwent multiple cell-like divisions (see the protocell number variation after 70 min in Figure 5.13, A.17 and A.18). The division period was around 20-30 min for all the chambers. The daughter cells formed were not fully separated in most cases; a light greyish region was visible around the newly formed daughter cells. Along with this, the reductive nature of cell division made it difficult to follow the division cycle in the chambers. Therefore, the images given in the Figure 5.13, A.17 and A.18, represents the protocell number variation over time and it does not represent the successive cell division times. Irrespective of the chamber geometry, the daughter cells covered the whole chamber after some cell divisions. The cell-like division shown in Figure 5.13 in the later stages was similar to the *Drosophila* embryo [251, 252].

The main difficulty we faced with this system was the sensitivity of the extract and flow inside the chambers. Careful preparation and handling of the extract with reduced internal flow allowed us to observe cell-like division in these chambers. As explained in the previous section, using a chip soaked overnight in Milli-Q water, sealing the filled chamber inlets and outlets with vacuum grease, and placing drops of water on the side of the chip during the measurement helped to reduce the flow inside the chamber. Due to the time limitation, we did not explore this system in more detail. This can be done in the future to unravel the effect of chamber geometry in cell-like division using this in vitro system. The identification and tracking of the daughter cell can be improved by fluorescent labelling of the nuclear envelope and chromosome.

5.3.2.3. Conclusion

In conclusion, we successfully observed cell-like division using cycling extract in microfluidic chambers having different geometries. The initial pattern formation was influenced by the chamber geometry and sperm head distribution. This formed structures underwent multiple cell-like divisions and all the chambers became covered with the daughter cells after some divisions. We did not track cell division due to the contrast issue, which can be improved in the future by fluorescence labelling of the chromosome and nuclear envelope.

5.4. Summary of the chapter

This chapter summarizes the different investigations to study structure and pattern formation conducted using the *Xenopus* egg extracts focussing mainly on the experimental methods. In summary, we successfully establish the protocols for preparing CSF, interphase and cycling extracts. In the first section, we realized the successful formation of the mitotic spindles and asters in fixed samples and microfluidic droplets using the CSF extract. However, the effect of MSBs on the mitotic spindle was not realized due to the complexity of the system. In the subsequent section, we successfully observed cell-like compartmentalization in large chambers and in microfluidic chambers with different geometries. Here we realized that increasing taxol concentration reduces the protocell length scale with similar geometrical features. The protocell size increase over time was observed, and its growth rate decreased with increasing taxol concentration. The chamber geometry was also found to influence the protocell pattern. Finally, we observed cell-like division in the large chamber and in microfluidic chambers with different geometries. However, more experiments were needed to comprehend chamber geometry's effect on cell-like division. The established methods with the *Xenopus* extract can be a valuable tool to study different aspects of cellular organization and division in greater depth in a controlled manner.

6 Perspectives

To summarise the result achieved with this thesis: several new experimental and analysis methods were developed to understand the effects of enhanced mixing, confinement and chemical perturbation on diffusion and pattern formation in biomimetic and biofluid systems. For this purpose, several experimental protocols were developed, such as magnetic stir bar (MSBs) synthesis and characterization, *Xenopus* extract (CSF, interphase and cycling) preparation, microfluidic methods for droplet and chamber production, and sample preparation strategies. Furthermore, magnetic stirrer and controllers were developed for addressing MSBs compatible with real-time confocal fluorescence microscopy.

Using the improved synthesis strategies, slender rod-like ferrimagnetic MSBs were developed with a mean length of around 4 μm and achieved synchronous rotation inside droplets using magnetic stirrers. The stirrer's real-time imaging was achieved using a custom-made Helmholtz coil-based stirrer and custom controllers compatible with an inverted confocal microscope. However, the MSBs were tilted at a higher stirring frequency due to the balancing of magnetic and friction-induced torques. The feasibility of the MSBs agitation/stirring method to enhance mixing was analyzed using an aqueous droplet containing polystyrene beads and MSBs. The agitation of these MSBs inside aqueous droplets revealed an enhanced diffusion of the polystyrene beads. In addition, a clear signature of the MSBs stirring was observed in the MSD, power spectral density and VACF function obtained from the SPT trajectories of the polystyrene beads. Due to the tilting of the MSBs at a higher stirring frequency (above 1 Hz), a non-monotonous progression with a maximum of two-fold enhancement of the transport coefficient with a normal diffusion characteristics was observed using the current stirring system.

Furthermore, we successfully encapsulated MSBs into *Xenopus* extract droplets using microfluidics methods. Interestingly, the MSBs agitation did not affect the formation of microtubules inside these droplets and was able to observe the signature of stirring. In addition, the MSBs incorporation did not affect the protocell pattern formation in the interphase extract. The added MSBs were accumulated and trapped at the center of the protocell and only seemed to perform rotation before protocell formation and after protocell disintegration. However, the effect of MSBs agitation in

mitotic spindle formation was unable to achieve. Analysis of stirring signatures can be improved by increasing the temporal resolution, and stirring can be enhanced by decorrelating the stirrer with a higher magnetic field. With these improvements, MSBs can be used as a versatile tool to enhance mixing and add controlled noise inside biomimetic and artificial fluids.

Different structures and pattern formations like mitotic spindle formation, cell-like protocell formation and cell-like division were achieved in vitro using *Xenopus* egg extracts. The pattern formation achieved using interphase extract was similar to the aster arrays in *Phallusia* oocytes [227] and *Drosophila* syncytial blastoderm [231]. A detailed analysis of the pattern formation using Voronoi tesselation revealed that the protocell length scale reduced with increasing the concentration of microtubule-stabilizing drug taxol, but the geometrical features remained invariant. The fluorescence confocal images with labelled tubulin substantiate this analysis. Moreover, the protocell size increased over time with merging and its growth rate reduced with increasing taxol concentration. Multiple cell-like division cycles were observed with cycling extract, which always occurred wave-like, with division first starting at the border and progressing towards the center. This cell-like division resembled the embryo of *Drosophila* [249, 250].

The structure and pattern formation were also studied under geometric constraints. The mitotic spindle or aster formations were achieved in CSF extracts encapsulated in water in oil droplets. In addition, pattern formation with interphase extract and cell-like division with cycling extracts were obtained in microfluidic chambers with different geometries. The taxol addition to interphase extract resulted in smaller protocells formation here as well and the pattern arrangement adapted to the chamber's geometry. The preliminary analysis showed that the cell-like division also had an influence on the chamber geometry for the initial arrangement. The smaller protocells formed later were evenly distributed in all the chambers. The pattern formed with interphase and cycling extracts in these chambers resembled the different stages of embryonic division in *Caenorhabditis elegans* [239, 240] and *Drosophila melanogaster* [241, 252]. A detailed analysis of pattern formation in these confined microfluidic chambers still needs to be done. Due to the chamber's resemblence to embryo shape and size, this can be used as a simple in vitro system to study the effect of embryo shape on cellular organization and embryonic division. Tracking cell division was difficult in our case due to low contrast in our brightfield images, which can be improved by fluorescence labelling of chromosome and nuclear envelope.

Overall this thesis provides valuable insight into the methods to achieve structure and pattern formation in biofluid systems. It also provides the methods that can be used to enhance mixing and modulate patterns in this system. The methods developed in this thesis can be used as a valuable tool to understand different factors affecting self-organization and division in a controlled manner. Moreover, it is easier to manipulate this system through mechanical and chemical interventions than a normal cell or an embryo.

A

Appendix

A.1. *Xenopus laevis* extract preparation

This section goes into great detail about the extract preparation protocols. Materials and buffers information for each extract protocol is also provided. The steps and materials/buffers that are common to the different extract preparation protocols are discussed together, while the rest are addressed separately. The matter covered in this section is based on previous works [12, 23, 60, 87, 134, 135, 138–140] and our own experience.

A.1.1. Materials and buffers

The following are the materials and buffers common to all three extract preparation protocols and extract experiments.

Common materials and buffers

- Pregnant mare serum gonadotropin (Intergonan, 240 U/mL)
- Human chorionic gonadotropin (Ovogest, 1000 U/mL)
- Cytochalasin B (Calbiochem, 10 mg/mL in DMSO)
- Rhodamine labelled tubulin from bovine brain (Cytoskeleton Inc.)
- Guanosine 5'-triphosphate sodium salt hydrate (GTP; Sigma-Aldrich, 100 mM in Milli-Q water)
- Sperm heads (14,400/μL stock), stored in small aliquotes at -80°C.
- 4 L plastic containers with tight-fitting lids (hole-punched for air exchange)
- 200 mL glass beaker

- Pasteur pipettes
- 2 mL syringes with 18-gauge needles
- Open-top polyclear centrifuge tube (Seton, 4/6.5 mL)
- Beckman Coulter JS-13.1 swinging bucket aluminium rotor
- SecureSeal ^{TM} imaging spacers (SS8X9, 8-9 mm Diameter and 120 μm height)
- Aquapel® water repellent glass treatment pack
- Microscope slides (Corning, plain, 25 × 75 mm, thickness 0.96-1.06 mm)
- Coverslips (Menzel Gläser, 24 × 60 mm, #1.5 thickness)
- General tubulin buffer: 80 mM PIPES pH 6.9, 2 mM $MgCl_2$, 0.5 mM EGTA. Stored at -80°C.
- 25x Marc's Modified Ringer's (MMR): 2.5 M NaCl, 50 mM KCl, 25 mM $MgCl_2$, 50 mM $CaCl_2$, 2.5 mM EDTA, 125 mM HEPES, pH 7.8 with NaOH. Stored at room temperature.

  Note: Different concentrations of MMR are made by diluting it with Milli-Q water.
- 20x extract buffer (XB) salts: 2 M KCl, 2 mM $CaCl_2$, 20 mM $MgCl_2$. Autoclaved and stored at 4°C.
- Sperm dilution buffer: 1 mM $MgCl_2$, 100 mM KCl, 150 mM Sucrose, 5 mM HEPES (pH 7.7, KOH), adjust final voulme to 15 mL using Milli-Q water. Stored in small aliquotes at -80°C.

A.1.1.1. Materials and buffers used mainly for CSF extract

The materials and buffers are only needed for the preparation of CSF extract and its experiments.

- Cytochalasin D (Calbiochem, 10 mg/mL stock in DMSO)
- Leupeptin (Sigma Aldrich, 10 mg/mL stock in DMSO)
- Pepstatin (Sigma Aldrich, 10 mg/mL stock in DMSO)
- Chymostatin (Sigma Aldrich, 10 mg/mL stock in DMSO)
- Extract buffer (CSF-XB): 100 mM KCl, 0.1 mM $CaCl_2$, 2 mM $MgCl_2$, 10 mM HEPES (pH 7.7, KOH), 5 mM EGTA (pH 8.0, KOH), 50 mM sucrose. Adjust pH to 7.7 using KOH. Prepare fresh and store at 16°C. For 1 L CSF-XB, add 50 mL 20x XB salts, 2 mL 1M $MgCl_2$, 10 mL 1 M HEPES (pH 7.7, KOH), 10 mL 0.5 M EGTA (pH 8.0, KOH), 17.15 g sucrose, and fill to 1 L with Milli-Q water. Adjust pH to 7.7 using KOH.
- Dejellying solution: 2.0% (w/v) L-Cysteine (free base; Sigma Aldrich) in 0.5x XB salts, pH 7.8 with KOH.

- 50x ATP regeneration mix: 190 mM creatine phosphate (Sigma-Aldrich), 25 mM ATP (Sigma Aldrich), 25 mM MgCl2, 2.5 mM EGTA, pH 7.7 with KOH. Stored in aliquots at -20°C for future use.
- 25x Ca^{2+}: 15 mM $CaCl_2$ in 15 mL sperm dilution buffer. Stored in small aliquotes at -80°C.
- Spindle-Fix: 48% Glycerol, 11% Formaldehyde, 1x MMR, 1 μg/mL Hoechst 33342 in small aliquotes at -80°C.

A.1.1.2. Materials and buffers used mainly for interphase extract

The materials and buffers are only needed for the preparation of interphase extract and its experiments.

- Aprotinin (Roche Diagnostics GmbH, 5 mg/mL in Milli-Q water)
- Leupeptin (Sigma Aldrich, 10 mg/mL in Milli-Q water)
- Cycloheximide (Calbiochem, 10 mg/mL in Milli-Q water)
- Taxol (Sigma Aldrich, 10 mg/mL stock solution in DMSO)
- 1,4-Dithiothreitol (DTT; Roche Diagnostics, 154 mg per liter of ELB)
- 1 μm polystyrene beads (Micromod Partikeltechnologie, micromer, COOH surface, product code: 01-02-103). Stock solution prepared by an aqueous 10x dilution of the pellet obtained by centrifugation.
- Fluorescein isothiocyanate-dextran (FITC-dextran 10kDa; Sigma Adrich). Stock solution: 10% (by weight) dissolved in Milli-Q water.
- Fluorinated ethylene propylene adhesive film (FEP; thickness 50 μm, Holscot Europe)
- SecureSeal™ imaging spacers (Grace Bio-Labs, SS8X9, 8-9 mm diameter, 120 μm height)
- Dejellying solution: 2.0% (w/v) L-Cysteine (free base; Sigma Aldrich) in Milli-Q water, pH 7.8 with KOH.
- Egg Lysis Buffer (ELB): 250 mM sucrose, 2.5 mM MgCl2, 50 mM KCl, 10 mM HEPES, pH 7.7 with KOH, 1 mM DDT.

  Note: DDT was added to the buffer just before the extract preparation.

A.1.1.3. Materials and buffers used mainly for cycling extract

The materials and buffers are only needed for the preparation of cycling extract and its experiments.

- Leupeptin (Sigma Aldrich, 10 mg/mL stock in DMSO)
- Pepstatin (Sigma Aldrich, 10 mg/mL stock in DMSO)

- Chymostatin (Sigma Aldrich, 10 mg/mL stock in DMSO)
- Calcium ionophore A23187 (Sigma Aldrich, 10 mg/mL stock in DMSO)
- 20x Egg laying buffer: 2M NaCl, 40 mM KCl, 20 mM $MgSO_4$, 50 mM $CaCl_2$, 10 mM HEPES (pH 7.7 with KOH), 2 mM EDTA.
- Dejellying solution: 20% (w/v) L-Cysteine (free base; Sigma Aldrich) in Milli-Q water with 1x XB salts, pH 7.8 with KOH.
- Calcium ionophore solution: 15 μL calcium ionophore A23187 stock solution to 300 mL of 0.2x MMR. prepare fresh and use immediately.
- 1x Extract buffer (XB): 50 mL 20x XB salts, 17.11g Sucrose, 10 mL HEPES (pH 7.7 KOH). Combine and bring to 1 L using Milli-Q water and adjust pH to 7.7 with KOH. Prepare fresh and stored at 16°C.
- XB^+: Add 1:1000 of LPC (leupeptin, pepstatin, and chymostatin) protease inhibitors to 1x XB buffer. Prepare fresh and use immediately.
- XB^{++}: Add 1:100 Cytochalasin B to XB^+ buffer. Prepare fresh and use immediately.

A.1.2. Extract preparation protocol

The general steps of extract preparation are discussed together, and the extract-specific steps are explained separately. The common steps are given below.

1. Three days before the planned experiments, subcutaneously injected pregnant mare serum gonadotropin (PMSG, 100 μL) into the female frogs and kept them together in a separate container filled with water. We also didn't feed the frogs until experiment day (max. 2 days) to avoid fecal contamination.
2. Primed frogs were injected subcutaneously with 600-800 μL of human chorionic gonadotropin (HCG, adjust volume to match frog size) 16-17 h before the scheduled experimental day. Then keep them in separate plastic containers filled with 1.5 L of 1x MMR buffer (CSF and interphase extract) or egg laying buffer (cycling extract) at 18°C to lay eggs.

   Note: In some extract preparation protocols, we only performed a single HCG injection to induce egg laying.
3. On the day of extract preparation, the frogs were separated from the eggs and placed in a container filled with deionized water. Frogs were returned to the colony at the end of the day. To get fresh eggs, massage the frog's back with the leg pushed forward while holding it in hand.

4. Cleaning the eggs: Transfer the eggs to a 200 mL glass beaker and pour away any excess solution to remove urine, feces, or other particulate matter. If the eggs are filthy, wash them once with the 1x MMR.

5. Remove bad eggs: Good eggs have clear delineated animal (dark) and vegetal (light) poles. Clutches of activated or lysed eggs (white and puffy appearance) or stringy should not be used as they can affect extract quality. The bad eggs were removed using a Pasteur pipette. Use a new Pasteur pipette once an egg breaks inside it.

6. Dejelly eggs: Pour as much as possible of the 1x MMR solution from the beaker and add the dejellying solution (different ones, check section A.1.1) to each of the beakers, each containing eggs from separate frogs, and swirl them frequently. If there is some dejellying solution left, remove some of it from the beaker and replace it with the remaining one. It is critical to have the eggs fully dejellied before moving to the CSF-XB/MMR washes, as seen by the disappearance of space between the eggs and the dissolution of jelly coats in the solution. Dejellying typically takes 4-6 min, depending on the eggs.

   Note: It is critical not to exceed 6 min since eggs left in the dejellying solution (cysteine) for too long will lyse. As the eggs dejelly, they become closely packed down. Next, let the eggs sediment, remove as much as possible of the dejellying solution, and start washing with CSF-XB/MMR washes. Pour the buffer down the side of the beaker to prevent harming the eggs, which are fragile once dejellied.

A.1.2.1. CSF extract

7. Rinse the dejellied eggs four times with CSF-XB. Stir each time briefly and let the eggs settle down. Remove any excess CSF-XB before the next addition. Rush through these washes to get the eggs into the centrifugation step.

8. Using an inverted Pasteur pipette (the bulb at the pointed end so that the eggs stay intact), transfer the eggs to an open-top Seton centrifuge tube containing 500 μL of CSF-XB with 5 μL of cytochalasin D.

9. To pack the eggs, centrifuge for 2 min at 18°C. Start with 200 g and increase to 600 g after 1 min. Remove the excess buffer from the top of the packed eggs with a pipette. Remove as much buffer as possible to ensure a concentrated egg extract. Sacrifice eggs to achieve this.

10. Crush the eggs in a Beckmann Coulter JS-13.1 swing rotor at 18°C for 10 min at 13,000 g. The crushed eggs are separated into three layers: a yellow lipid layer on top, a crude CSF extract in the middle, and a dark pellet containing pigment granules on the bottom.

11. Remove the crude CSF extract by piercing the side of the centrifuge tube $\sim$ 2-3 mm above the dark bottom layer with an 18-gauge needle attached to a 2-mL syringe. The needle is inserted upward at a 45-degree angle and pushed to the opposite side of the tube. The opening of the

needle should be facing up. Observe from this opposite side and aspirate the extract until the yellow yolk enters the needle. Then rotate the needle to get as much extract as possible. Stop when the remaining cytoplasmic layer in the tube is no less than 2-3 mm deep or cannot be harvested without significant contamination with lipids or mitochondria. Remove the needle and carefully eject the extract into an Eppendorf tube.

Note: While slight contamination of the top layer (yellow yolk) is acceptable, avoid contamination of the bottom layer as it contains mitochondria that cause apoptosis.

12. Determine the volume of the extract, then add 10 μg/mL leupeptin, 10 μg/mL pepstatin, 10 μg/mL chymostatin, 10 μg/mL cytochalasin D, and 1:50 of ATP regeneration mix directly to the extract. For optimal timing, mix these compounds together in a single solution before adding the required volume to the extract. Mix these by carefully inverting the Eppendorf tube and keep the Eppendorf tube immediately on ice.

A.1.2.2. Interphase extract

7. Rinse the dejellied eggs five times with 0.5x MMR. Stir each time briefly and let the eggs settle down. Remove any excess MMR before the next addition. Rush through these washes to get the eggs into egg lysis buffer (ELB).
8. Wash the eggs three times with ELB containing dithiothreitol (DTT) by swirling them in the buffer and then pour off the buffer. Remove any bad eggs (eggs are more stable in the ELB, so up to 10 min are available to remove bad eggs).
9. Using an inverted Pasteur pipette (the bulb at the pointed end so that the eggs are not broken), transfer the eggs to an open-top Seton centrifuge tube containing 500 μL of ELB with 5 μL of cytochalasin B.
10. To pack the eggs, centrifuge for 2 min at 18°C. Start with 200 g and increase to 600 g after 1 min. Remove the excess buffer from the top of the packed eggs with a pipette. Removing as much buffer as possible is critical to ensure a concentrated egg extract. Sacrifice eggs to achieve this.
11. Crush the eggs in a Beckmann Coulter JS-13.1 swing rotor at 18°C for 10 min at 13,000 g. The crushed eggs are separated into three layers: a yellow lipid layer on top, a crude interphase extract in the middle, and a dark pellet containing pigment granules on the bottom.
12. Remove the crude extract by piercing the side of the centrifuge tube $\sim$ 2-3 mm above the dark bottom layer with an 18-gauge needle attached to a 2-mL syringe. The needle is inserted upward at a 45-degree angle and pushed to the opposite side of the tube. The opening of the needle should be facing up. Observe from this opposite side and aspirate the extract until the yellow yolk enters the needle. Then rotate the needle to get as much extract as possible. Stop when the remaining cytoplasmic layer in the tube is no less than 2-3 mm deep or cannot be

harvested without significant contamination with lipids or mitochondria. Remove the needle and carefully eject the extract into an Eppendorf tube.

Note: While slight contamination of the top layer (yellow yolk) is acceptable, avoid contamination of the bottom layer as it contains mitochondria that cause apoptosis.

13. Determine the volume of the extract, then add 5 μg/mL aprotinin, 5 μg/mL leupeptin, 5 μg/mL cytochalasin B, and 50 μg/mL of cycloheximide directly to the extract. For optimal timing, mix these compounds into a single solution before adding the required volume to the extract. Mix by carefully inverting the Eppendorf tube, and put immediately on ice.

A.1.2.3. Cycling extract

7. Gently rinses the dejellied eggs five times with 0.2x MMR. Stir each time briefly and let the eggs settle down. Decant as much of the MMR solution as possible between the washes. Rush through these washes to get eggs to the subsequent activation step.

8. Activate eggs: Add calcium ionophore solution to eggs. Incubate for precisely 2 min with occasional swirling. A contraction of the animal pole pigment is often visible towards the end of 2 min. During this period, use a transfer pipette to remove any bad eggs. We often noticed a colour change in the eggs at the end of this activation step.
Note: Without agitation, the eggs may stick to each other and the bottom of the glass beaker, but this will not noticeably impact extract quality. Keep only the exact 2 min with calcium ionophore (use a stopwatch). Prolonged exposure to calcium ionophores will reduce extract quality.

9. Wash: Decant the calcium ionophore solution and wash eggs immediately four times with a total of 1 L 1x XB.

   Note: Most often, most eggs rotate with their animal poles up. Nevertheless, extracts from batches that do not show uniform rotation often still execute the cell cycle.

10. Wash: The eggs were washed twice in 24 mL of 1x XB^{+}. We skipped this washing step to reduce the consumption of LPC and cytochalasin B.

11. Using an inverted Pasteur pipette (the bulb at the pointed end so that the eggs are not broken), transfer the eggs to an open-top Seton centrifuge tube containing 1 mL of XB^{++}. Minimize buffer transfer as little as possible to avoid diluting cytochalasin B.

12. Packing of eggs: 15 min after the start of calcium activation (step 8), use a Beckmann Coulter JS-13.1 swing rotor to centrifuge the eggs for 60 s at 157 g and then for 30 s at 600 g at 4°C. To obtain a concentrated extract, remove as much buffer as possible.

13. Place the Seton centrifuge tube on ice for 15 min to rest.

14. Crush the eggs by centrifugation at 16,000 g in Beckmann Coulter JS-13.1 swing rotor for 10 min at 4°C.

15. Clean and dry the outside of the Seton centrifuge tube with 70% ethanol.

16. Remove the crude extract by piercing the side of the ultracentrifuge tube using an 18-gauge needle attached to a 5 mL syringe. The entry point should be toward the bottom of the straw-coloured cytosolic layer (the cytosolic layer is between the bottom darker yolk layer and the top lipid layer). Slowly withdraw crude extract to avoid mixing other layers.

17. Expel extract into a 1.5 mL Eppendorf tube and add leupeptin, pepstatin, chymostatin, and cytochalasin B at a ratio of 1:1000 (10 μg/mL final each). For optimal timing, mix these compounds into a single solution before adding the required volume to the extract. Mix by carefully inverting the Eppendorf tube, and put immediately on ice.

18. Centrifuge this extract at 16,000 g in a tabletop centrifuge for 6 min at 4°C.

19. Remove the top residual lipid layer by aspiration with a 30-gauge needle connected to the vacuum pump.

    Note: Since we don't have a vacuum-connected setup, we used a 2 mL syringe connected to a 30-gauge needle. We need to be careful during this step.

20. Trim a P-1000 pipette tip with scissors, and transfer the extract to a fresh Eppendorf tube, leaving behind the darkly pigmented portion at the bottom.

    Note: Depending on the purpose of the extracts may be supplemented with an ATP regeneration/energy mix. 30 μL of the energy mix was added to 970 μL of extract. Chang and Ferrel [140] found that this energy mix sometimes prevents extracts from cycling, so it was not used unless attempting to do a very long (> 8 cycles) experiment.

A.2. Aggregated MSBs

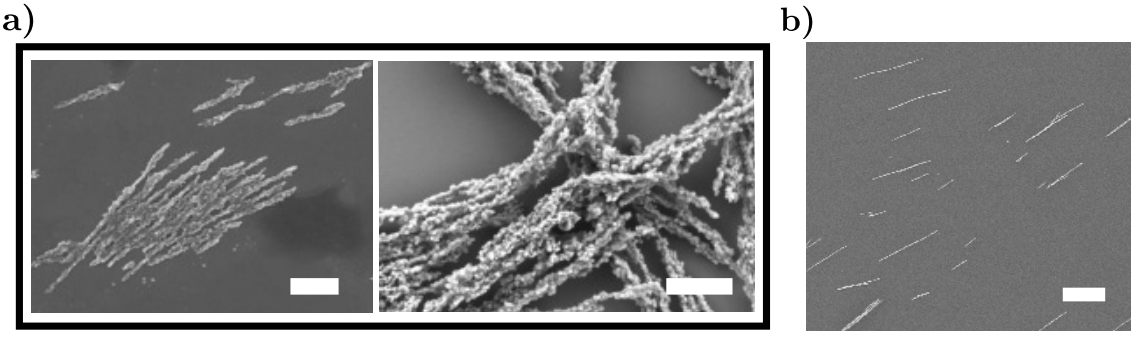

Figure A.1.: Aggregated MSBs and also an overview of aligned MSBs: (a) SEM images of aggregated MSBs synthesized using the old method by keeping the magnet at the bottom of the vial. The MSBs are fused in the silica matrix to form this aggregated structure. The scale bar is 2 μm. **(b)** SEM image with the overview of aligned MSBs. The SEM sample was dried on top of the VWR stirrer during the sample preparation to achieve this arrangement. MSBs used here are synthesized using the refined method with the magnet on the side of the vial using a custom-made holder. Scale bar is 15 μm.

A.3. Magnetic field measurement

The magnetic field of the stirrers was measured using the Hall effect sensor (SS495A1, see Figure A.2b). The sensor has three legs, the legs on the side are for the 5 V power supply (positive and Ground), and the center one is for the voltage output. We used an Arduino Mega2560 to power the sensor and to get the voltage output. According to the transfer characteristics, the voltage output is proportional to the magnetic field (see Figure A.2c) [254], and using a custom MATLAB script, obtained the magnetic field produced by the corresponding stirrer. The measurement setup arrangement for the 2mag stirrer is given in Figure A.2a (a similar arrangement was made for other stirrers too). We utilized a micromanager program to position the sensor using a motorized XYZ-stage and obtain the Arduino's voltage output. All the magnetic field values for stirrers mentioned in the thesis were obtained through this setup.

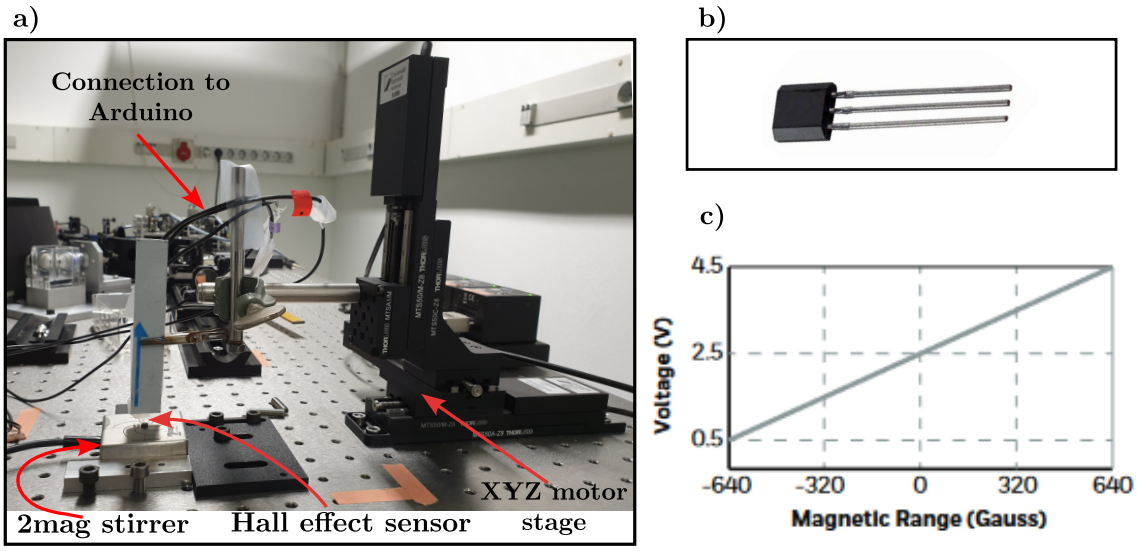

Figure A.2.: Magnetic field measurement: (a) The magnetic field measurement setup: The position of the Hall effect sensor on the stirrer was controlled using a motorized stage. Here measuring the magnetic field of a 2mag stirrer, the procedure is similar to other realizations. The corresponding field intensity was obtained using a connected Arduino with the help of micromanager software. **(b)** The Hall effect sensor (SS495A1). **(c)** Transfer characteristics of the Hall effect sensor [254], which was used to obtain the magnetic field with the help of voltage measurement through Arduino.

A.4. Evolution history of Helmholtz coil based magnetic stirrer

We began with the arrangement of four inductors on an aluminum holder and ended up on machine-winded coils held using a custom-made holder. The intermediate designs proved our idea was working and enabled us to observe the rotation of MSBs even with brightfield microscopy. Figure A.3 shows the evolution history of the stirrer design with duly marked components.

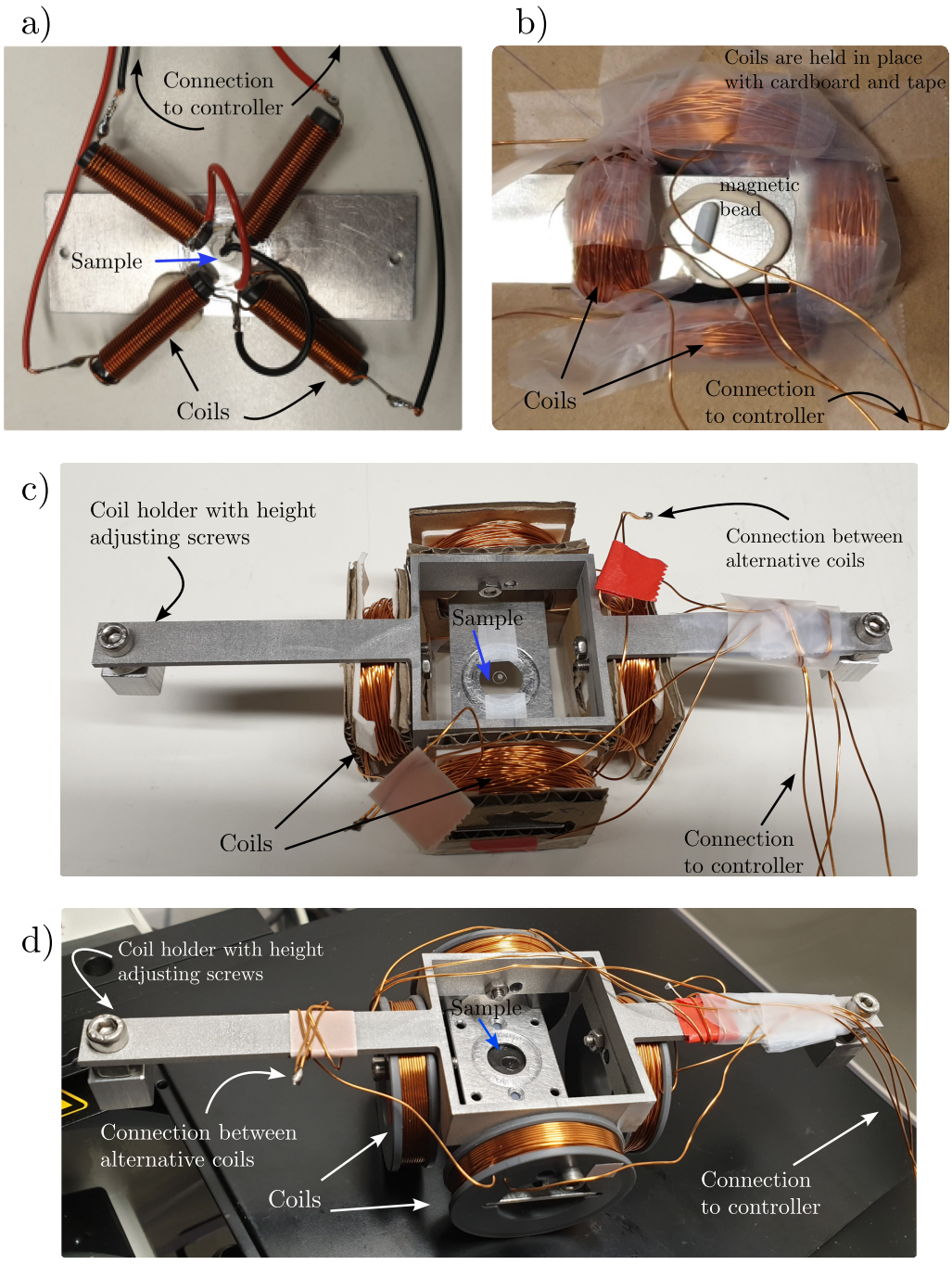

Figure A.3.: Evolution of Helmholtz coil based magnetic stirring device: All devices consist of four coils. The alternative coils are connected to become a pair. An alternating current with a 90° phase difference is given to the coil pairs to induce a rotating magnetic field. **(a)** The magnetic stirring device is based on four small inductors glued into an aluminum holder. **(b)** It consists of four coils, which are hand winded and aligned with the help of cardboard and tapes (it was to check the working principle). **(c)** It consists of four hand-winded coils aligned with a custom-made coil holder. Height can be adjusted using the screws at both ends while keeping it on the microscope. The coil was winded on a piece of centrifugation tube, and cardboard pieces were glued to the sides to stabilize the coil winding. Samples can keep in the center for microscopic observation. **(d)** The four coils were winded using the winding machine on 3D-printed coil casings. Coils were aligned using the custom aluminum holder, and samples can be placed on the grove made on one pair of 3D-printed coil casings used for coil winding.

A.5. Arduino IDE code for the Arduino controller

```
1
int pwm_a = 3;  // PWM control for the motor outputs 1 and 2
3
int pwm_b = 9;  // PWM control for the motor outputs 3 and 4
5
int dir_a = 2;  // direction control for the motor outputs 1 and 2
7
int dir_b = 8;  // direction control for the motor outputs 3 and 4
9
int i;  // Loop variable
11
double frq=0.1; // frequency of rotation, modify it for different frequency
13
double T=1/(frq); // Period
15
int n=500;
17
double dt=T/n*1e3;
19
double amp_a;  // Signal amplitude in loop
21
double amp_b;  // Signal amplitude in loop
23
double phi;
25
void setup()
27
{
29
  TCCR1B = TCCR1B & B11111000 | B00000001;  // set timer 1 divisor to 1 for
     PWM frequency of 31372.55 Hz, pin 9 and 10
31
  TCCR2B = TCCR2B & B11111000 | B00000001;  // for PWM frequency of
    31372.55 Hz, pin 3
33
  pinMode(pwm_a, OUTPUT);   // set control pins to be outputs
35
  pinMode(pwm_b, OUTPUT);
37
  pinMode(dir_a, OUTPUT);
39
  pinMode(dir_b, OUTPUT);
41
  analogWrite(pwm_a, 100);  // set both motors to run at (100/255 = 39)%
    duty cycle (slow)
43
  analogWrite(pwm_b, 100);
```

```
45
}
47 void loop()

49 {

51 for(i =0; i < n; i += 1)

53   {

55     phi=2.0*3.14156*i/(n-1);

57     amp_a=255*cos(phi);

59     if (amp_a>0) {

61      digitalWrite(dir_a, HIGH);

63     }

65     else {

67      digitalWrite(dir_a, LOW);

69     }
       amp_b=255*sin(phi);
71
       if (amp_b>0) {
73
        digitalWrite(dir_b, HIGH);
75
       }
77
       else {
79
        digitalWrite(dir_b, LOW);
81
       }
83
       analogWrite(pwm_a, floor(abs(amp_a)));
85
       analogWrite(pwm_b, floor(abs(amp_b)));
87
       delay(dt);
89   }

91 }
```

A.6. Stirring mitotic spindle in droplets

Since we didn't observe any significant effects of MSBs stirring in droplets prepared by the microfluidic and pipetting methods, we prepared a large droplet with the spindle assembly reaction containing MSBs. The sample was prepared by pipetting 1 μL of this extract onto the bottom of a glass-bottom IBIDI chip containing 200 μL of Squalene oil. We observed some mitotic spindles in the vicinity of MSBs during the fluorescence screening. So intrigued with the idea of studying the effect of MSBs stirring on these spindles, a rotating magnetic field was applied.

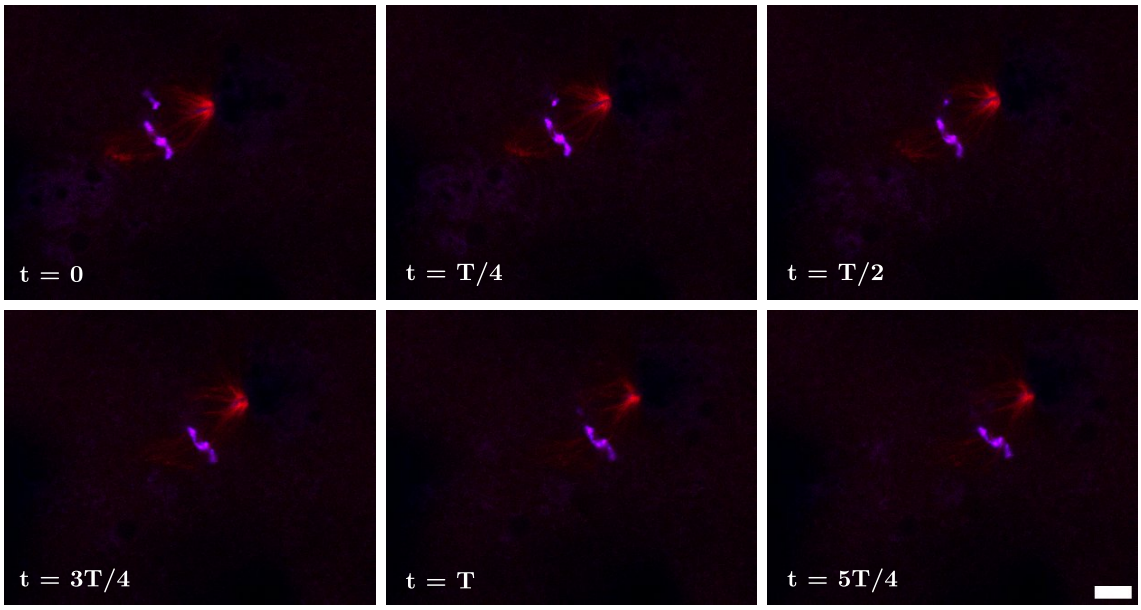

Figure A.4.: Mitotic spindle stirring in droplets: Representative snapshot of the mitotic spindle inside a large droplet deforming when stirred with MSB at 0.5 Hz. The microtubules and chromosomes are colour-coded red and blue, respectively, and the MSBs are some of the dark pixels. The scale bar for is 20 μm.

The global motion of this droplet was observed while it was addressed with a rotating magnetic field frequency (f) of 0.5 Hz. Some MSBs in the vicinity (which may be attached to microtubules) resulted in the deformation of the mitotic spindle. Since MSBs are not labelled made challenging to observe them in fluorescence imaging. But can be distinguished from the agitation while addressing with a rotating magnetic field (seen as some dark pixel). The deformation observed on a mitotic spindle is shown in Figure A.4. In this case, some MSBs felt attached to the mitotic spindle and significantly affected the deformation. In conclusion, we can deform the mitotic spindle inside a droplet in a controlled manner.

A.7. Additional information and figures for protocell formation in chambers

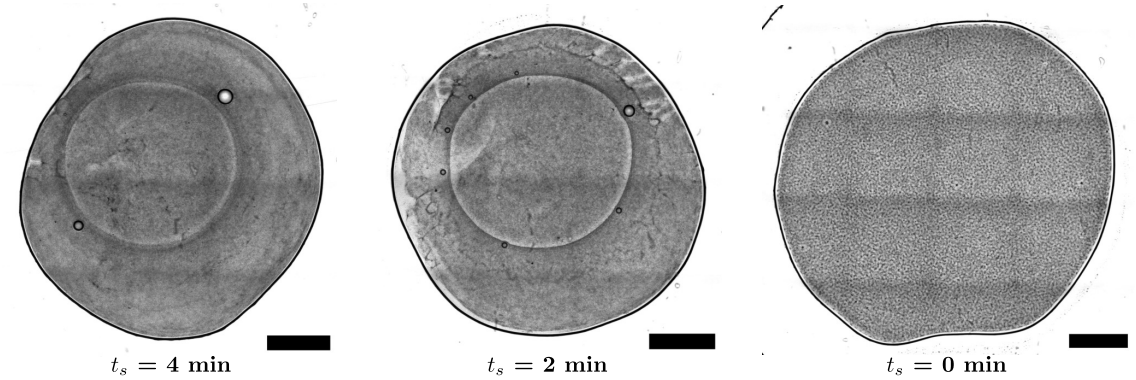

Figure A.5.: Effect of chamber sealing time: Representative images of the droplets at different chamber sealing times (t_s) as indicated in the figure. The longer time interval between pipetting the extract droplet into the chamber and sealing it resulted in forming a ring-shaped pattern. Immediate sealing of the chamber eliminates this ring-like pattern. The scale bar of the images is 1 mm.

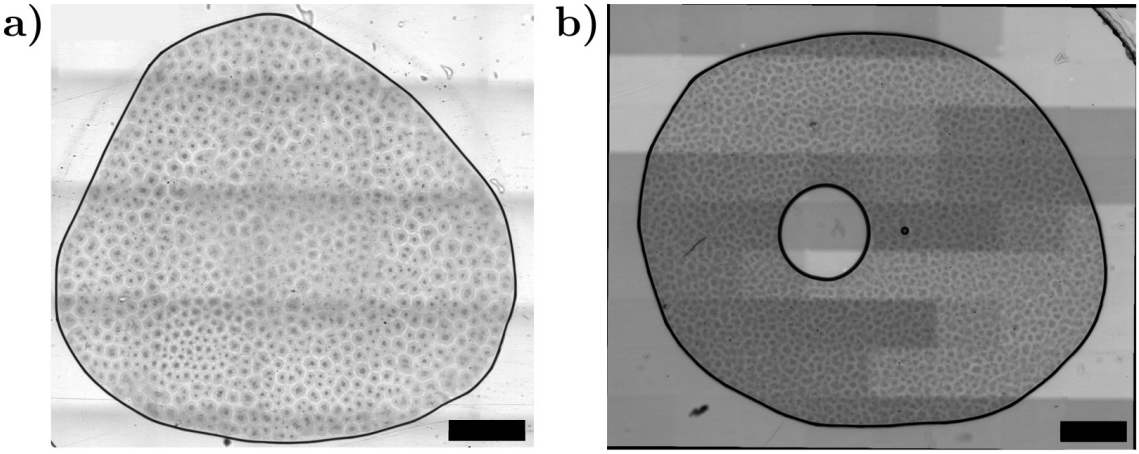

Figure A.6.: The issue with mixing and intensity fluctuation: **(a)** Representative image of a droplet containing protocells of different sizes results from the extract's inhomogeneous mixing. The inhomogeneous mixing of the different added components leads to this kind of protocell pattern formation. **(b)** Representative image of a droplet with a bubble in the center and contrast variation between the merged tiles due to transmission light intensity fluctuation while imaging. The scale bar of the images is 1 mm.

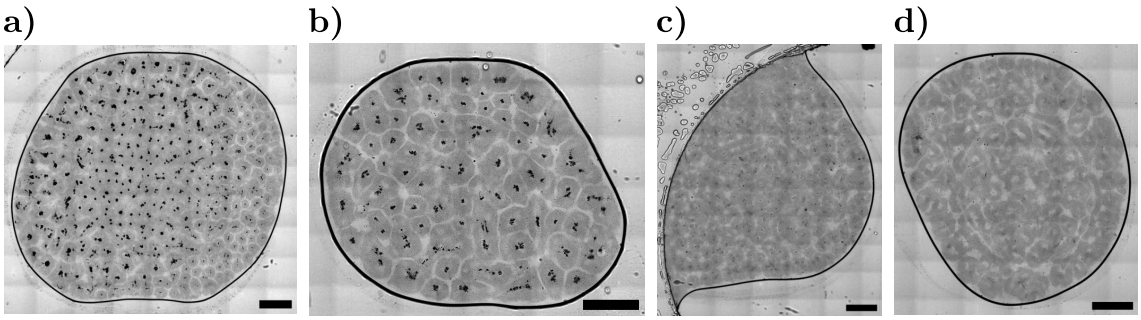

Figure A.7.: Optimizing the concentration of 1 μm polystyrene beads (beads) in the extract: Representative images of droplets with 1% volume of different dilutions of the centrifuged pellet of 5 mg/mL beads (bulk) added to the extract; **(a)** bulk, **(b)** bulk/10, **(c)** bulk/100, and **(d)** no beads. We chose the concentration in **(b)** for all our experiments as it is not too concentrated, provided a good contrast for image analysis, and did not alter the protocell formation. The scale bar of the images is 1 mm.

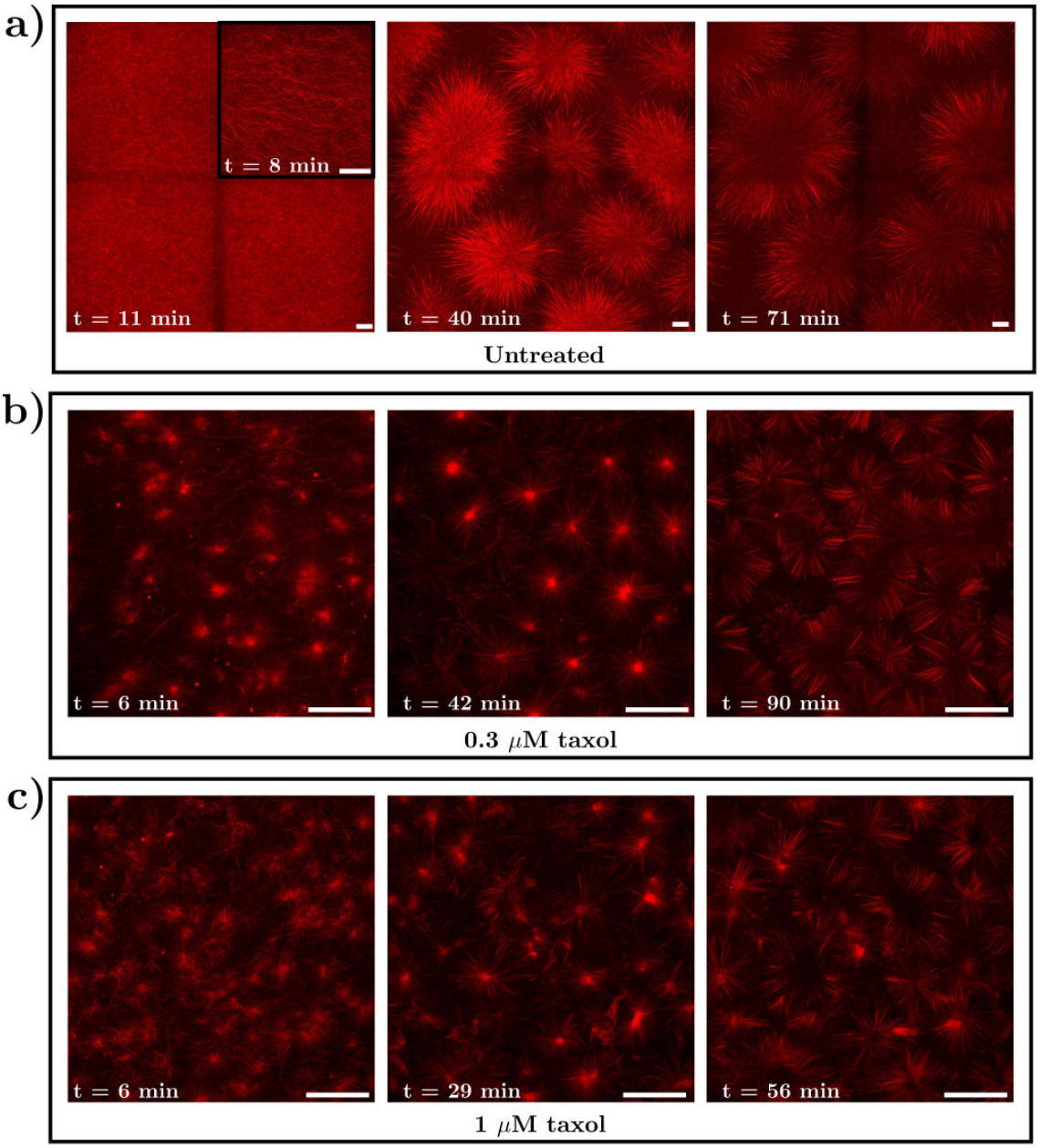

Figure A.8.: Representative confocal fluorescence images of microtubules in protocells at different times of pattern evolution and taxol concentrations: The taxol concentration and the time (after chamber sealing) of the images are indicated in the figure and the scale bar is 50 μm. The radial microtubule array is visible in all the concentrations with varying length scales. **(a)** At the beginning (t = 11 min), the microtubules appear long and homogeneously distributed; see the figure inset at t = 8 min from another experiment for a better overview. These microtubules focus later (at t = 40 min) into a flower-like structure (radially arranged microtubules), forming the protocells. At 71 min, protocells still appear as radial arrays of microtubules. The protocell centers appear slightly darker as they are crowded with organelles and minute amounts of polystyrene beads transported inwards by the radial microtubule array. In **(b and c)**, focussed microtubule centers, which acts as seeds for protocell formation, are visible at the first time point itself (t = 6 min). Compared to the untreated case, the microtubule appears shorter and radial arrangements are also visible. Later (t = 42 and 29 min, respectively), these microtubule organizations resulted in smaller protocells. Similar to the untreated case, slightly darker centers with microtubules radially arranged in the periphery are visible subsequently (t = 90 and 56 min, respectively). The microtubule structure in 1 μM is less tidy than the 0.3 μM taxol, but more focused centers are visible at the beginning. The merging of the nearby centers resulted in similarly large compartments; earlier points for 1 μM were omitted due to the untidiness of the images.

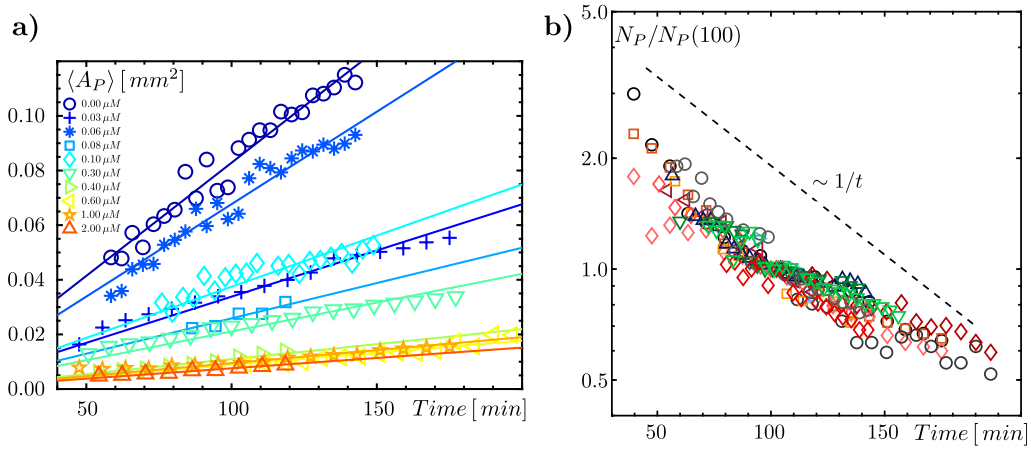

Figure A.9.: Time evolution of average protocell area and protocell number: **(a)** As indicated in the figure, representative time courses of the average protocell area for different taxol concentrations showed an increase in average protocell area with time. The $\langle A_P \rangle$ was getting smaller with the increase in taxol concentration. **(b)** The number of protocells, N_P (different droplet preparations/experiments shown as different symbols), normalized by the respective average protocell number at t = 100 min, followed a power-law decay $\sim 1/t$. This is an alternative way to represent **(a)** at a constant total droplet area.

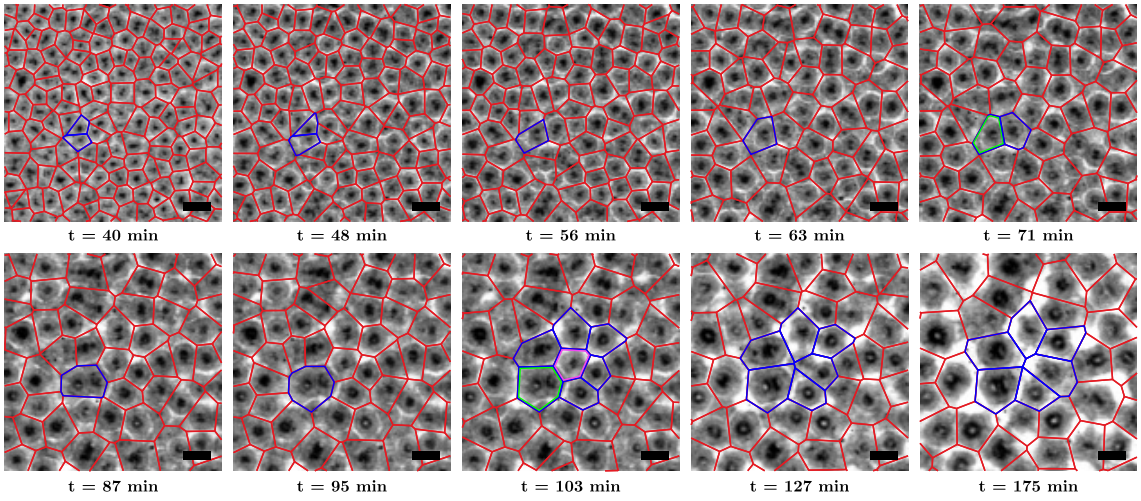

Figure A.10.: Temporal evolution of protocell: Example for the temporal evolution of protocell patterns through merging. Different colours of the Voronoi cells are to identify the merging processes of the protocells easily. The scale bar is 200 μm.

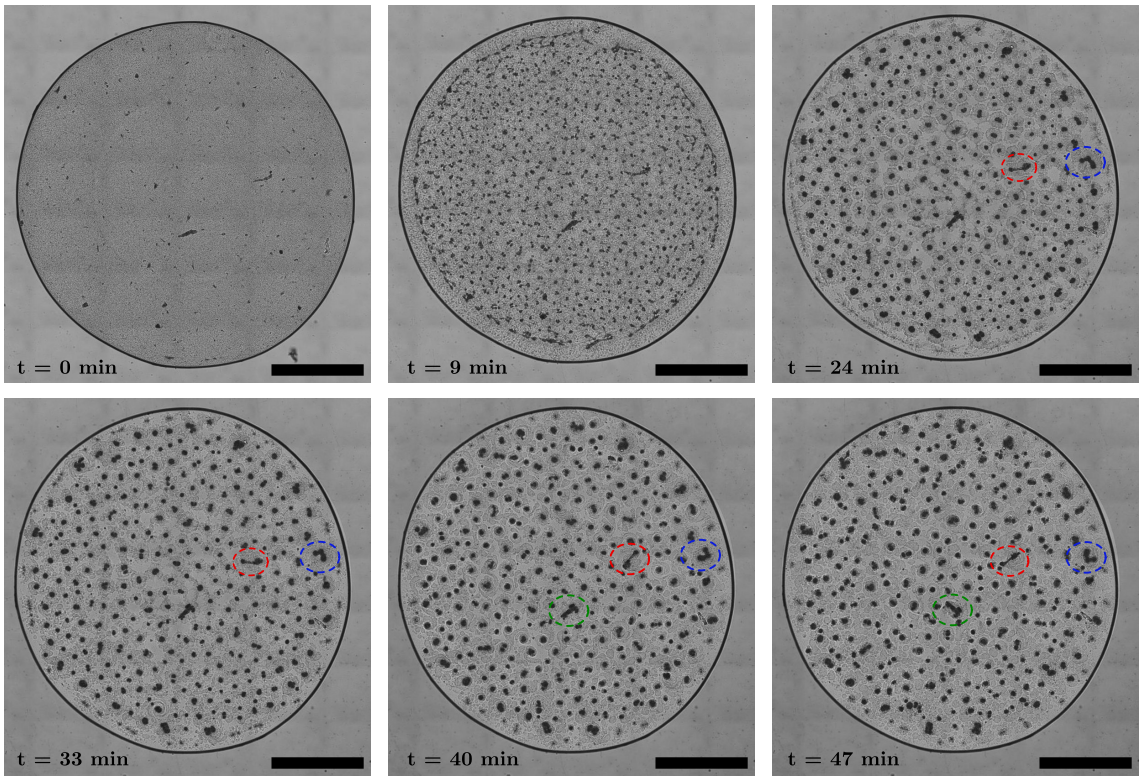

Figure A.11.: Stirring of cell-like compartments: The homogenous extract containing MSBs also resulted in cell-like compartments in a rotating magnetic field at a frequency $f = 0.1$ Hz and a magnetic field of 2.4 mT. The MSBs were uniformly distributed initially and aggregated during the protocell formation (see time intervals 0, 9, and 24 min). These MSBs were trapped inside the protocells. Any motion or agitation was not performed during this period. The MSBs started to rotate/agitate when the protocell disintegration was initiated (see the MSBs motion inside the red, green and blue circles for an idea). The motion was first visible in the droplet periphery, and the movement was subsequently observed for MSBs present in the center along with the apoptotic wave (see time points 24 to 47 min). The scale bar is 1 mm.

A.8. Additional information and figures for protocell formation in microfluidic chambers

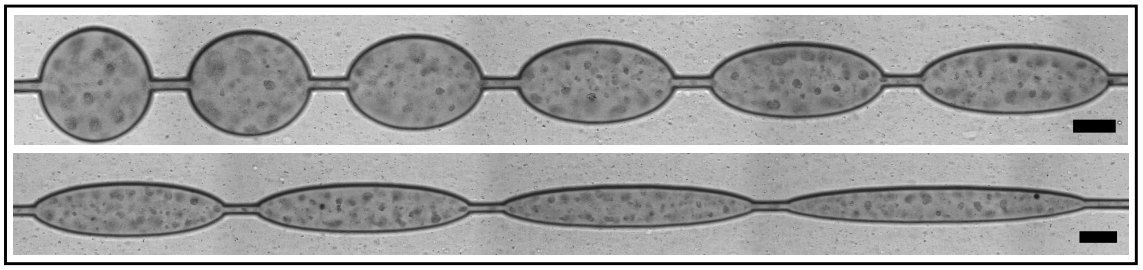

Figure A.12.: Protocell pattern formation with 1 μM taxol in the microfluidic channel: Protocells formed with extract supplemented with 1 μM taxol in the small microfluidic chambers at 142 min. The protocell patterns had a diameter of around 50-70 μm, which were uniformly distributed in the microfluidic chambers. The scale bar is 200 μm.

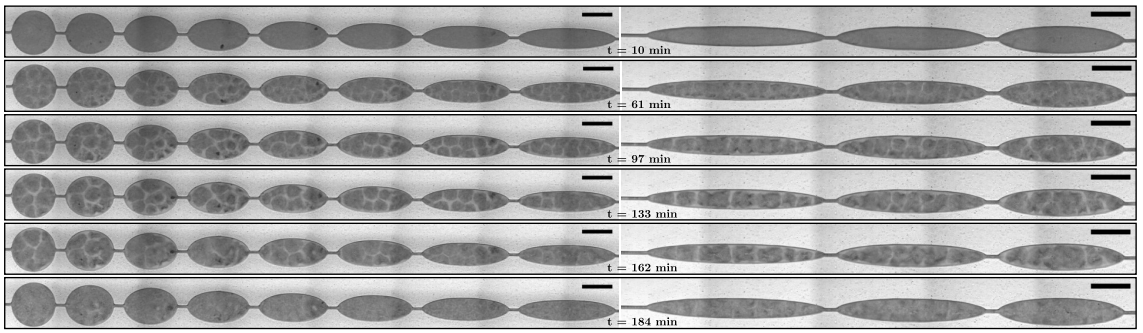

Figure A.13.: The evolution of protocell patterns over time in different microfluidic chamber geometries with the extract containing 0.1 μM taxol: The patterns formed in the microfluidic chambers are dependent on the chamber geometries. The size of the pattern is in a similar range in all geometries. However, the arrangement is dependent on the geometry. The fusion of the protocells is also visible (see figures at times 61 min and 97 min). Also, note that the pattern started to disappear at 162 min and became homogenous fluid without patterns at 184 min. The scale bar is 500 μm.

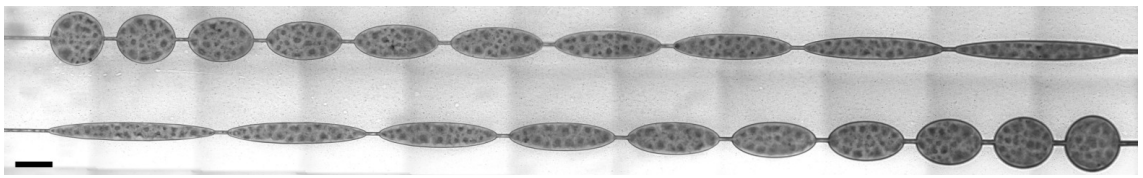

Figure A.14.: Disrupted protocell pattern formation with 0.1 μM taxol in the microfluidic CCS: Out of the three CCS in the microfluidic chip (see Figure 3.2), those filled at the end showed a significant difference in pattern formation. The extract may start to compartmentalize inside the PTFE tubing, and filling this extract in chambers may result in this different phenotype. Here the protocells formed were much smaller than the ones formed in the first filled CCS (see Figure A.13). The image was taken 100 min after starting the measurement, and the scale bar is 500 μm.

A.9. Additional information and figures for cell-like division with cycling extract in chamber

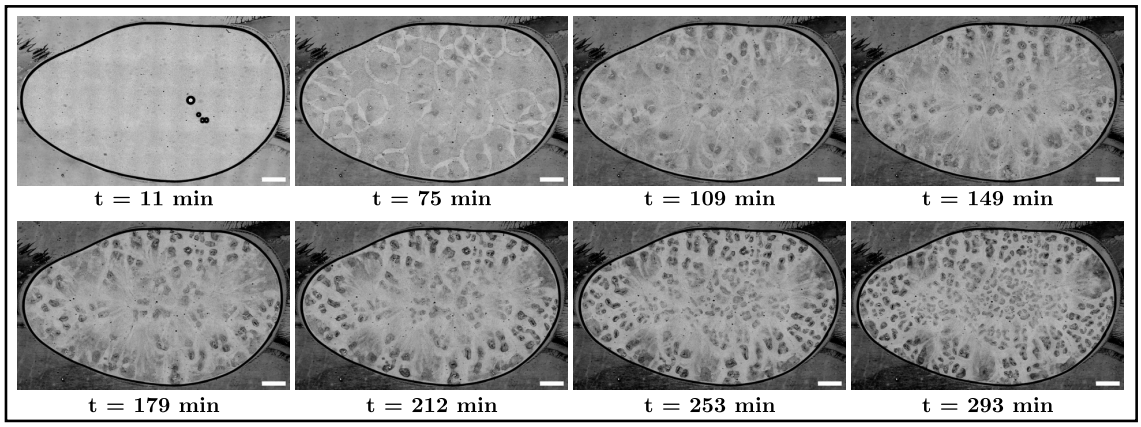

Figure A.15.: Cell-like protocell division in slab-like droplet in chamber: Time-lapse images of protocell formation in cycling extract supplemented with 100 sperm heads/μL. The extract was homogeneous initially and the mother protocell became apparent around 75 min. Subsequently, the protocells underwent multiple protocell divisions. The scale bar is 500 μm.

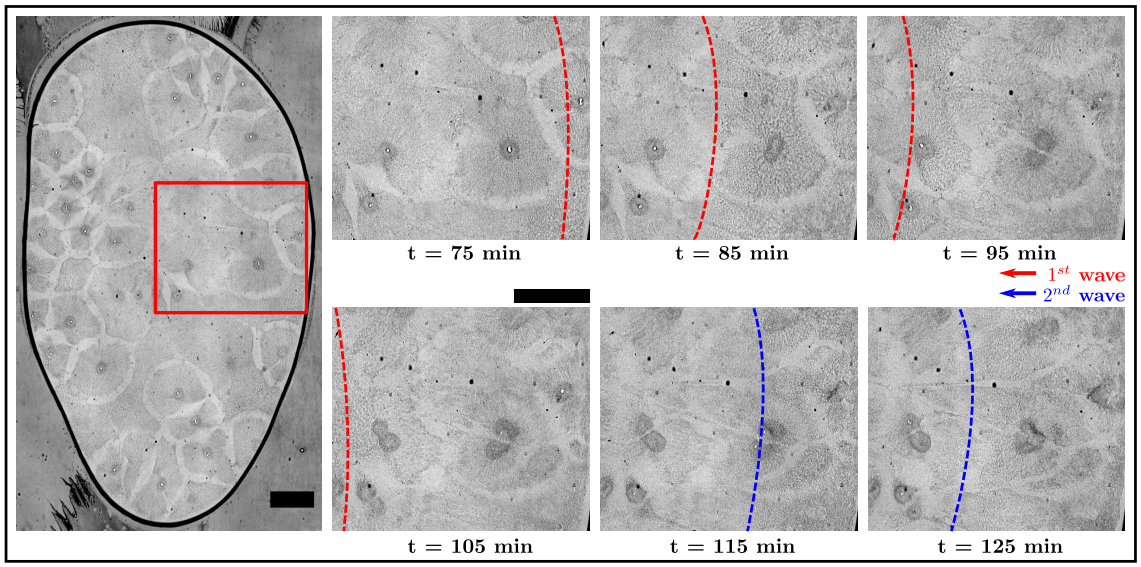

Figure A.16.: Cell-like division wave in chamber: Time-lapse images showing the propagating cell division wave inside the cycling extract droplet supplemented with 100 sperm heads/μL. In the selected region of the droplet (red rectangular region), two representative cell division waves can be seen (the first and second waves are represented by red and blue dotted lines, respectively) moving in the direction of the arrows. The protocell began to divide after the wave had passed through it (see figures from 75 to 95 min). The wave started at the droplet boundaries and ended in the center. The granularity changes near the protocells were used to detect the propagation of the cell division waves. The scale bar is 500 μm.

A.10. Additional information and figures for cell-like division in microfluidic chamber

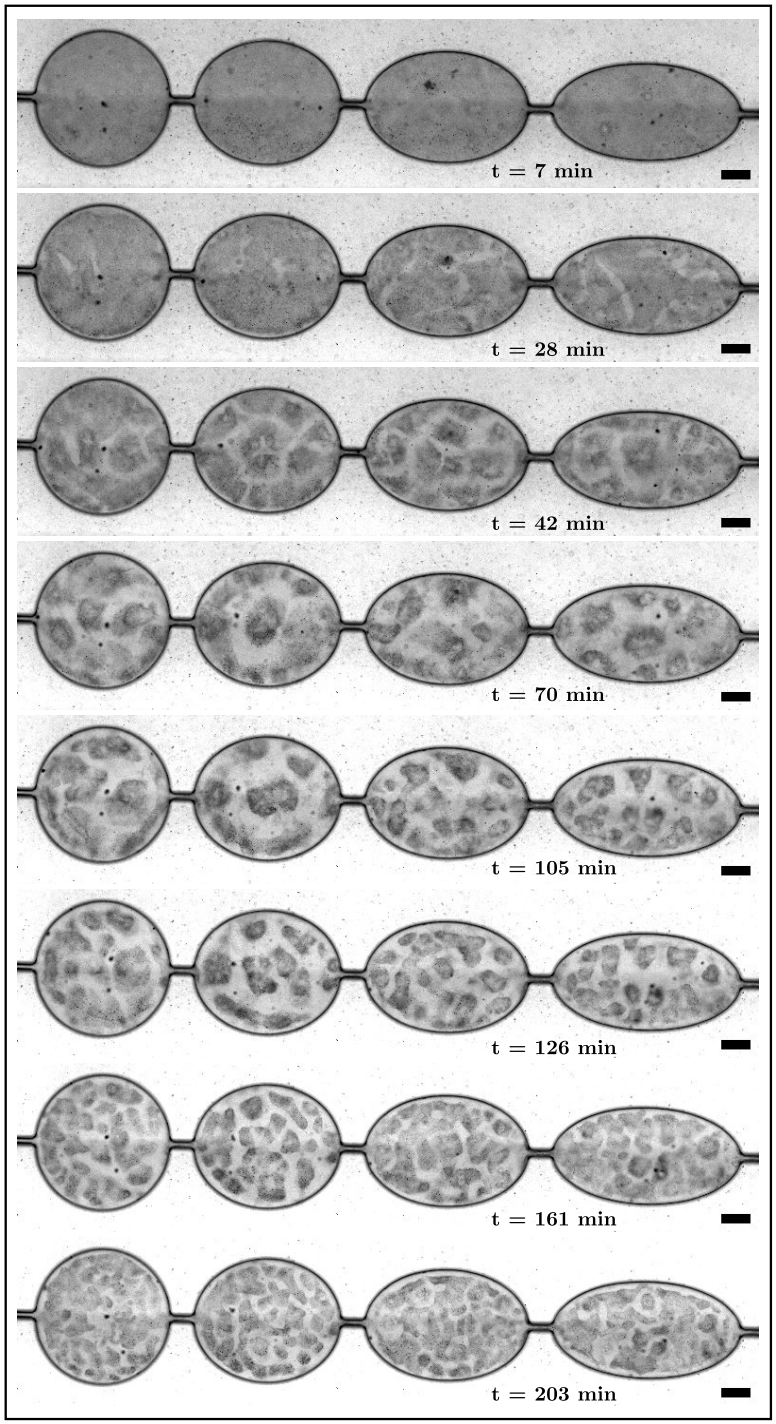

Figure A.17.: Cell-like protocell division in circular microfluidic chamber: Time-lapse images of protocell formation and cell-like division in a circular microfluidic chamber filled with cycling extract containing 100 sperm heads/μL. The protocell formed around 28 min. Subsequently, it underwent protocell divisions. Images are taken when distinguishable daughter protocells are visible during the division cycles of the protocells. The scale bar is 200 μm.

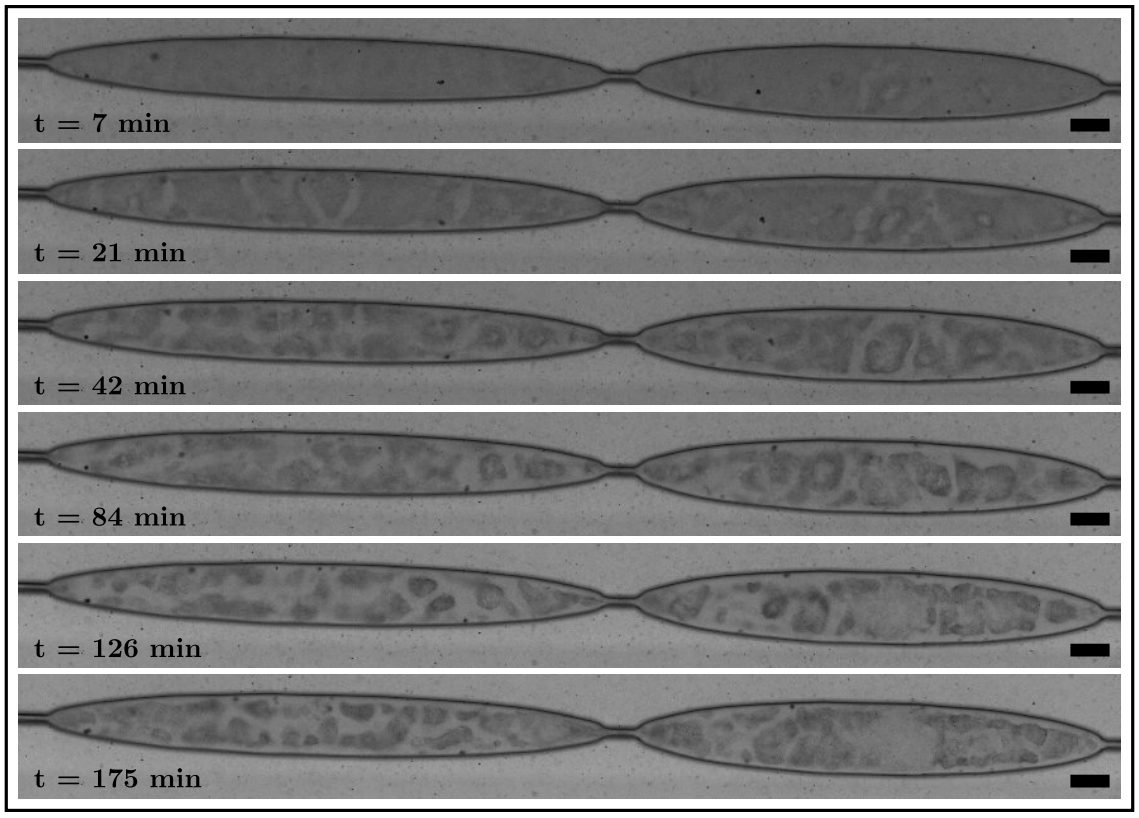

Figure A.18.: Cell-like protocell division in elongated microfluidic chamber: Time-lapse images of protocell formation and cell-like division in an elongated microfluidic chamber filled with cycling extract containing 100 sperm heads/μL. The protocell formed around 21 min. Subsequently, it underwent protocell divisions. Images are taken when distinguishable daughter protocells are visible during the division cycles of the protocells. The geometrical influence of the protocell formation and division is also clearly visible. The scale bar is 200 μm.

Abbrevations

HCG Human chorionic gonadotropin

mRNA messenger ribonucleic acid

DNA Deoxyribonucleic acid

LH Luteinizing hormone

MPF Maturation promoting factor

Cdk1 Cyclin dependent kinase 1

CSF Cytostatic factor

APC/C Anaphase promoting complex/cyclosome

EGTA Ethylene glycol-bis (β-aminoethyl ether)-N,N,N′,N′-tetraacetic acid

MTs Microtubules

PF Protofilament

GTP Guanosine 5′-triphosphate

GDP Guanosine diphosphate

MAPs Microtubule-associated protiens

Re Reynolds number

MSD Mean square displacement

D Diffusion coefficient

k_B Boltzmann constant

FBM Fractional Brownian motion

CTRW Continuous time random walk

VACF Velocity autocorrelation function

PMSG Pregnant mare serum gonadotropin

MMR Marc's Modified Ringer's

CSF Cytostatic factor

XB Extract buffer

CSF-XB Cytostatic factor extract buffer

ATP Adenosine triphosphate

ELB Egg lysis buffer

DTT Dithiothreitol

LPC Leupeptin, Pepstatin, and Chymostatin

PDMS Poly(dimethylsiloxane)

PTFE Polytetrafluoroethylene

CCS Chamber channel system

SPT Single particle tracking

FWHM Full-width-at-half-maximum

VT Voronoi tesselation

NPs Nanoparticles

Fe_3O_4 Iron oxide

OA@NPs Oleic acid stabilized Fe_3O_4 NPs

CA@NPs Citric acid stabilized Fe_3O_4 NPs

MSBs Magnetic stir bars

SiO_2 Silicon dioxide

Si Silicon

SEM Scanning electron microscope

EW Electronic workshop

PWM Pulse width modulation

2mag stirrer MIXdrive 1 XS from 2mag AG

2mag driver MIXcontrol eco DINrail from 2mag AG

EW controller Controller made at the electronic workshop

APTES (3-Aminopropyl)triethoxysilane

FITC Fluorescein isothiocyanate

FEP Fluorinated ethylene propylene

FA FITC linked APTES

FITC-MSBs MSBs labelled with FITC

AA ATTO 390 linked APTES

ATTO-MSBs MSBs labelled with ATTO 390

SNR Signal-to-noise ratio

PBs 200 nm diameter fluorescent beads

TA-MSD Time-averaged MSD

EA-TA-MSD Ensemble-averaged time-averaged MSD

PDF Probability density function

P Peclet number

DAPI 4′,6-diamidino-2-phenylindole

DMSO Dimethyl sulfoxide

FEP Fluorinated ethylene propylene

MDCK-II Madin-Darby Canine Kidney II

List of Figures

Bibliography

1. Wedlich-Söldner, R. & Betz, T. *Self-organization: the fundament of cell biology*. Philosophical Transactions of the Royal Society B: Biological Sciences **373**, 20170103. doi:10.1098/rstb.2017.0103 (2018) (Cited on pages 1, 70).

2. Misteli, T. *The concept of self-organization in cellular architecture*. Journal of Cell Biology **155**, 181–186. doi:10.1083/jcb.200108110 (2001) (Cited on pages 1, 2).

3. Koch, A. J. & Meinhardt, H. *Biological pattern formation: from basic mechanisms to complex structures*. Reviews of Modern Physics **66**, 1481–1507. doi:10.1103/revmodphys.66.1481 (1994) (Cited on page 1).

4. Karsenti, E. *Self-organization in cell biology: a brief history*. Nature Reviews Molecular Cell Biology **9**, 255–262. doi:10.1038/nrm2357 (2008) (Cited on page 1).

5. Roth, S. *Mathematics and biology: a Kantian view on the history of pattern formation theory*. Development Genes and Evolution **221**, 255–279. doi:10.1007/s00427-011-0378-0 (2011) (Cited on page 1).

6. Turing, A. M. *The chemical basis of morphogenesis*. Philosophical Transactions of the Royal Society of London. Series B, Biological Sciences **237**, 37–72. doi:10.1098/rstb.1952.0012 (1952) (Cited on page 1).

7. Halatek, J., Brauns, F. & Frey, E. *Self-organization principles of intracellular pattern formation*. Philosophical Transactions of the Royal Society B: Biological Sciences **373**, 20170107. doi:10.1098/rstb.2017.0107 (2018) (Cited on page 1).

8. Kondo, S. & Miura, T. *Reaction-diffusion model as a framework for understanding biological pattern formation*. Science **329**, 1616–1620. doi:10.1126/science.1179047 (2010) (Cited on page 1).

9. Tabony, J., Glade, N., Demongeot, J. & Papaseit, C. *Biological self-organization by way of microtubule reaction-diffusion processes*. Langmuir **18**, 7196–7207. doi:10.1021/la0255875 (2002) (Cited on page 1).

10. Fuller, B. G. *Self-organization of intracellular gradients during mitosis*. Cell Division **5**, 5. doi:10.1186/1747-1028-5-5 (2010) (Cited on page 1).

11. Nédélec, F. J., Surrey, T., Maggs, A. C. & Leibler, S. *Self-organization of microtubules and motors*. Nature **389**, 305–308. doi:10.1038/38532 (1997) (Cited on pages 2, 77).

12. Good, M. C., Vahey, M. D., Skandarajah, A., Fletcher, D. A. & Heald, R. *Cytoplasmic volume modulates spindle size during embryogenesis*. Science **342**, 856–860. doi:10.1126/science.1243147 (2013) (Cited on pages 2, 9, 18, 22, 31, 58, 63, 64, 66, 68, 93).

13. Hazel, J., Krutkramelis, K., Mooney, P., Tomschik, M., Gerow, K., Oakey, J. & Gatlin, J. C. *Changes in cytoplasmic volume are sufficient to drive spindle scaling*. Science **342**, 853–856. doi:10.1126/science.1243110 (2013) (Cited on pages 2, 6, 31, 63, 64, 66, 68).

14. Cheng, X. & Ferrell, J. E. *Spontaneous emergence of cell-like organization in Xenopus egg extracts*. Science **366**, 631–637. doi:10.1126/science.aav7793 (2019) (Cited on pages 2, 70, 73, 76, 84–86, 88).

15. Höfling, F. & Franosch, T. *Anomalous transport in the crowded world of biological cells*. Reports on Progress in Physics **76**, 046602. doi:10.1088/0034-4885/76/4/046602 (2013) (Cited on pages 2, 26, 31).

16. Weiss, M. *Chapter 11 Crowding, diffusion, and biochemical reactions.* In: International Review of Cell and Molecular Biology. (eds Hancock, R. & Jeon, K. W.) vol. 307, 383–417 (Academic Press, 2014). doi:10.1016/B978-0-12-800046-5.00011-4 (Cited on pages 2, 31).

17. Fortriede, J. D., Pells, T. J., Chu, S., Chaturvedi, P., *et al. Xenbase: deep integration of GEO & amp; SRA RNA-seq and ChIP-seq data in a model organism database*. Nucleic Acids Research **48**, D776–D782. doi:10.1093/nar/gkz933 (2019) (Cited on page 5).

18. *Xenbase Home,* xenbase.org. [Accessed 28-06-2022]. https://www.xenbase.org/entry/ (Cited on page 5).

19. Harland, R. M. & Grainger, R. M. *Xenopus research: metamorphosed by genetics and genomics*. Trends in Genetics **27**, 507–515. doi:10.1016/j.tig.2011.08.003 (2011) (Cited on pages 5, 6).

20. Wheeler, G. N. & Brändli, A. W. *Simple vertebrate models for chemical genetics and drug discovery screens: Lessons from zebrafish and Xenopus*. Developmental Dynamics **238**, 1287–1308. doi:10.1002/dvdy.21967 (2009) (Cited on page 5).

21. Nikos, P. *Xenopus laevis as a model system*. Materials and Methods **2**. doi:10.13070/mm.en.2.151 (2012) (Cited on page 5).

22. Sive, H. L., Grainger, R. M. & Harland, R. M. *Inducing ovulation in Xenopus laevis*. Cold Spring Harbor Protocols **2007**, pdb.prot4734. doi:10.1101/pdb.prot4734 (2007) (Cited on page 5).

23. Murray, A. W. *Chapter 30 Cell cycle extracts.* In: Methods in Cell Biology. (eds Kay, B. K. & Peng, H. B.) vol. 36, 581–605 (Academic Press, 1991). doi:10.1016/S0091-679X(08)60298-8 (Cited on pages 5, 6, 18, 64, 84, 93).

24. Elkan, E. R. *The Xenopus pregnancy test*. The British Medical Journal **2**, 1253–1274. doi:10.1136/bmj.2.4067.1253 (1938) (Cited on page 5).

25. Gurdon, J. B. & Hopwood, N. *The introduction of Xenopus laevis into developmental biology: of empire, pregnancy testing and ribosomal genes*. The International Journal of Developmental Biology **44**, 43–50 (2000) (Cited on page 5).

26. *The Nobel Prize in Physiology or Medicine 2012,* NobelPrize.org. [Accessed 02-07-2022]. https://www.nobelprize.org/prizes/medicine/2012/press-release/ (Cited on page 5).

27. Gurdon, J. B. *The developmental capacity of nuclei taken from intestinal epithelium cells of feeding tadpoles*. Development **10**, 622–640. doi:10.1242/dev.10.4.622 (1962) (Cited on pages 5, 6).

28. Levick, S. E. *From Xenopus to Oedipus: "Dolly", human cloning, and psychological and social "Cloneness"*. Cloning and Stem Cells **9**, 33–39. doi:10.1089/clo.2006.0087 (2007) (Cited on page 5).

29. Afouda, B. A. & Hoppler, S. *Xenopus explants as an experimental model system for studying heart development*. Trends in Cardiovascular Medicine **19**, 220–226. doi:10.1016/j.tcm.2010.01.001 (2009) (Cited on page 6).

30. Kha, C. X., Son, P. H., Lauper, J. & Tseng, K. A.-S. *A model for investigating developmental eye repair in Xenopus laevis*. Experimental Eye Research **169**, 38–47. doi:10.1016/j.exer.2018.01.007 (2018) (Cited on page 6).

31. Soreq, H. & Seidman, S. *Chapter 14 Xenopus oocyte microinjection: from gene to protein.* In: Methods in Enzymology. vol. 207, 225–265 (Academic Press, 1992). doi:10.1016/0076-6879(92)07016-H (Cited on page 6).

32. Sible, J. C. & Wroble, B. N. *Expression of exogenous mRNA in Xenopus laevis embryos for the study of cell cycle regulation.* In: Microinjection: Methods and Applications. (ed Carroll, D. J.) vol. 518, 1–15 (Humana Press, Totowa, NJ, 2009). doi:10.1007/978-1-59745-202-1_1 (Cited on page 6).

33. Lei, Y., Guo, X., Liu, Y., Cao, Y., Deng, Y., Chen, X., Cheng, C. H. K., Dawid, I. B., Chen, Y. & Zhao, H. *Efficient targeted gene disruption in Xenopus embryos using engineered transcription activator-like effector nucleases (TALENs)*. Proceedings of the National Academy of Sciences **109**, 17484–17489. doi:10.1073/pnas.1215421109 (2012) (Cited on page 6).

34. Caherec, F. L., Bron, P., Verbavatz, J., Garret, A., Morel, G., Cavalier, A., Bonnec, G., Thomas, D., Gouranton, J. & Hubert, J. *Incorporation of proteins into Xenopus oocytes by proteoliposome microinjection: functional characterization of a novel aquaporin*. Journal of Cell Science **109**, 1285–1295. doi:10.1242/jcs.109.6.1285 (1996) (Cited on page 6).

35. Moody, S. A. *Fates of the blastomeres of the 16-cell stage Xenopus embryo*. Developmental Biology **119**, 560–578. doi:10.1016/0012-1606(87)90059-5 (1987) (Cited on page 6).

36. Moody, S. A. *Fates of the blastomeres of the 32-cell stage Xenopus embryo*. Developmental Biology **122**, 300–319. doi:10.1016/0012-1606(87)90296-x (1987) (Cited on page 6).

37. Akhmanova, A. & Steinmetz, M. O. *Control of microtubule organization and dynamics: two ends in the limelight*. Nature Reviews Molecular Cell Biology **16**, 711–726. doi:10.1038/nrm4084 (2015) (Cited on pages 6, 9).

38. Gadde, S. & Heald, R. *Mechanisms and molecules of the mitotic spindle*. Current Biology **14**, R797–R805. doi:10.1016/j.cub.2004.09.021 (2004) (Cited on pages 6, 9).

39. Blow, J. J. & Laskey, R. A. *Xenopus cell-free extracts and their contribution to the study of DNA replication and other complex biological processes*. The International Journal of Developmental Biology **60**, 201–207. doi:10.1387/ijdb.160142jb (2016) (Cited on page 6).

40. Blow, J. J. & Laskey, R. A. *A role for the nuclear envelope in controlling DNA replication within the cell cycle*. Nature **332**, 546–548. doi:10.1038/332546a0 (1988) (Cited on page 6).

41. Murray, A. W. & Kirschner, M. W. *Cyclin synthesis drives the early embryonic cell cycle*. Nature **339**, 275–280. doi:10.1038/339275a0 (1989) (Cited on page 6).

42. Belmont, L., Hyman, A., Sawin, K. & Mitchison, T. *Real-time visualization of cell cycle-dependent changes in microtubule dynamics in cytoplasmic extracts*. Cell **62**, 579–589. doi:10.1016/0092-8674(90)90022-7 (1990) (Cited on page 6).

43. Cupello, S., Richardson, C. & Yan, S. *Cell-free Xenopus egg extracts for studying DNA damage response pathways*. The International Journal of Developmental Biology **60**, 229–236. doi:10.1387/ijdb.160113sy (2016) (Cited on page 6).

44. Chang, J. B. & Jr, J. E. F. *Mitotic trigger waves and the spatial coordination of the Xenopus cell cycle*. Nature **500**, 603–607. doi:10.1038/nature12321 (2013) (Cited on pages 6, 7, 84–86).

45. Yang, Q. & Ferrell, J. E. *The Cdk1–APC/C cell cycle oscillator circuit functions as a time-delayed, ultrasensitive switch*. Nature Cell Biology **15**, 519–525. doi:10.1038/ncb2737 (2013) (Cited on pages 6, 7).

46. Walczak, C. E. & Heald, R. *Chapter 3 - Mechanisms of mitotic spindle assembly and function.* In: International Review of Cytology. (ed Jeon, K. W.) vol. 265, 111–158 (Academic Press, 2008). doi:10.1016/S0074-7696(07)65003-7 (Cited on pages 6, 7, 9).

47. Desai, A., Maddox, P. S., Mitchison, T. J. & Salmon, E. *Anaphase A chromosome movement and poleward spindle microtubule flux occur at similar rates in Xenopus extract spindles*. Journal of Cell Biology **141**, 703–713. doi:10.1083/jcb.141.3.703 (1998) (Cited on page 6).

48. Murray, A. W., Desai, A. B. & Salmon, E. D. *Real time observation of anaphase in vitro.* Proceedings of the National Academy of Sciences **93**, 12327–12332. doi:10.1073/pnas.93.22.12327 (1996) (Cited on page 6).

49. Verde, F, Dogterom, M, Stelzer, E, Karsenti, E & Leibler, S. *Control of microtubule dynamics and length by cyclin A- and cyclin B-dependent kinases in Xenopus egg extracts.* Journal of Cell Biology **118**, 1097–1108. doi:10.1083/jcb.118.5.1097 (1992) (Cited on page 6).

50. Field, C. M., Wühr, M., Anderson, G. A., Kueh, H. Y., Strickland, D. & Mitchison, T. J. *Actin behavior in bulk cytoplasm is cell cycle regulated in early vertebrate embryos*. Journal of Cell Science **124**, 2086–2095. doi:10.1242/jcs.082263 (2011) (Cited on pages 6, 7).

51. Newmeyer, D. *Cell-free apoptosis in Xenopus egg extracts: Inhibition by Bcl-2 and requirement for an organelle fraction enriched in mitochondria*. Cell **79**, 353–364. doi:10.1016/0092-8674(94)90203-8 (1994) (Cited on page 6).

52. *Molecular biology of the cell* 5th ed. (eds Alberts, B., Johnson, A., Lewis, J., Raff, M., Roberts, K. & Walter, P.) (CRC Press, Boca Raton, FL, 2007) (Cited on pages 7–9).

53. Bartee, L., Shriner, W. & Creech, C. *Principles of biology: biology 211, 212, and 213* eng. OCLC: 1341864177 (Open Oregon Educational Resources, Oregon, 2020) (Cited on page 7).

54. Ferrell, J. E. *Xenopus oocyte maturation: new lessons from a good egg*. BioEssays **21**, 833–842. doi:10.1002/(sici)1521-1878(199910)21:10<833::aid-bies5>3.0.co;2-p (1999) (Cited on page 7).

55. Tunquist, B. J. & Maller, J. L. *Under arrest: cytostatic factor (CSF)-mediated metaphase arrest in vertebrate eggs*. Genes & Development **17**, 683–710. doi:10.1101/gad.1071303 (2003) (Cited on pages 7, 9, 63).

56. Tokmakov, A. A., Matsumoto, Y., Isobe, T. & Sato, K.-I. *In vitro reconstruction of Xenopus oocyte ovulation*. en. International Journal of Molecular Sciences **20**, 4766. doi:10.3390/ijms20194766 (2019) (Cited on page 7).

57. Masui, Y. *The role of "cytostatic factor (CSF)" in the control of oocyte cell cycles: a summary of 20 years of study. (CSF/MPF/cell cycle/metaphase arrest)*. Development, Growth and Differentiation **33**, 543–551. doi:10.1111/j.1440-169X.1991.00543.x (1991) (Cited on page 7).

58. Madgwick, S. & Jones, K. T. *How eggs arrest at metaphase II: MPF stabilisation plus APC/C inhibition equals Cytostatic Factor*. Cell Division **2**, 4. doi:10.1186/1747-1028-2-4 (2007) (Cited on page 7).

59. Gillespie, P. J., Gambus, A. & Blow, J. J. *Preparation and use of Xenopus egg extracts to study DNA replication and chromatin associated proteins*. Methods **57**, 203–213. doi:10.1016/j.ymeth.2012.03.029 (2012) (Cited on page 7).

60. Good, M. C. & Heald, R. *Preparation of cellular extracts from Xenopus eggs and embryos*. Cold Spring Harbor Protocols **2018**, 429–439. doi:10.1101/pdb.prot097055 (2018) (Cited on pages 7, 8, 18, 93).

61. Tokmakov, A. A., Sato, K.-I. & Fukami, Y. *Calcium oscillations in Xenopus egg cycling extracts*. Journal of Cellular Biochemistry **82**, 89–97. doi:10.1002/jcb.1140 (2001) (Cited on page 8).

62. Alfaro-Aco, R. & Petry, S. *Building the microtubule cytoskeleton piece by piece*. Journal of Biological Chemistry **290**, 17154–17162. doi:10.1074/jbc.r115.638452 (2015) (Cited on page 8).

63. Brinkley, W. B. *Microtubules: a brief historical perspective*. Journal of Structural Biology **118**, 84–86. doi:10.1006/jsbi.1997.3854 (1997) (Cited on page 8).

64. Löwe, J, Li, H, Downing, K. & Nogales, E. *Refined structure of $\alpha\beta$-tubulin at 3.5 Å resolution*. Journal of Molecular Biology **313**, 1045–1057. doi:10.1006/jmbi.2001.5077 (2001) (Cited on page 8).

65. Li, H., DeRosier, D. J., Nicholson, W. V., Nogales, E. & Downing, K. H. *Microtubule structure at 8 Å resolution*. Structure **10**, 1317–1328. doi:10.1016/s0969-2126(02)00827-4 (2002) (Cited on page 8).

66. Zhang, R., LaFrance, B. & Nogales, E. *Separating the effects of nucleotide and EB binding on microtubule structure*. Proceedings of the National Academy of Sciences **115**, E6191–E6200. doi:10.1073/pnas.1802637115 (2018) (Cited on pages 8, 9).

67. McIntosh, J. R., Morphew, M. K., Grissom, P. M., Gilbert, S. P. & Hoenger, A. *Lattice structure of cytoplasmic microtubules in a cultured mammalian cell*. Journal of Molecular Biology **394**, 177–182. doi:10.1016/j.jmb.2009.09.033 (2009) (Cited on page 8).

68. Chaaban, S. & Brouhard, G. J. *A microtubule bestiary: structural diversity in tubulin polymers*. Molecular Biology of the Cell **28** (ed Bement, W.) 2924–2931. doi:10.1091/mbc.e16-05-0271 (2017) (Cited on page 8).

69. Johnson, K. A. & Borisy, G. G. *Kinetic analysis of microtubule self-assembly in vitro*. Journal of Molecular Biology **117**, 1–31. doi:10.1016/0022-2836(77)90020-1 (1977) (Cited on page 8).

70. Roostalu, J. & Surrey, T. *Microtubule nucleation: beyond the template*. Nature Reviews Molecular Cell Biology **18**, 702–710. doi:10.1038/nrm.2017.75 (2017) (Cited on page 8).

71. Hamel, E., Del Campo, A., Lowe, M. & Lin, C. *Interactions of taxol, microtubule-associated proteins, and guanine nucleotides in tubulin polymerization*. Journal of Biological Chemistry **256**, 11887–11894. doi:10.1016/S0021-9258(19)68489-9 (1981) (Cited on page 8).

72. Kellogg, E. H., Hejab, N. M., Howes, S., Northcote, P., Miller, J. H., Díaz, J. F., Downing, K. H. & Nogales, E. *Insights into the distinct mechanisms of action of Taxane and non-Taxane microtubule stabilizers from cryo-EM structures*. Journal of Molecular Biology **429**, 633–646. doi:10.1016/j.jmb.2017.01.001 (2017) (Cited on page 8).

73. Lee, J. C., Hirsh, J. & Timasheff, S. N. *In vitro formation of filaments from calf brain microtubule protein*. Archives of Biochemistry and Biophysics **168**, 726–729. doi:10.1016/0003-9861(75)90308-2 (1975) (Cited on page 8).

74. Job, D., Valiron, O. & Oakley, B. *Microtubule nucleation*. Current Opinion in Cell Biology **15**, 111–117. doi:10.1016/s0955-0674(02)00003-0 (2003) (Cited on page 8).

75. Goshima, G., Mayer, M., Zhang, N., Stuurman, N. & Vale, R. D. *Augmin: a protein complex required for centrosome-independent microtubule generation within the spindle*. Journal of Cell Biology **181**, 421–429. doi:10.1083/jcb.200711053 (2008) (Cited on page 8).

76. Hsia, K.-C., Wilson-Kubalek, E. M., Dottore, A., Hao, Q., Tsai, K.-L., Forth, S., Shimamoto, Y., Milligan, R. A. & Kapoor, T. M. *Reconstitution of the augmin complex provides insights into its architecture and function*. Nature Cell Biology **16**, 852–863. doi:10.1038/ncb3030 (2014) (Cited on page 8).

77. Petry, S., Groen, A. C., Ishihara, K., Mitchison, T. J. & Vale, R. D. *Branching microtubule nucleation in Xenopus egg extracts mediated by augmin and TPX2*. Cell **152**, 768–777. doi:10.1016/j.cell.2012.12.044 (2013) (Cited on page 8).

78. Mitchison, T. & Kirschner, M. *Dynamic instability of microtubule growth*. Nature **312**, 237–242. doi:10.1038/312237a0 (1984) (Cited on page 8).

79. Michaels, T. C., Feng, S., Liang, H. & Mahadevan, L. *Mechanics and kinetics of dynamic instability*. eLife **9**, e54077. doi:10.7554/elife.54077 (2020) (Cited on page 9).

80. Heald, R. & Nogales, E. *Microtubule dynamics*. Journal of Cell Science **115**, 3–4. doi:10.1242/jcs.115.1.3 (2002) (Cited on page 9).

81. Menéndez, M., Rivas, G., Díaz, J. F. & Andreu, J. M. *Control of the structural stability of the tubulin dimer by one high affinity bound magnesium ion at nucleotide N-site*. Journal of Biological Chemistry **273**, 167–176. doi:10.1074/jbc.273.1.167 (1998) (Cited on page 9).

82. Valiron, O., Caudron, N. & Job, D. *Microtubule dynamics*. Cellular and Molecular Life Sciences **58**, 2069–2084. doi:10.1007/pl00000837 (2001) (Cited on page 9).

83. Gudimchuk, N. B. & McIntosh, J. R. *Regulation of microtubule dynamics, mechanics and function through the growing tip*. Nature Reviews Molecular Cell Biology **22**, 777–795. doi:10.1038/s41580-021-00399-x (2021) (Cited on page 9).

84. Dimitrov, A., Quesnoit, M., Moutel, S., Cantaloube, I., Poüs, C. & Perez, F. *Detection of GTP-tubulin conformation in vivo reveals a role for GTP remnants in microtubule rescues*. Science **322**, 1353–1356. doi:10.1126/science.1165401 (2008) (Cited on page 9).

85. McIntosh, J. & Hays, T. *A brief history of research on mitotic mechanisms*. Biology **5**, 55. doi:10.3390/biology5040055 (2016) (Cited on page 9).

86. Cross, M. K. & Powers, M. A. *Learning about cancer from frogs: analysis of mitotic spindles in Xenopus egg extracts*. Disease Models & Mechanisms **2**, 541–547. doi:10.1242/dmm.002022 (2009) (Cited on pages 10, 63).

87. Hannak, E. & Heald, R. *Investigating mitotic spindle assembly and function in vitro using Xenopus laevis egg extracts*. Nature Protocols **1**, 2305–2314. doi:10.1038/nprot.2006.396 (2006) (Cited on pages 10, 18, 63, 93).

88. Wittmann, T., Hyman, A. & Desai, A. *The spindle: a dynamic assembly of microtubules and motors*. Nature Cell Biology **3**, E28–E34. doi:10.1038/35050669 (2001) (Cited on page 9).

89. Titus, J. & Wadsworth, P. *Mitotic spindle assembly: the role of motor proteins.* In: Encyclopedia of Life Sciences (eLS). (John Wiley & Sons, Ltd, 2012). doi:10.1002/9780470015902.a0022519 (Cited on page 9).

90. Sawin, K. E. & Mitchison, T. J. *Mitotic spindle assembly by two different pathways in vitro.* Journal of Cell Biology **112**, 925–940. doi:10.1083/jcb.112.5.925 (1991) (Cited on pages 9, 10, 63).

91. Lohka, M. J. & Maller, J. L. *Induction of nuclear envelope breakdown, chromosome condensation, and spindle formation in cell-free extracts.* The Journal of Cell Biology **101**, 518–523. doi:10.1083/jcb.101.2.518 (1985) (Cited on page 9).

92. Heald, R., Tournebize, R., Habermann, A., Karsenti, E. & Hyman, A. *Spindle assembly in Xenopus egg extracts: respective roles of centrosomes and microtubule self-organization*. Journal of Cell Biology **138**, 615–628. doi:10.1083/jcb.138.3.615 (1997) (Cited on page 9).

93. Loughlin, R., Wilbur, J. D., McNally, F. J., Nédélec, F. J. & Heald, R. *Katanin contributes to interspecies spindle length scaling in Xenopus*. Cell **147**, 1397–1407. doi:10.1016/j.cell.2011.11.014 (2011) (Cited on pages 9, 63).

94. Bisht, J. S., Tomschik, M. & Gatlin, J. C. *Induction of a spindle-assembly-competent M phase in Xenopus egg extracts*. Current Biology **29**, 1273–1285.e5. doi:10.1016/j.cub.2019.02.061 (2019) (Cited on pages 9, 63).

95. Mitchison, T. J., Maddox, P., Gaetz, J., Groen, A., Shirasu, M., Desai, A., Salmon, E. D. & Kapoor, T. M. *Roles of polymerization dynamics, opposed motors, and a tensile element in governing the length of Xenopus extract meiotic spindles*. Molecular Biology of the Cell **16**, 3064–3076. doi:10.1091/mbc.e05-02-0174 (2005) (Cited on page 9).

96. Brugués, J., Nuzzo, V., Mazur, E. & Needleman, D. J. *Nucleation and transport organize microtubules in metaphase spindles*. Cell **149**, 554–564. doi:10.1016/j.cell.2012.03.027 (2012) (Cited on pages 9, 63).

97. Mogilner, A. & Craig, E. *Towards a quantitative understanding of mitotic spindle assembly and mechanics*. Journal of Cell Science **123**, 3435–3445. doi:10.1242/jcs.062208 (2010) (Cited on pages 9, 63).

98. Wilde, A. & Zheng, Y. *Stimulation of microtubule aster formation and spindle assembly by the small GTPase Ran*. Science **284**, 1359–1362. doi:10.1126/science.284.5418.1359 (1999) (Cited on page 10).

99. Brown, R. *XXVII. A brief account of microscopical observations made in the months of June, July and August 1827, on the particles contained in the pollen of plants; and on the general existence of active molecules in organic and inorganic bodies*. en. The Philosophical Magazine **4**, 161–173. doi:10.1080/14786442808674769 (1828) (Cited on page 11).

100. Einstein, A. *Über die von der molekularkinetischen Theorie der Wärme geforderte Bewegung von in ruhenden Flüssigkeiten suspendierten Teilchen*. de. Annalen der Physik **322**, 549–560. doi:10.1002/andp.19053220806 (1905) (Cited on pages 11, 13).

101. Einstein, A. *The collected papers of Albert Einstein. 2: The Swiss years: writings, 1900 - 1909: English translation* (Princeton Univ. Pr, Princeton, NJ, 1989) (Cited on page 11).

102. Von Smoluchowski, M. *Zur kinetischen Theorie der Brownschen Molekularbewegung und der Suspensionen*. Annalen der Physik **326**, 756–780. doi:10.1002/andp.19063261405 (1906) (Cited on page 11).

103. Perrin, J. B. *Mouvement brownien et réalité moléculaire*. Annales de Chimie et de Physique **18**, 5–114. eprint: https://gallica.bnf.fr/ark:/12148/bpt6k96034900/f1.item (1909) (Cited on page 11).

104. *The Nobel Prize in Physics 1926,* NobelPrize.org. [Accessed 02-06-2022]. https://www.nobelprize.org/prizes/physics/1926/summary/ (Cited on page 11).

105. Langevin, P. *Sur la théorie du mouvement brownien (On the Theory of Brownian Motion)*. fr. Comptes-rendus de l'Académie des sciences **146**, 530–533. eprint: https://www.academie-sciences.fr/archivage_site/activite/hds/textes/tsf_Kahane1.pdf (1908) (Cited on page 11).

106. Oliveira, F. A., Ferreira, R. M. S., Lapas, L. C. & Vainstein, M. H. *Anomalous diffusion: a basic mechanism for the evolution of inhomogeneous systems*. Frontiers in Physics **7**, 18. doi:10.3389/fphy.2019.00018 (2019) (Cited on page 11).

107. Purcell, E. M. *Life at low Reynolds number*. American Journal of Physics **45**, 3–11. doi:10.1119/1.10903 (1977) (Cited on page 12).

108. Fick, A. *Ueber Diffusion*. de. Annalen der Physik und Chemie **170**, 59–86. doi:10.1002/andp.18551700105 (1855) (Cited on page 12).

109. Walters, P. *An introduction to ergodic theory* 1st ed. *Graduate texts in mathematics* **79** (Springer, New York, 2000) (Cited on page 13).

110. Huang, K. *Introduction to statistical physics* (Taylor & Francis, London; New York, 2001) (Cited on page 13).

111. Kubo, R. *The fluctuation-dissipation theorem*. Reports on Progress in Physics **29**, 255. doi:10.1088/0034-4885/29/1/306 (1966) (Cited on page 13).

112. Berg, H. C. *Random walks in biology* Expanded ed (Princeton University Press, Princeton, N.J, 1993) (Cited on page 13).

113. Metzler, R., Jeon, J.-H., Cherstvy, A. G. & Barkai, E. *Anomalous diffusion models and their properties: non-stationarity, non-ergodicity, and ageing at the centenary of single particle tracking*. Physical Chemistry Chemical Physics **16**, 24128–24164. doi:10.1039/C4CP03465A (2014) (Cited on pages 13–15, 52, 56).

114. Vilk, O., Aghion, E., Avgar, T., Beta, C., *et al. Unravelling the origins of anomalous diffusion: From molecules to migrating storks*. Physical Review Research **4**, 033055. doi:10.1103/PhysRevResearch.4.033055 (2022) (Cited on page 13).

115. Metzler, R. & Klafter, J. *The restaurant at the end of the random walk: recent developments in the description of anomalous transport by fractional dynamics*. Journal of Physics A: Mathematical and General **37**, R161. doi:10.1088/0305-4470/37/31/R01 (2004) (Cited on page 14).

116. Balcerek, M., Burnecki, K., Thapa, S., Wyłomańska, A. & Chechkin, A. *Fractional Brownian motion with random Hurst exponent: accelerating diffusion and persistence transitions*. Chaos: An Interdisciplinary Journal of Nonlinear Science **32**, 093114. doi:10.1063/5.0101913 (2022) (Cited on page 14).

117. Guigas, G. & Weiss, M. *Sampling the cell with anomalous diffusion—The discovery of slowness*. Biophysical Journal **94**, 90–94. doi:10.1529/biophysj.107.117044 (2008) (Cited on page 14).

118. Weber, S. C., Spakowitz, A. J. & Theriot, J. A. *Bacterial chromosomal loci move subdiffusively through a viscoelastic cytoplasm*. Physical Review Letters **104**, 238102. doi:10.1103/PhysRevLett.104.238102 (2010) (Cited on page 14).

119. Sabri, A., Xu, X., Krapf, D. & Weiss, M. *Elucidating the origin of heterogeneous anomalous diffusion in the cytoplasm of mammalian cells*. Physical Review Letters **125**, 058101. doi:10.1103/physrevlett.125.058101 (2020) (Cited on page 14).

120. Reverey, J. F., Jeon, J.-H., Bao, H., Leippe, M., Metzler, R. & Selhuber-Unkel, C. *Superdiffusion dominates intracellular particle motion in the supercrowded cytoplasm of pathogenic Acanthamoeba castellanii*. Scientific Reports **5**, 11690. doi:10.1038/srep11690 (2015) (Cited on page 14).

121. Weiss, M. *Single-particle tracking data reveal anticorrelated fractional Brownian motion in crowded fluids*. Physical Review E **88**, 010101. doi:10.1103/PhysRevE.88.010101 (2013) (Cited on page 14).

122. Burnecki, K., Kepten, E., Janczura, J., Bronshtein, I., Garini, Y. & Weron, A. *Universal algorithm for identification of fractional Brownian motion. A case of telomere subdiffusion*. Biophysical Journal **103**, 1839–1847. doi:10.1016/j.bpj.2012.09.040 (2012) (Cited on page 14).

123. Speckner, K. & Weiss, M. *Single-particle tracking reveals anti-persistent subdiffusion in cell extracts*. Entropy **23**, 892. doi:10.3390/e23070892 (2021) (Cited on pages 14, 15).

124. Wong, I. Y., Gardel, M. L., Reichman, D. R., Weeks, E. R., Valentine, M. T., Bausch, A. R. & Weitz, D. A. *Anomalous diffusion probes microstructure dynamics of entangled F-actin networks*. Physical Review Letters **92**, 178101. doi:10.1103/PhysRevLett.92.178101 (2004) (Cited on page 14).

125. Weigel, A. V., Simon, B., Tamkun, M. M. & Krapf, D. *Ergodic and nonergodic processes coexist in the plasma membrane as observed by single-molecule tracking*. Proceedings of the National Academy of Sciences **108**, 6438–6443. doi:10.1073/pnas.1016325108 (2011) (Cited on page 14).

126. Kutner, R. & Masoliver, J. *The continuous time random walk, still trendy: fifty-year history, state of art and outlook*. The European Physical Journal B **90**, 50. doi:10.1140/epjb/e2016-70578-3 (2017) (Cited on page 14).

127. Viswanathan, G. M., Afanasyev, V., Buldyrev, S. V., Murphy, E. J., Prince, P. A. & Stanley, H. E. *Lévy flight search patterns of wandering albatrosses*. Nature **381**, 413–415. doi:10.1038/381413a0 (1996) (Cited on page 14).

128. Sims, D. W., Humphries, N. E., Bradford, R. W. & Bruce, B. D. *Lévy flight and Brownian search patterns of a free-ranging predator reflect different prey field characteristics*. Journal of Animal Ecology **81**, 432–442. doi:10.1111/j.1365-2656.2011.01914.x (2011) (Cited on page 14).

129. Ott, A., Bouchaud, J. P., Langevin, D. & Urbach, W. *Anomalous diffusion in "living polymers": A genuine Levy flight?* Physical Review Letters **65**, 2201–2204. doi:10.1103/physrevlett.65.2201 (1990) (Cited on page 14).

130. Harris, T. H., Banigan, E. J., Christian, D. A., Konradt, C., *et al. Generalized Lévy walks and the role of chemokines in migration of effector CD8$^+$ T cells*. Nature **486**, 545–548. doi:10.1038/nature11098 (2012) (Cited on page 14).

131. Hafner, A. E., Santen, L., Rieger, H. & Shaebani, M. R. *Run-and-pause dynamics of cytoskeletal motor proteins*. Scientific Reports **6**, 37162. doi:10.1038/srep37162 (2016) (Cited on page 14).

132. Burov, S., Jeon, J.-H., Metzler, R. & Barkai, E. *Single particle tracking in systems showing anomalous diffusion: the role of weak ergodicity breaking*. Physical Chemistry Chemical Physics **13**, 1800–1812. doi:10.1039/c0cp01879a (2011) (Cited on pages 14, 15).

133. Benelli, R. & Weiss, M. *From sub- to superdiffusion: fractional Brownian motion of membraneless organelles in early C. elegans embryos*. New Journal of Physics **23**, 063072. doi:10.1088/1367-2630/ac0853 (2021) (Cited on page 15).

134. Desai, A., Murray, A., Mitchison, T. J. & Walczak, C. E. *Chapter 20 The use of Xenopus egg extracts to study mitotic spindle assembly and function in vitro.* In: Methods in Cell Biology (ed Rieder, C. L.) vol. 61, 385–412 (Academic Press, 1998). doi:10.1016/s0091-679x(08)61991-3 (Cited on pages 18, 93).

135. Good, M. C. *Encapsulation of Xenopus egg and embryo extract spindle assembly reactions in synthetic cell-like compartments with tunable size.* In: The Mitotic Spindle: Methods and Protocols. (eds Chang, P. & Ohi, R.) vol. 1413, 87–108 (Springer New York, 2016). doi:10.1007/978-1-4939-3542-0_7 (Cited on pages 18, 58, 64, 67, 93).

136. Chan, R. C. & Forbes, D. J. *In vitro study of nuclear assembly and nuclear import using Xenopus egg extracts.* In: *Xenopus* Protocols: Cell Biology and Signal Transduction. (ed Liu, X. J.) vol. 322, 289–300 (Humana Press, 2006). doi:10.1007/978-1-59745-000-3_20 (Cited on pages 18, 19).

137. MacLean-Fletcher, S. *Mechanism of action of cytochalasin B on actin*. Cell **20**, 329–341. doi:10.1016/0092-8674(80)90619-4 (1980) (Cited on pages 18, 19).

138. Deming, P. & Kornbluth, S. *Study of apoptosis in vitro using the Xenopus egg extract reconstitution system.* In: *Xenopus* Protocols: Cell Biology and Signal Transduction. (ed Liu, X. J.) vol. 322, 379–393 (Humana Press, 2006). doi:10.1007/978-1-59745-000-3_27 (Cited on pages 18, 93).

139. Sparks, J. & Walter, J. C. *Extracts for analysis of DNA replication in a nucleus-free system*. Cold Spring Harbor Protocols **2019**, pdb.prot097154. doi:10.1101/pdb.prot097154 (2018) (Cited on pages 18, 93).

140. Chang, J. B. & Ferrell, J. E. *Robustly cycling Xenopus laevis cell-free extracts in Teflon chambers*. Cold Spring Harbor Protocols **2018**, pdb.prot097212. doi:10.1101/pdb.prot097212 (2018) (Cited on pages 19, 84, 85, 93, 100).

141. *Technical data sheet, SU-8 2000 permanent negative epoxy photoresist, 2025-2075,* Kayaku Advanced Materials. [Accessed 22-08-2021] (Cited on page 20).

142. Wang, Z., Volinsky, A. A. & Gallant, N. D. *Crosslinking effect on polydimethylsiloxane elastic modulus measured by custom-built compression instrument*. Journal of Applied Polymer Science **131**, 41050. doi:10.1002/app.41050 (2014) (Cited on page 20).

143. Bauer, W.-A. C., Fischlechner, M., Abell, C. & Huck, W. T. S. *Hydrophilic PDMS microchannels for high-throughput formation of oil-in-water microdroplets and water-in-oil-in-water double emulsions*. Lab on a Chip **10**, 1814–1819. doi:10.1039/c004046k (2010) (Cited on page 21).

144. Zinchenko, A., Devenish, S. R. A., Kintses, B., Colin, P.-Y., Fischlechner, M. & Hollfelder, F. *One in a million: flow cytometric sorting of single cell-lysate assays in monodisperse picolitre double emulsion droplets for directed evolution*. Analytical Chemistry **86**, 2526–2533. doi:10.1021/ac403585p (2014) (Cited on page 21).

145. Lee, J. N., Park, C. & Whitesides, G. M. *Solvent compatibility of Poly(dimethylsiloxane)-based microfluidic devices*. Analytical Chemistry **75**, 6544–6554. doi:10.1021/ac0346712 (2003) (Cited on page 22).

146. Randall, G. C. & Doyle, P. S. *Permeation-driven flow in poly(dimethylsiloxane) microfluidic devices*. Proceedings of the National Academy of Sciences **102**, 10813–10818. doi:10.1073/pnas.0503287102 (2005) (Cited on page 22).

147. Thorsen, T., Roberts, R. W., Arnold, F. H. & Quake, S. R. *Dynamic pattern formation in a vesicle-generating microfluidic device*. Physical Review Letters **86**, 4163–4166. doi:10.1103/PhysRevLett.86.4163 (2001) (Cited on page 22).

148. Ai, Y., Xie, R., Xiong, J. & Liang, Q. *Microfluidics for biosynthesizing: from droplets and vesicles to artificial cells*. Small **16**, 1903940. doi:10.1002/smll.201903940 (2019) (Cited on page 22).

149. Garstecki, P., Fuerstman, M. J., Stone, H. A. & Whitesides, G. M. *Formation of droplets and bubbles in a microfluidic T-junction—scaling and mechanism of break-up*. Lab on a Chip **6**, 437–446. doi:10.1039/b510841a (2006) (Cited on page 22).

150. Menech, M. D., Garstecki, P., Jousse, F. & Stone, H. A. *Transition from squeezing to dripping in a microfluidic T-shaped junction*. Journal of Fluid Mechanics **595**, 141–161. doi:10.1017/s002211200700910x (2008) (Cited on page 22).

151. Xu, J. H., Li, S. W., Tan, J. & Luo, G. S. *Correlations of droplet formation in T-junction microfluidic devices: from squeezing to dripping*. Microfluidics and Nanofluidics **5**, 711–717. doi:10.1007/s10404-008-0306-4 (2008) (Cited on page 22).

152. Gupta, A. & Kumar, R. *Effect of geometry on droplet formation in the squeezing regime in a microfluidic T-junction*. Microfluidics and Nanofluidics **8**, 799–812. doi:10.1007/s10404-009-0513-7 (2009) (Cited on page 22).

153. Sivasamy, J., Wong, T.-N., Nguyen, N.-T. & Kao, L. T.-H. *An investigation on the mechanism of droplet formation in a microfluidic T-junction*. Microfluidics and Nanofluidics **11**, 1–10. doi:10.1007/s10404-011-0767-8 (2011) (Cited on page 22).

154. Schindelin, J., Arganda-Carreras, I., Frise, E., Kaynig, V., *et al. Fiji: an open-source platform for biological-image analysis*. Nature Methods **9**, 676–682. doi:10.1038/nmeth.2019 (2012) (Cited on page 25).

155. Manzo, C. & Garcia-Parajo, M. F. *A review of progress in single particle tracking: from methods to biophysical insights*. Reports on Progress in Physics **78**, 124601. doi:10.1088/0034-4885/78/12/124601 (2015) (Cited on page 26).

156. Shen, H., Tauzin, L. J., Baiyasi, R., Wang, W., Moringo, N., Shuang, B. & Landes, C. F. *Single particle tracking: from theory to biophysical applications*. Chemical Reviews **117**, 7331–7376. doi:10.1021/acs.chemrev.6b00815 (2017) (Cited on page 26).

157. Geerts, H., De Brabander, M., Nuydens, R., Geuens, S., Moeremans, M., De Mey, J. & Hollenbeck, P. *Nanovid tracking: a new automatic method for the study of mobility in living cells based on colloidal gold and video microscopy*. Biophysical Journal **52**, 775–782. doi:10.1016/S0006-3495(87)83271-X (1987) (Cited on page 26).

158. De Brabander, M., Nuydens, R., Geerts, H. & Hopkins, C. R. *Dynamic behavior of the transferrin receptor followed in living epidermoid carcinoma (A431) cells with nanovid microscopy*. Cell Motility and the Cytoskeleton **9**, 30–47. doi:10.1002/cm.970090105 (1988) (Cited on page 26).

159. Struntz, P. & Weiss, M. *The hitchhiker's guide to quantitative diffusion measurements*. Physical Chemistry Chemical Physics **20**, 28910–28919. doi:10.1039/c8cp06158k (2018) (Cited on pages 26, 54).

160. Tinevez, J.-Y., Perry, N., Schindelin, J., Hoopes, G. M., Reynolds, G. D., Laplantine, E., Bednarek, S. Y., Shorte, S. L. & Eliceiri, K. W. *TrackMate: An open and extensible platform for single-particle tracking*. Methods **115**, 80–90. doi:10.1016/j.ymeth.2016.09.016 (2017) (Cited on page 26).

161. Dirichlet, P. G. L. *Über die Reduction der positiven quadratischen Formen mit drei unbestimmten ganzen Zahlen.* Journal für die reine und angewandte Mathematik (Crelles Journal) **1850**, 209–227. doi:10.1515/crll.1850.40.209 (1850) (Cited on page 27).

162. Voronoi, G. *Nouvelles applications des paramètres continus à la théorie des formes quadratiques. Deuxième mémoire. Recherches sur les parallélloèdres primitifs.* Journal für die reine und angewandte Mathematik (Crelles Journal) **1908**, 198–287. doi:10.1515/crll.1908.134.198 (1908) (Cited on page 27).

163. Bock, M., Tyagi, A. K., Kreft, J.-U. & Alt, W. *Generalized Voronoi tessellation as a model of two-dimensional cell tissue dynamics*. Bulletin of Mathematical Biology **72**, 1696–1731. doi:10.1007/s11538-009-9498-3 (2010) (Cited on page 28).

164. Ju, L., Du, Q. & Gunzburger, M. *Probabilistic methods for centroidal Voronoi tessellations and their parallel implementations*. Parallel Computing **28**, 1477–1500. doi:10.1016/s0167-8191(02)00151-5 (2002) (Cited on page 28).

165. Honda, H. *Description of cellular patterns by Dirichlet domains: The two-dimensional case*. Journal of Theoretical Biology **72**, 523–543. doi:10.1016/0022-5193(78)90315-6 (1978) (Cited on page 28).

166. Kayser, K. & Stute, H. *Minimum spanning tree - Voronoi's tesselation - Johnson-Mehl diagrams - human lung carcinoma*. Pathology - Research and Practice **185**, 729–734. doi:10.1016/s0344-0338(89)80228-6 (1989) (Cited on page 28).

167. Takinoue, M. & Takeuchi, S. *Droplet microfluidics for the study of artificial cells*. Analytical and Bioanalytical Chemistry **400**, 1705–1716. doi:10.1007/s00216-011-4984-5 (2011) (Cited on page 31).

168. Martino, C. & deMello, A. J. *Droplet-based microfluidics for artificial cell generation: a brief review*. Interface Focus **6**, 20160011. doi:10.1098/rsfs.2016.0011 (2016) (Cited on page 31).

169. Buddingh', B. C. & van Hest, J. C. M. *Artificial cells: synthetic compartments with life-like functionality and adaptivity*. Accounts of Chemical Research **50**, 769–777. doi:10.1021/acs.accounts.6b00512 (2017) (Cited on page 31).

170. Song, H. & Ismagilov, R. F. *Millisecond kinetics on a microfluidic chip using nanoliters of reagents*. Journal of the American Chemical Society **125**, 14613–14619. doi:10.1021/ja0354566 (2003) (Cited on page 31).

171. Sokolova, E., Spruijt, E., Hansen, M. M. K., Dubuc, E., Groen, J., Chokkalingam, V., Piruska, A., Heus, H. A. & Huck, W. T. S. *Enhanced transcription rates in membrane-free protocells formed by coacervation of cell lysate*. Proceedings of the National Academy of Sciences **110**, 11692–11697. doi:10.1073/pnas.1222321110 (2013) (Cited on page 31).

172. Hansen, M. M. K., Meijer, L. H. H., Spruijt, E., Maas, R. J. M., Rosquelles, M. V., Groen, J., Heus, H. A. & Huck, W. T. S. *Macromolecular crowding creates heterogeneous environments of gene expression in picolitre droplets*. Nature Nanotechnology **11**, 191–197. doi:10.1038/nnano.2015.243 (2015) (Cited on page 31).

173. Kelly, B. T., Baret, J.-C., Taly, V. & Griffiths, A. D. *Miniaturizing chemistry and biology in microdroplets*. Chemical Communications, 1773–1788. doi:10.1039/b616252e (2007) (Cited on page 31).

174. Schaerli, Y., Wootton, R. C., Robinson, T., Stein, V., Dunsby, C., Neil, M. A. A., French, P. M. W., deMello, A. J., Abell, C. & Hollfelder, F. *Continuous-flow polymerase chain reaction of single-copy DNA in microfluidic microdroplets*. Analytical Chemistry **81**, 302–306. doi:10.1021/ac802038c (2008) (Cited on page 31).

175. Baroud, C. N., Gallaire, F. & Dangla, R. *Dynamics of microfluidic droplets*. Lab on a Chip **10**, 2032–2045. doi:10.1039/c001191f (2010) (Cited on page 31).

176. Wiklund, M., Green, R. & Ohlin, M. *Acoustofluidics 14: Applications of acoustic streaming in microfluidic devices*. Lab on a Chip **12**, 2438–2451. doi:10.1039/c2lc40203c (2012) (Cited on page 31).

177. Wixforth, A. *Acoustically driven programmable microfluidics for biological and chemical applications*. JALA: Journal of the Association for Laboratory Automation **11**, 399–405. doi:10.1016/j.jala.2006.08.001 (2006) (Cited on page 31).

178. Edwards, B., Mayer, T. S. & Bhiladvala, R. B. *Synchronous electrorotation of nanowires in fluid*. Nano Letters **6**, 626–632. doi:10.1021/nl0522328 (2006) (Cited on page 32).

179. Chong, W. H., Chin, L. K., Tan, R. L. S., Wang, H., Liu, A. Q. & Chen, H. *Stirring in suspension: nanometer-sized magnetic stir bars*. Angewandte Chemie International Edition **52**, 8570–8573. doi:10.1002/anie.201303249 (2013) (Cited on pages 32, 34, 37).

180. Chong, W. H., Huang, Y., Wong, T. N., Ooi, K. T. & Zhu, G.-P. *Magnetic nanorobots, generating vortexes inside nanoliter droplets for effective mixing*. Advanced Materials Technologies **3**, 1700312. doi:10.1002/admt.201700312 (2018) (Cited on pages 32, 34).

181. Bruyker, D. D., Recht, M. I., Bhagat, A. A. S., Torres, F. E., Bell, A. G. & Bruce, R. H. *Rapid mixing of sub-microlitre drops by magnetic micro-stirring*. Lab on a Chip **11**, 3313–3319. doi:10.1039/c1lc20354a (2011) (Cited on page 32).

182. Franke, T., Schmid, L., Weitz, D. A. & Wixforth, A. *Magneto-mechanical mixing and manipulation of picoliter volumes in vesicles*. Lab on a Chip **9**, 2831–2835. doi:10.1039/b906569p (2009) (Cited on page 32).

183. Singh, H., Laibinis, P. E. & Hatton, T. A. *Rigid, superparamagnetic chains of permanently linked beads coated with magnetic nanoparticles. Synthesis and rotational dynamics under applied magnetic fields*. Langmuir **21**, 11500–11509. doi:10.1021/la0517843 (2005) (Cited on page 32).

184. Roy, T., Sinha, A., Chakraborty, S., Ganguly, R. & Puri, I. K. *Magnetic microsphere-based mixers for microdroplets*. Physics of Fluids **21**, 027101. doi:10.1063/1.3072602 (2009) (Cited on page 32).

185. Yang, S., Cao, C., Peng, L., Huang, P., Sun, Y., Wei, F. & Song, W. *Spindle-shaped nanoscale yolk/shell magnetic stirring bars for heterogeneous catalysis in macro- and microscopic systems*. Chemical Communications **52**, 1575–1578. doi:10.1039/c5cc09104g (2016) (Cited on page 32).

186. Van Reenen, A., de Jong, A. M., den Toonder, J. M. J. & Prins, M. W. J. *Integrated lab-on-chip biosensing systems based on magnetic particle actuation – a comprehensive review*. Lab on a Chip **14**, 1966–1986. doi:10.1039/c3lc51454d (2014) (Cited on page 32).

187. Zhang, Y. & Wang, T.-H. *Micro magnetic gyromixer for speeding up reactions in droplets*. Microfluidics and Nanofluidics **12**, 787–794. doi:10.1007/s10404-011-0922-2 (2011) (Cited on page 32).

188. Uebe, R. & Schüler, D. *Magnetosome biogenesis in magnetotactic bacteria*. Nature Reviews Microbiology **14**, 621–637. doi:10.1038/nrmicro.2016.99 (2016) (Cited on page 32).

189. Yan, L., Zhang, S., Chen, P., Liu, H., Yin, H. & Li, H. *Magnetotactic bacteria, magnetosomes and their application*. Microbiological Research **167**, 507–519. doi:10.1016/j.micres.2012.04.002 (2012) (Cited on page 32).

190. Lattuada, M. & Hatton, T. A. *Functionalization of monodisperse magnetic nanoparticles*. Langmuir **23**, 2158–2168. doi:10.1021/la062092x (2006) (Cited on page 32).

191. Stöber, W., Fink, A. & Bohn, E. *Controlled growth of monodisperse silica spheres in the micron size range*. Journal of Colloid and Interface Science **26**, 62–69. doi:10.1016/0021-9797(68)90272-5 (1968) (Cited on page 32).

192. Bogush, G., Tracy, M. & Zukoski, C. *Preparation of monodisperse silica particles: Control of size and mass fraction*. Journal of Non-Crystalline Solids **104**, 95–106. doi:10.1016/0022-3093(88)90187-1 (1988) (Cited on page 32).

193. Shanthil, M., Thomas, R., Swathi, R. S. & Thomas, K. G. *Ag@SiO_2 core-shell nanostructures: Distance-dependent plasmon coupling and SERS investigation*. The Journal of Physical Chemistry Letters **3**, 1459–1464. doi:10.1021/jz3004014 (2012) (Cited on pages 33, 34).

194. Pastoriza-Santos, I., Pérez-Juste, J. & Liz-Marzán, L. M. *Silica-coating and hydrophobation of CTAB-stabilized gold nanorods*. Chemistry of Materials **18**, 2465–2467. doi:10.1021/cm060293g (2006) (Cited on page 33).

195. Rho, W.-Y., Kim, H.-M., Kyeong, S., Kang, Y.-L., Kim, D.-H., Kang, H., Jeong, C., Kim, D.-E., Lee, Y.-S. & Jun, B.-H. *Facile synthesis of monodispersed silica-coated magnetic nanoparticles*. Journal of Industrial and Engineering Chemistry **20**, 2646–2649. doi:10.1016/j.jiec.2013.12.014 (2014) (Cited on page 33).

196. Hui, C., Shen, C., Tian, J., Bao, L., Ding, H., Li, C., Tian, Y., Shi, X. & Gao, H.-J. *Core-shell Fe_3O_4@SiO_2 nanoparticles synthesized with well-dispersed hydrophilic Fe_3O_4 seeds*. Nanoscale **3**, 701–705. doi:10.1039/c0nr00497a (2011) (Cited on page 33).

197. Yi, D. K., Selvan, S. T., Lee, S. S., Papaefthymiou, G. C., Kundaliya, D. & Ying, J. Y. *Silica-coated nanocomposites of magnetic nanoparticles and quantum dots*. Journal of the American Chemical Society **127**, 4990–4991. doi:10.1021/ja0428863 (2005) (Cited on page 33).

198. Nocera, T. M., Chen, J., Murray, C. B. & Agarwal, G. *Magnetic anisotropy considerations in magnetic force microscopy studies of single superparamagnetic nanoparticles*. Nanotechnology **23**, 495704. doi:10.1088/0957-4484/23/49/495704 (2012) (Cited on page 33).

199. Cēbers, A. & Ozols, M. *Dynamics of an active magnetic particle in a rotating magnetic field*. Physical Review E **73**, 021505. doi:10.1103/physreve.73.021505 (2006) (Cited on pages 33, 50).

200. Gires, P.-Y., Thampi, M. & Weiss, M. *Miniaturized magnetic stir bars for controlled agitation of aqueous microdroplets*. Scientific Reports **10**, 10911. doi:10.1038/s41598-020-67767-z (2020) (Cited on pages 34, 47, 57, 60).

201. *2mag magnetic drivers,* 2mag AG. [Accessed on 21-03-2022]. https://www.2mag.de/images/pdf/kataloge/2mag_Magnetic_Stirrers.pdf (Cited on page 38).

202. Zhang, Y., Kuang, M., Zhang, L., Yang, P. & Lu, H. *An accessible protocol for solid-phase extraction of N-linked glycopeptides through reductive amination by amine-functionalized magnetic nanoparticles*. Analytical Chemistry **85**, 5535–5541. doi:10.1021/ac400733y (2013) (Cited on page 42).

203. Williams, E. H., Davydov, A. V., Motayed, A., Sundaresan, S. G., *et al. Immobilization of streptavidin on 4H–SiC for biosensor development*. Applied Surface Science **258**, 6056–6063. doi:10.1016/j.apsusc.2012.02.137 (2012) (Cited on page 42).

204. Albert H. Coons Hugh J. Creech, R. N. J. & Berliner, E. *The demonstration of pneumococcal antigen in tissues by the use of fluorescent antibody*. The Journal of Immunology **45**, 159–170. doi:10.4049/jimmunol.45.3.159 (1942) (Cited on page 42).

205. Riggs, J. L., Seiwald, R. J., Burckhalter, J. H., Downs, C. M. & Metcalf, T. G. *Isothiocyanate compounds as fluorescent labeling agents for immune serum*. The American Journal of Pathology **34**, 1081–1097 (1958) (Cited on page 42).

206. Greb, C. *Fluorescent dyes | Science Lab | Leica Microsystems*. https://www.leica-microsystems.com/science-lab/fluorescent-dyes/. [Accessed on 16-08-2022] (Cited on page 42).

207. Wacker, J. B., Lignos, I., Parashar, V. K. & Gijs, M. A. M. *Controlled synthesis of fluorescent silica nanoparticles inside microfluidic droplets*. Lab on a Chip **12**, 3111–3116. doi:10.1039/C2LC40300E (2012) (Cited on page 42).

208. *ATTO-TEC fluorescent labels and dyes, catalogue 2009/2010,* ATTO-TEC GmbH. [Accessed on 16-08-2022]. https://www.atto-tec.com/fileadmin/user_upload/Katalog_Flyer_Support/Catalogue_2009_2010.pdf (Cited on page 43).

209. *crosslinking-technical-handbook,* Thermofisher Scientific. [Accessed on 16-08-2022]. https://tools.thermofisher.com/content/sfs/brochures/1602163-Crosslinking-Reagents-Handbook.pdf (Cited on page 43).

210. Mattson, G., Conklin, E., Desai, S., Nielander, G., Savage, M. D. & Morgensen, S. *A practical approach to crosslinking*. Molecular Biology Reports **17**, 167–183. doi:10.1007/bf00986726 (1993) (Cited on page 43).

211. Dunlop, D. J. & Özden Özdemir. *Rock Magnetism: Fundamentals and Frontiers*. 1st ed. (Cambridge University Press, 1997). doi:10.1017/cbo9780511612794 (Cited on page 48).

212. Morozov, K. I. & Leshansky, A. M. *Dynamics and polarization of superparamagnetic chiral nanomotors in a rotating magnetic field*. Nanoscale **6**, 12142–12150. doi:10.1039/c4nr02953d (2014) (Cited on page 49).

213. Ghosh, A., Mandal, P., Karmakar, S. & Ghosh, A. *Analytical theory and stability analysis of an elongated nanoscale object under external torque*. Physical Chemistry Chemical Physics **15**, 10817–10823. doi:10.1039/c3cp50701g (2013) (Cited on page 49).

214. Li, Q., Kartikowati, C. W., Horie, S., Ogi, T., Iwaki, T. & Okuyama, K. *Correlation between particle size/domain structure and magnetic properties of highly crystalline Fe3O4 nanoparticles*. Scientific Reports **7**, 9894. doi:10.1038/s41598-017-09897-5 (2017) (Cited on page 50).

215. Reichel, V., Kovács, A., Kumari, M., Bereczk-Tompa, É., *et al. Single crystalline superstructured stable single domain magnetite nanoparticles*. Scientific Reports **7**, 45484. doi:10.1038/srep45484 (2017) (Cited on page 50).

216. Tierno, P., Claret, J., Sagués, F. & Cēbers, A. *Overdamped dynamics of paramagnetic ellipsoids in a precessing magnetic field*. Physical Review E **79**, 021501. doi:10.1103/physreve.79.021501 (2009) (Cited on page 50).

217. Gires, P.-Y., Thampi, M. & Weiss, M. *Quantifying active diffusion in an agitated fluid*. Physical Chemistry Chemical Physics **22**, 21678–21684. doi:10.1039/d0cp03629c (2020) (Cited on pages 50, 52, 56, 57).

218. Qian, H., Sheetz, M. & Elson, E. *Single particle tracking. Analysis of diffusion and flow in two-dimensional systems*. Biophysical Journal **60**, 910–921. doi:10.1016/s0006-3495(91)82125-7 (1991) (Cited on page 52).

219. Weiss, M. *Resampling single-particle tracking data eliminates localization errors and reveals proper diffusion anomalies*. Physical Review E **100**, 042125. doi:10.1103/physreve.100.042125 (2019) (Cited on page 54).

220. Masui, Y. & Markert, C. L. *Cytoplasmic control of nuclear behavior during meiotic maturation of frog oocytes*. Journal of Experimental Zoology **177**, 129–145. doi:10.1002/jez.1401770202 (1971) (Cited on page 63).

221. Wühr, M., Chen, Y., Dumont, S., Groen, A. C., Needleman, D. J., Salic, A. & Mitchison, T. J. *Evidence for an upper limit to mitotic spindle length*. Current Biology **18**, 1256–1261. doi:10.1016/j.cub.2008.07.092 (2008) (Cited on page 63).

222. Bernardini, G., Andrietti, F., Camatini, M. & Cosson, M.-P. *Xenopus spermatozoon: Correlation between shape and motility*. Gamete Research **20**, 165–175. doi:10.1002/mrd.1120200207 (1988) (Cited on page 64).

223. Grenfell, A. W., Strzelecka, M., Crowder, M. E., Helmke, K. J., Schlaitz, A.-L. & Heald, R. *A versatile multivariate image analysis pipeline reveals features of Xenopus extract spindles*. Journal of Cell Biology **213**, 127–136. doi:10.1083/jcb.201509079 (2016) (Cited on page 66).

224. Classen, A.-K., Anderson, K. I., Marois, E. & Eaton, S. *Hexagonal packing of Drosophila wing epithelial cells by the planar cell polarity pathway*. Developmental Cell **9**, 805–817. doi:10.1016/j.devcel.2005.10.016 (2005) (Cited on page 70).

225. Sugimura, K. & Ishihara, S. *The mechanical anisotropy in a tissue promotes ordering in hexagonal cell packing*. Development **140**, 4091–4101. doi:10.1242/dev.094060 (2013) (Cited on page 70).

226. Kaliman, S., Hubert, M., Wollnik, C., Nuić, L., Vurnek, D., Gehrer, S., Lovrić, J., Dudziak, D., Rehfeldt, F. & Smith, A.-S. *Mechanical regulation of epithelial tissue homeostasis*. Physical Review X **11**, 031029. doi:10.1103/physrevx.11.031029 (2021) (Cited on pages 70, 76).

227. Khetan, N., Pruliere, G., Hebras, C., Chenevert, J. & Athale, C. A. *Self-organized optimal packing of kinesin-5-driven microtubule asters scales with cell size*. Journal of Cell Science **134**. jcs257543. doi:10.1242/jcs.257543 (2021) (Cited on pages 70, 76, 78, 92).

228. Gires, P.-Y., Thampi, M., Krauss, S. W. & Weiss, M. *Exploring generic principles of compartmentalization in a developmental in vitro model*. Development **150**. dev200851. doi:10.1242/dev.200851 (2023) (Cited on pages 70, 78).

229. Verde, F, Berrez, J. M., Antony, C & Karsenti, E. *Taxol-induced microtubule asters in mitotic extracts of Xenopus eggs: requirement for phosphorylated factors and cytoplasmic dynein.* Journal of Cell Biology **112**, 1177–1187. doi:10.1083/jcb.112.6.1177 (1991) (Cited on pages 71, 77).

230. Donth, C. & Weiss, M. *Quantitative assessment of the spatial crowding heterogeneity in cellular fluids*. Physical Review E **99**, 052415. doi:10.1103/physreve.99.052415 (2019) (Cited on page 73).

231. De Carvalho, J., Tlili, S., Hufnagel, L., Saunders, T. E. & Telley, I. A. *Aster repulsion drives short-ranged ordering in the Drosophila syncytial blastoderm*. Development **149**. dev199997. doi:10.1242/dev.199997 (2022) (Cited on pages 76, 92).

232. Mitchison, T., Wühr, M., Nguyen, P., Ishihara, K., Groen, A. & Field, C. M. *Growth, interaction, and positioning of microtubule asters in extremely large vertebrate embryo cells*. Cytoskeleton **69**, 738–750. doi:10.1002/cm.21050 (2012) (Cited on pages 77, 78).

233. Surrey, T., Nédélec, F., Leibler, S. & Karsenti, E. *Physical properties determining self-organization of motors and microtubules*. Science **292**, 1167–1171. doi:10.1126/science.1059758 (2001) (Cited on page 77).

234. Roostalu, J., Rickman, J., Thomas, C., Nédélec, F. & Surrey, T. *Determinants of polar versus nematic organization in networks of dynamic microtubules and mitotic motors*. Cell **175**, 796–808.e14. doi:10.1016/j.cell.2018.09.029 (2018) (Cited on page 77).

235. Mitchison, T. J., Nguyen, P., Coughlin, M. & Groen, A. C. *Self-organization of stabilized microtubules by both spindle and midzone mechanisms in Xenopus egg cytosol*. Molecular Biology of the Cell **24** (ed Li, R.) 1559–1573. doi:10.1091/mbc.e12-12-0850 (2013) (Cited on page 77).

236. Yvon, A.-M. C., Wadsworth, P. & Jordan, M. A. *Taxol suppresses dynamics of individual microtubules in living human tumor cells*. Molecular Biology of the Cell **10** (ed Kirschner, M. W.) 947–959. doi:10.1091/mbc.10.4.947 (1999) (Cited on page 77).

237. Ishihara, K., Decker, F., Caldas, P., Pelletier, J. F., Loose, M., Brugués, J. & Mitchison, T. J. *Spatial variation of microtubule depolymerization in large asters*. Molecular Biology of the Cell **32** (ed Surrey, T.) 869–879. doi:10.1091/mbc.e20-11-0723 (2021) (Cited on page 78).

238. Cheng, X. & Ferrell, J. E. *Apoptosis propagates through the cytoplasm as trigger waves*. Science **361**, 607–612. doi:10.1126/science.aah4065 (2018) (Cited on page 78).

239. Gilbert, S. F. *Early development of the nematode Caenorhabditis elegans.* In: Developmental Biology. 6th ed. (Sunderland (MA): Sinauer Associates, 2000) (Cited on pages 83, 92).

240. Fickentscher, R. & Weiss, M. *Physical determinants of asymmetric cell divisions in the early development of Caenorhabditis elegans*. Scientific Reports **7**, 9369. doi:10.1038/s41598-017-09690-4 (2017) (Cited on pages 83, 88, 92).

241. Campos-Ortega, J. A. & Hartenstein, V. *Stages of Drosophila Embryogenesis.* In: The Embryonic Development of *Drosophila melanogaster.* 9–84 (Springer Berlin Heidelberg, 1985). doi:10.1007/978-3-662-02454-6_3 (Cited on pages 83, 92).

242. Sulerud, T., Sami, A. B., Li, G., Kloxin, A., Oakey, J. & Gatlin, J. *Microtubule-dependent pushing forces contribute to long-distance aster movement and centration in Xenopus laevis egg extracts*. Molecular Biology of the Cell **31** (ed Walczak, C.) 2791–2802. doi:10.1091/mbc.e20-01-0088 (2020) (Cited on page 84).

243. Hutchison, C. J., Brill, D., Cox, R., Gilbert, J., Kill, I. & Ford, C. C. *DNA replication and cell cycle control in Xenopus egg extracts*. Journal of Cell Science **1989**, 197–212. doi:10.1242/jcs.1989.supplement_12.17 (1989) (Cited on page 84).

244. Fainsod, A. & Moody, S. A. *Xenopus - from basic biology to disease models in the genomic era* (CRC Press, Boca Raton, Fla, 2022) (Cited on page 84).

245. Tsai, T. Y.-C., Theriot, J. A. & Ferrell Jr, J. E. *Changes in oscillatory dynamics in the cell cycle of early Xenopus laevis embryos*. PLOS Biology **12** (ed Kirschner, M. W.) e1001788. doi:10.1371/journal.pbio.1001788 (2014) (Cited on page 84).

246. Afanzar, O., Buss, G. K., Stearns, T. & Ferrell, J. E. *The nucleus serves as the pacemaker for the cell cycle*. eLife **9**, e59989. doi:10.7554/elife.59989 (2020) (Cited on pages 84–86).

247. Nolet, F. E., Vandervelde, A., Vanderbeke, A., Piñeros, L., Chang, J. B. & Gelens, L. *Nuclei determine the spatial origin of mitotic waves*. eLife **9**, e52868. doi:10.7554/elife.52868 (2020) (Cited on pages 84–87).

248. Guan, Y., Wang, S., Jin, M., Xu, H. & Yang, Q. *Reconstitution of cell-cycle oscillations in microemulsions of cell-free Xenopus egg extracts*. Journal of Visualized Experiments, 58240. doi:10.3791/58240 (2018) (Cited on pages 84–86).

249. Deneke, V. E., Melbinger, A., Vergassola, M. & Talia, S. D. *Waves of Cdk1 activity in S phase synchronize the cell cycle in Drosophila embryos*. Developmental Cell **38**, 399–412. doi:10.1016/j.devcel.2016.07.023 (2016) (Cited on pages 86, 92).

250. Vergassola, M., Deneke, V. E. & Talia, S. D. *Mitotic waves in the early embryogenesis of Drosophila: Bistability traded for speed*. Proceedings of the National Academy of Sciences **115**, E2165–E2174. doi:10.1073/pnas.1714873115 (2018) (Cited on pages 86, 92).

251. Foe, V. & Alberts, B. *Studies of nuclear and cytoplasmic behaviour during the five mitotic cycles that precede gastrulation in Drosophila embryogenesis*. Journal of Cell Science **61**, 31–70. doi:10.1242/jcs.61.1.31 (1983) (Cited on pages 87, 89).

252. Kotadia, S., Crest, J., Tram, U., Riggs, B. & Sullivan, W. *Blastoderm Formation and Cellularisation in Drosophila melanogaster.* In: Encyclopedia of Life Sciences (eLS). (John Wiley & Sons, Ltd, 2010). doi:10.1002/9780470015902.a0001071.pub2 (Cited on pages 87, 89, 92).

253. Fickentscher, R., Struntz, P. & Weiss, M. *Mechanical cues in the early embryogenesis of Caenorhabditis elegans*. Biophysical Journal **105**, 1805–1811. doi:10.1016/j.bpj.2013.09.005 (2013) (Cited on page 88).

254. *Linear Hall-effect sensor ICs:SS490 series datasheet,* Honeywell Sensing and Internet of Things. [Accessed 12-01-2022]. https://eu.mouser.com/datasheet/2/187/honeywell-sensing-sensors-linear-hall-effect-ics-s-1568346.pdf (Cited on page 101).

Publications

Articles (peer-reviewed)

Extracts from this work have been published in the following articles:
*(* denotes equal contribution)*

1. Pierre-Yves Gires*, Mithun Thampi* and Matthias Weiss
   Miniaturized magnetic stir bars for controlled agitation of aqueous microdroplets
   Scientific Reports **10**, 10911 (2020). doi: 10.1038/s41598-020-67767-z

2. Pierre-Yves Gires*, Mithun Thampi* and Matthias Weiss
   Quantifying active diffusion in an agitated fluid
   Physical Chemistry Chemical Physics **22**, 21678-21684 (2020). doi: 10.1039/d0cp03629c

3. Pierre-Yves Gires*, Mithun Thampi*, Sebastian W. Krauss* and Matthias Weiss
   Exploring generic principles of compartmentalization in a developmental in vitro model
   Development **150**. dev200851 (2023). doi: 10.1242/dev.200851

   ** An earlier version of this article has been deposited in bioRxiv in the following format **

   Pierre-Yves Gires*, Mithun Thampi*, Sebastian W. Krauss* and Matthias Weiss
   Generic principles of space compartmentalization in protocell patterns
   bioRxiv (2022). doi: 10.1101/2022.01.17.476586

Conference contributions

1. Mithun Thampi, Pierre-Yves Gires and Matthias Weiss
   Nano-stir bars for perturbing biofluid microdroplets in a microfluidic channel
   Poster for DPG Spring Meeting (Section Active matter (joint with CPP)) in Regensburg, April 2019
2. Mithun Thampi, Pierre-Yves Gires and Matthias Weiss
   Nanobars for perturbing biofluid microdroplets in a microfluidic channel
   Poster for Sommerfeld School on "Physics of Life" in Munich, October 2019
3. Mithun Thampi, Pierre-Yves Gires and Matthias Weiss
   Magnetic stirbars as a tunable stirrer for cell-like systems
   Poster for DPG virtual conference BPCPPDYSOE 2021 (Section Active matter (joint with DY)), March 2021

Eidesstattliche Versicherung

Hiermit versichere ich an Eides statt, dass ich die vorliegende Arbeit selbstständig verfasst und keine anderen als die von mir angegebenen Quellen und Hilfsmittel verwendet habe.

Weiterhin erkläre ich, dass ich die Hilfe von gewerblichen Promotionsberatern beziehungsweise -vermittlern oder ähnlichen Dienstleistern weder bisher in Anspruch genommen habe, noch künftig in Anspruch nehmen werde.

Zusätzlich erkläre ich hiermit, dass ich keinerlei frühere Promotionsversuche unternommen habe.

Bayreuth, den 15.12.2022

Mithun Thampi